Radar-derived Thermodynamic Structure of a Major Hurricane in Vertical Wind Shear

A DISSERTATION SUBMITTED TO THE GRADUATE DIVISION OF THE UNIVERSITY OF HAWAI'I AT MĀNOA IN PARTIAL FULFILLMENT OF THE REQUIREMENTS FOR THE DEGREE OF

DOCTOR OF PHILOSOPHY

IN

ATMOSPHERIC SCIENCES

DECEMBER 2016

By

Annette M. Foerster

Dissertation Committee:

Michael Bell, Chairperson

Gary Barnes

Jennifer Griswold

Patrick Harr

Wen-Chau Lee

Albert Kim

Acknowledgments

I would like to thank my advisor Michael Bell for his mentorship, his dedication, his encouragement and for providing me with many great opportunities such as attending conferences, visiting NCAR and HRD, and participating in field campaigns. I would like to thank my committee members for their valuable comments and feedback and the members of my research group for many great discussions. Thanks also go to my previous advisor Sarah Jones for her mentorship and for introducing me to the world of hurricane research. I would like to thank my family for supporting me in my decision to continue my education far away from home, and I would like to thank my friends for their encouragement, their support and the countless great memories. I would also like to acknowledge the RAINEX field campaign for collecting the data used for this study. This research was supported by the National Science Foundation Grant AGS-1349881.

Abstract

Investigating the physical mechanisms that determine the location and timing of eyewall convection is critical to understand intensity changes in tropical cyclones. Observations within the eyewall are essential to identify these physical mechanisms, but high resolution measurements of both kinematic and thermodynamic quantities in the eyewall are limited. Direct thermodynamic observations in particular are limited spatially to aircraft tracks and dropsonde paths. This study presents a thermodynamic retrieval tailored specifically toward rapidly rotating vortices, which provides an unprecedented view of the three-dimensional temperature and pressure structure of the inner core region of tropical cyclones using airborne Doppler radar data. The retrieval is applied to observations in Hurricane Rita collected on 23 September 2005 during the RAINEX field campaign. The retrieved pressure and temperature fields along with the wind and precipitation structure of Hurricane Rita emphasize the impact of vertical wind shear on the azimuthal location of convection in the eyewall and show the dynamic and thermodynamic processes that act to balance the vortex tilt. Analysis of the contributions of the retrieved pressure and temperature fields to different azimuthal wavenumbers suggests the interpretation of eyewall convection within a three-level framework of balanced, quasibalanced, and unbalanced motions. The axisymmetric, wavenumber-0 structure is determined by both gradient wind and hydrostatic balance, resulting in a pressure drop and temperature increase toward the center. The wavenumber-1 structure, and perhaps in part the wavenumber-2 structure, is determined by the interaction of the storm with environmental vertical wind shear, resulting in a quasi-balance between shear and shear-induced kinematic and thermodynamic anomalies. The higher-order wavenumbers are connected to unbalanced motions and convective cells within the eyewall.

Contents

List of Tables

List of Figures

1 Introduction and Scientific Background

Improved understanding of the processes driving tropical cyclone dynamics is essential for building more accurate models, which in turn results in more accurate forecasts. Recent theoretical studies investigated the influence of the internal structure of tropical cyclones on intensity change. Idealized studies by Pendergrass and Willoughby (2009) and Willoughby (2009) used the classical Sawyer-Eliassen equation in height coordinates to study the effects of location and longevity of convective cells. They showed that the intensification efficiency caused by heating in the eyewall critically depends on the location and timing of these convective cells. The intensification efficiency increases with decreased distance to the center, and with increased duration. Vigh and Schubert (2009) used a theoretical model to emphasize the role of inertial stability for the intensification efficiency, with high intensification efficiencies in the high-inertial-stability region inside the radius of maximum wind and low intensification efficiencies in the low-inertial-stability region outside the radius of maximum wind (RMW).

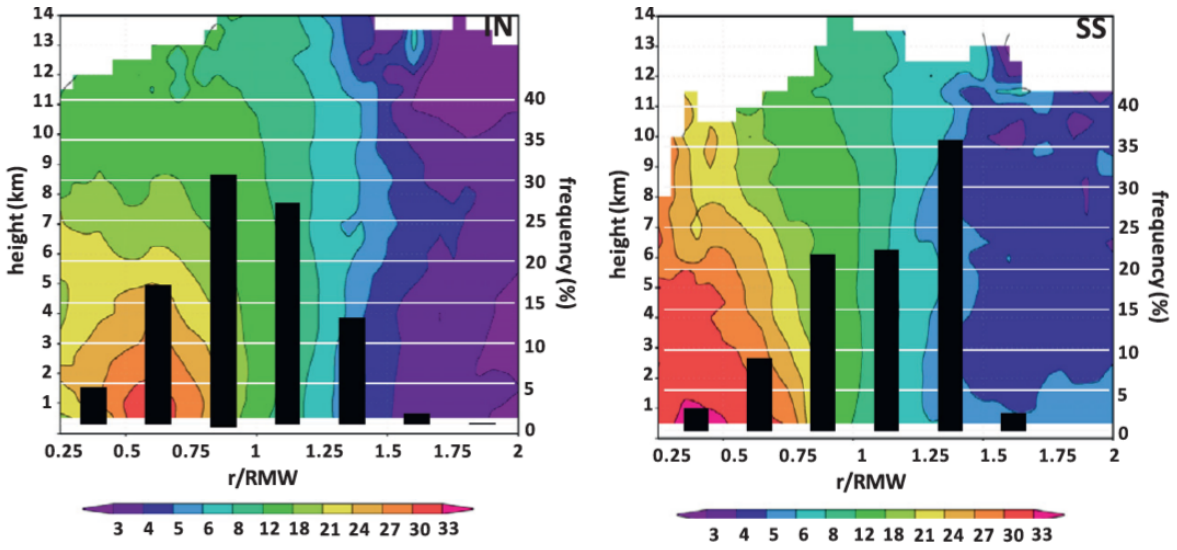

Figure 1: *Frequency of convective burst points (vertical velocity exceeding 5.5 m s^{-1} at 8 km altitude) as a function of normalized radial location (bar chart, %) overlain on normalized radius-height plot of composite-mean axisymmetric vertical vorticity (color shaded, 10^{-4} s^{-1}) for the (left) intensifying and (right) steady state TC composites. From Rogers et al. (2013), their Fig. 15.*

Rogers et al. (2013) confirmed that the radial location of convective bursts differs for intensifying and steady-state storms using radar data from 93 eyewall passes, with the convective bursts in intensifying storms being located inside the radius of maximum wind more fre-

quently than in steady-state storms (Fig. 1). Consequently, the ability to forecast changes in tropical cyclone intensity depends, among other factors, on an improved understanding of the processes that determine the radial location and duration of repeated convective bursts in the tropical cyclone eyewall. Axisymmetric conceptual and numeric models of the eyewall are characterized by moist neutral ascent forced by boundary layer convergence. The eyewall is pictured as a ring of mesoscale ascent, with air parcels rising along constant angular momentum surfaces at the speed they obtain leaving the boundary layer (Emanuel, 1995). In contrast, three-dimensional models suggest that a significant fraction of eyewall convective elements may contain positive buoyancy, with a large fraction of the upward mass transport being accomplished by a few buoyant undilute updrafts (Braun et al., 2006).

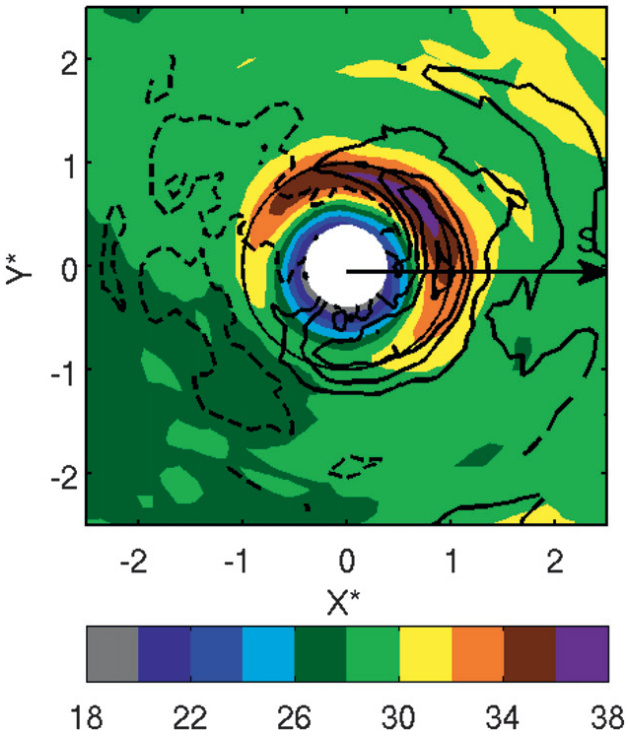

Figure 2: *Shear-relative composite of 2-km reflectivity (dBZ, shaded) and 5-km vertical velocity (m s^{-1}, contour) for cases with maximum velocities $V_{max} > 31$ m s^{-1} and deep-layer shear $S_{850-200} > 2.5$ m s^{-1}. Negative values of vertical velocity are bounded by the dashed contour. Positive values (solid) are contoured from 0.5 m s^{-1} at an interval of 0.5 m s^{-1}. Horizontal distance (X*, Y*) is scaled by the radius of maximum wind at 2 km height with r* = 1 denoted by the circle. Shear vector points to the east. From Reasor et al. (2013), their Fig. 10.*

One of the primary environmental factors directly impacting the structure of eyewall convection is vertical wind shear. It introduces a vortex tilt, and modifies the azimuthal location of convection as well as the thermodynamic structure. Many observational studies, including

composite studies of satellite-derived precipitation data (Hence and Houze, 2011), airborne radar data (Marks et al., 1992, Black et al., 2002, Reasor and Eastin, 2012, Reasor et al., 2013, DeHart et al., 2014), and lightning data (Corbosiero and Molinari, 2002, 2003) found a shear-induced wavenumber-1 pattern in the convective structure of the eyewall, with the strongest upward motion downshear and the highest radar reflectivities left of shear (Fig. 2). Black et al. (2002) and Braun et al. (2006) highlight that while the time-averaged vertical motion shows a clear wavenumber-1 pattern, the instantaneous vertical motion is closely linked to individual deep updraft towers, which form downtilt right, mature as they rotate cyclonically around the eyewall, and dissipate in the downtilt left direction. The time-averaged wavenumber-1 pattern represents the envelope of these convective elements.

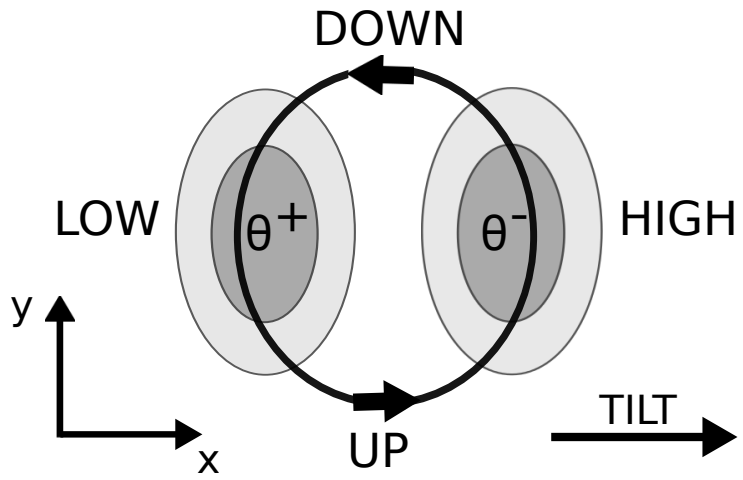

Figure 3: *Schematic of the mechanisms contributing to the vertical circulation. A plan view of the potential-temperature perturbation. The shaded region shows a positive potential-temperature anomaly (θ^+) where the isentropes are lowered and a negative potential-temperature anomaly (θ^-) where they are raised. The bold circle illustrates the relative motion through the anomaly, which descends as it moves towards the region of lowered isentropes and ascends as it moves towards the region of raised isentropes. Adapted from Jones (1995), her Fig. 4c.*

Jones (1995) investigated the impacts of vertical wind shear on barotropic vortices using a primitive-equation numerical model. She found that the vortex initially tilts downshear, then precesses and with time reaches an equilibrium tilt direction somewhere in the left of shear semicircle. As a result of the tilt, potential temperature and vertical velocity anomalies are introduced such that the flow remains balanced. The potential temperature and vertical velocity anomalies are phase-shifted by 90°, with negative potential temperature anomalies

in the downtilt direction, descent left-of-tilt, positive potential temperature anomalies in the uptilt direction, and ascent right-of-tilt. This pattern is consistent with lifting along isentropes right-of-tilt, resulting in negative potential temperature anomalies downshear, and adiabatic descent left-of-tilt, resulting in positive potential temperature anomalies upshear (Fig. 3).

Frank and Ritchie (1999) investigated the impact of vertical wind shear on the location of forced ascent in the eyewall with a series of dry and moist simulations using the Pennsylvania State University-National Center for Atmospheric Research Mesoscale Model version 5 (MM5). They show in their dry runs and in the early periods of their moist runs that the downshear right direction is the preferred location for strong, deep ascent, whereas the downshear left is favored later on in their moist runs. They conclude that adiabatic lifting mechanisms dominate in the dry and early moist runs, but once the eyewall becomes saturated the latent heat release interrupts the adiabatic lifting mechanisms.

Wang and Holland (1996) and Reasor et al. (2004) confirmed the quasi-steady orientation of the tilt toward the downshear left direction. Reasor et al. (2004), however, questioned the role of the diabatically driven secondary circulation to realign the vortex. They argue that the realignment is due to dry adiabatic dynamics, specifically the projection of the tilt asymmetry onto vortex Rossby waves and their subsequent damping. The diabatically driven secondary circulation is believed to play only an indirect role with its axisymmetric component acting to increase the damping efficiency.

Reasor and Eastin (2012) found wavenumber-1 asymmetries in vertically-sheared Hurricane Guillermo (1997) for two different intensive observing periods (IOPs). Their airborne Doppler radar observations showed wavenumber-1 vertical velocity asymmetries at 5 km, with the largest upward motion down- shear left, and wavenumber-1 vertical vorticity asymmetries at 2 km, with positive vorticity left-of-shear out to 20 km radius and negative vorticity beyond 30 km radius (Fig. 4). They suggested that the vorticity structure can be attributed to vortex tube stretching and the large-scale tilt of the vortex. The positive vorticity values inside of 20 km radius occur in the convectively active left-of-shear region, which might result from vorticity amplification through vortex stretching. The vorticity outside of 30 km radius in the vortex skirt is believed to reflect the large-scale tilt of Guillermo's vortex. Potential temperature perturbation asymmetries at 3 and 6 km flight levels derived from in situ aircraft measurements of Guillermo indicated a wavenumber-1 temperature asymmetry. Cold anomalies were located left-of-shear at 3 km for both of their IOPs, and left-of-shear and downshear respectively at 6 km.

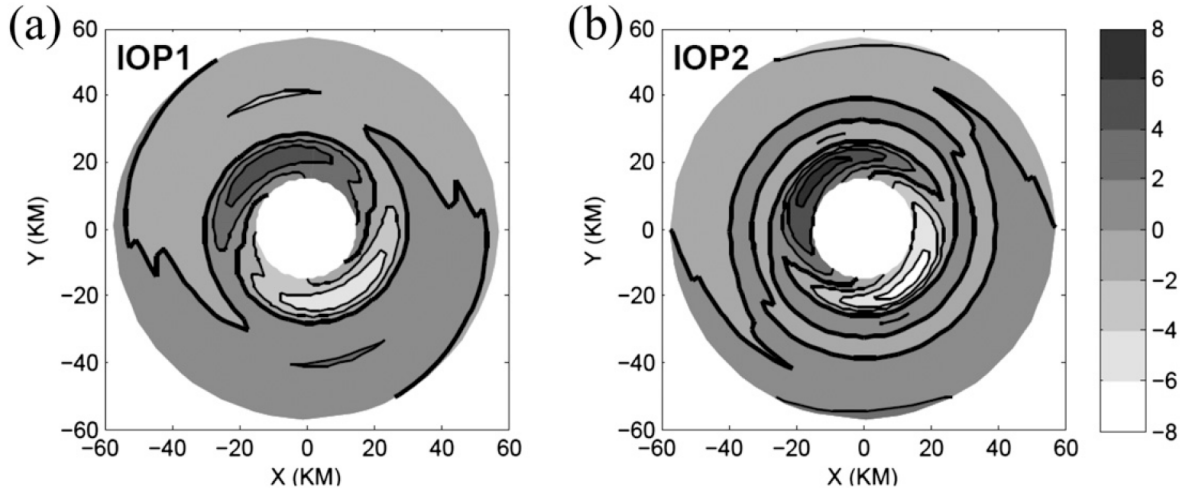

Figure 4: *Time-averaged wavenumber-1 vertical vorticity asymmetry (shaded, 10^{-4} s^{-1}) at 2 km for (a) IOP1 and (b) IOP2. The zero contour is indicated by the heavy line. All fields have been rotated such that the large-scale vertical wind shear vector points due east. From Reasor and Eastin (2012), their Fig. 10.*

The majority of studies about the impact of vertical wind shear on eyewall convection have focused on the wavenumber-1 structure of wind and precipitation fields. Less attention has been paid to the thermodynamic properties, in part because of a lack of observations. Jones (1995) showed that the tilt introduces a thermal couplet. She also mentions that horizontal advection may act to rotate the thermal anomalies cyclonically, whereas vertical advection may act to rotate the thermal anomalies anticyclonically. In a subsequent study with baroclinic vortices Jones (2000) found an anticyclonic rotation of the temperature anomalies with height and attributed it to the coincident anticyclonic rotation of the tilt with height, keeping the relative orientation of tilt and temperature anomalies constant. She also showed that the temperature anomalies resulted in enhanced low-level stability uptilt, and reduced low-level stability downtilt. Reasor and Eastin (2012) derived potential temperature asymmetries from aircraft flight-level measurements of Hurricane Guillermo (1997) for two different IOPs and two vertical levels, 3 km and 6 km. The data coverage is limited, but their results are in agreement with Jones (2000), showing a mesoscale thermal couplet, with cold anomalies in the downtilt direction (Fig.5). Braun et al. (2006) found a similar relationship between tilt and potential temperature anomalies in their high-resolution simulation of Hurricane Bonnie, with cold anomalies located in the downtilt direction at 5 km height. They offer two possible explanations for this cold anomaly, which Frank and Ritchie (1999) suggested should not exist in moist simulations of intense tropical cyclones, because latent heating eliminates the temperature anomalies. The first possible explanation is that the latent heat-

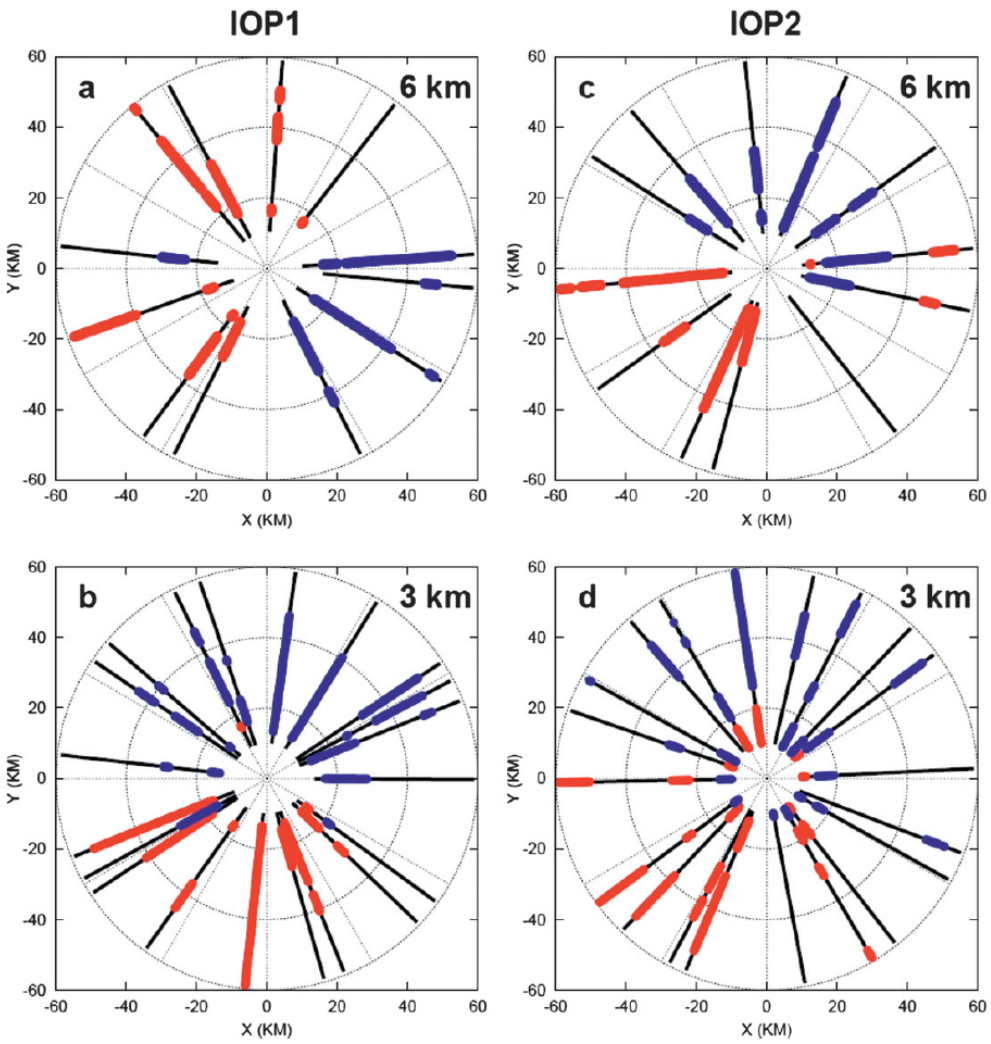

Figure 5: *Potential temperature asymmetry derived from aircraft flight-level measurements for (left) IOP1 and (right) IOP2. Red (blue) colors denote azimuthal perturbation potential temperatures that exceed +1 K (-1 K), which roughly corresponds to the mean standard deviation from the azimuthal mean radial profile. All fields have been rotated such that the large-scale VWS vector points due east. From Reasor and Eastin (2012), their Fig. 11.*

ing in the eyewall updrafts might be exceeded by adiabatic cooling, and the second possible explanation is that in case latent heating and adiabatic cooling balance exactly, the thermal couplet might be a result of adiabatic warming of dry, subsiding air on the uptilt side. In either case, they conclude that the convective forcing caused by this temperature couplet is weak and only plays a minor role in forcing eyewall convection.

Braun et al. (2006) suggest that the deep convective towers in the eyewall are a result of the interaction of shear-induced relative flow and eyewall mesovortices, specifically that updrafts

are initiated where the low level inflow collides with the mesovortex circulation (Fig. 6, left panel). Braun and Wu (2007) showed that the organization of vertical motion in the eyewall is dependent on the magnitude of the shear. Their conceptual model suggests that in weak to moderate shear the dominant convective forcing mechanism is the interaction of eyewall mesovortices with the low level inflow, whereas in stronger shear the dominant mechanism is eye-eyewall mixing due to a vortex couplet consisting of a cyclonic vortex downtilt and an anticyclonic vortex downtilt right which induces flow across the eye (Fig. 6, right panel).

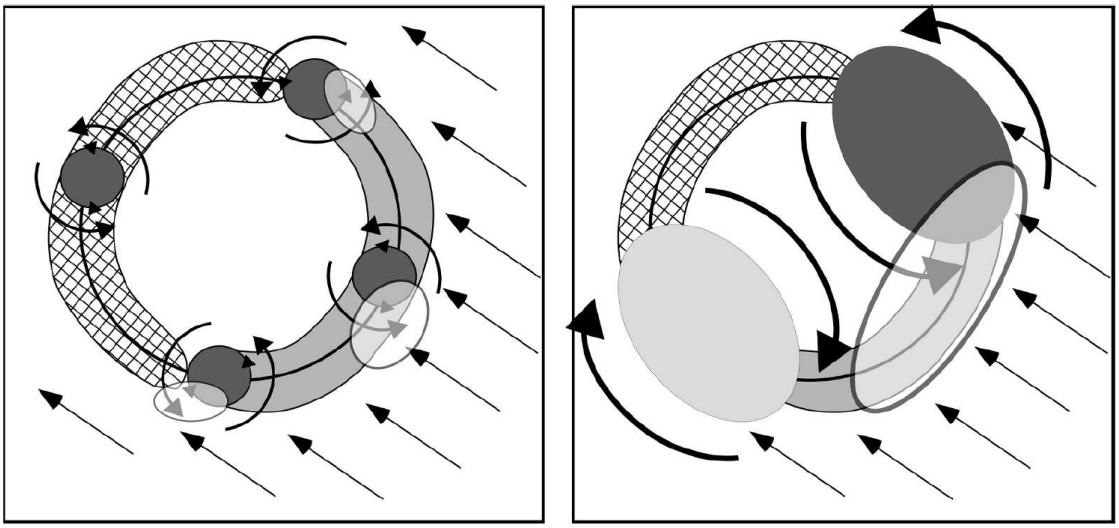

Figure 6: *Schematic diagram summarizing (left) the interaction between eyewall mesovortices and the low-level inflow associated with weak-to-moderate environmental wind shear; (right) similar to (left), but for strong shear. The elongated semicircular areas indicate where shear effects favor low-level convergence (light shading) and divergence (cross hatching). The low-level storm-relative flow associated with the environmental shear is indicated by the straight arrows. In (left), the mesovortices and their local cyclonic circulations are indicated by darkly shaded circles and curved arrows. In (right), a cyclonic-anticyclonic vortex couplet is indicated by the dark-light shaded ovals and their associated circulations by curved arrows. The semitransparent, lightly shaded ovals represent areas of enhanced low-level convergence and upward motion. The orientation of the low-level eyewall convergence-divergence asymmetry associated with the sheared flow is held fixed in this figure and may not necessarily match that of the simulations. From Braun and Wu (2007), their Fig. 12.*

The two physical mechanisms that can act to vertically accelerate individual updrafts are buoyancy and vertical pressure gradients. In a horizontally uniform, resting environment, buoyancy describes an upward acceleration resulting from the density difference between parcel and environment (Principle of Archimedes). In the atmosphere, density is closely related to temperature, pressure, humidity and water loading and can be expressed in terms of density potential temperature θ_ρ. Differences between parcel and environment in either

one of these three variables result in the parcel being positively or negatively buoyant. The common assumption of a horizontally uniform environment is not valid for tropical cyclones, because of the pronounced pressure minimum at the storm center, which causes the isobars to slope downward with decreasing radius. Thus, an air parcel in a tropical cyclone that is lighter than its environment will experience an upward and inward acceleration.

Two modeling studies (Zhang et al., 2000, Braun, 2002) and one observational study (Eastin et al., 2005) investigated buoyancy in the eyewall of tropical cyclones. The studies came to different conclusions. While Zhang et al. (2000) found that the eyewall is negatively buoyant and the updrafts are driven mainly by the vertical perturbation pressure gradient force, Braun (2002) and Eastin et al. (2005) found areas of positive buoyancy in the eyewall. Smith et al. (2005) addressed these seemingly contradicting findings by pointing out the importance of the definition of the reference state for the interpretation of the results. Buoyancy, in contrast to vertical acceleration, is not defined uniquely, but with respect to a reference state. Thus, the choice of this reference state is crucial for the interpretation.

Tropical cyclones are usually considered to be in approximate hydrostatic balance, and in approximate gradient wind balance outside the boundary layer. Based on in situ aircraft observations, Willoughby (1990) showed that the gradient wind balance is valid to within 1.5 m s^{-1} outside the boundary layer for the azimuthal mean tangential wind. This means that the bulk of the pressure gradient field is in balance with the primary wind field and does not act to accelerate air parcels. The hydrostatic assumption is valid if vertical accelerations are negligible, which is the case for convectively-neutral updrafts. This hydrostatic assumption might not be valid for individual updrafts, but it is valid on average for the primary vortex. Hence, using the thermal wind balanced vortex as the reference state for buoyancy calculations is the natural choice for tropical cyclones (Smith et al., 2005), and makes interpretation easier, because in this framework positive buoyancy translates into upward acceleration, unless the vertical perturbation pressure gradient counteracts. This upward acceleration strengthens the secondary circulation, which in turn can enhance the primary circulation and thus intensify the tropical cyclone.

Determining whether any given eyewall location is buoyant with respect to the balanced vortex requires kinematic and thermodynamic measurements. Measurements of the wind field throughout the entire vortex are necessary to compute the balanced vortex reference state, and temperature, pressure and moisture measurements are necessary to determine whether or not the location is buoyant. However, in-situ observations exist only along flight tracks or dropsonde paths. Hence, a complete picture of the buoyancy distribution within

the eyewall can't be obtained from direct observations.

In the past, several approaches have been taken to estimate pressure and temperature fields from radar data. Radar data are an excellent data source because they provide great spatial coverage at a good horizontal and vertical resolution. The traditional thermodynamic retrievals are based on seminal work by Gal-Chen (1978) and use the horizontal and vertical momentum equations, sometimes complemented with the thermodynamic equation and other constraints, to infer thermodynamic properties from kinematic measurements (Gal-Chen, 1978, Roux, 1985, Viltard and Roux, 1998, Liou, 2001). These methods were developed for mesoscale convective situations such as squall lines. Hence, they all assume a horizontally uniform reference state in hydrostatic balance.

Predicting tropical cyclone intensity and especially tropical cyclone intensity change remains challenging and the understanding of mesoscale convective organization in tropical cyclones is still incomplete. An improved understanding of how convective activity and organization affects intensity change and what the dominant convective forcing mechanisms in the eyewall are is instrumental in improving our ability to correctly forecast intensity change. With my research I specifically want to address the following questions:

1. Is the eyewall convection buoyant?
2. Can thermodynamic fields in the inner core region of tropical cyclones be estimated from Doppler radar data?
3. What are the mesoscale and convective-scale structures of the thermodynamic fields?
4. How does vertical wind shear impact the thermodynamic structure?

Kinematic and thermodynamic measurements with high spatial coverage throughout the eyewall region are necessary to adequately answer the first question. However, direct thermodynamic measurements are only available along flight tracks or dropsonde paths. Thus, the first step in addressing the research questions stated above is to develop a method to retrieve the temperature and pressure fields from Doppler radar data. The thermodynamic retrieval is specifically tailored toward tropical cyclones and builds on technical advancements from a recently developed variational wind retrieval software tool that uses a spline-based representation of the analyzed wind field. The retrieval method uses the balanced vortex as reference state to simplify the interpretation of the temperature and pressure perturbations, and to improve the numerical accuracy of the retrieval. The second step is to evaluate the retrieval and to quantify the retrieval uncertainties using a Weather Research and Forecasting

(WRF) simulation. The final step is to apply the thermodynamic retrieval to observations in Hurricane Rita (2005) and to examine the kinematic and thermodynamic structure of Rita, in particular with respect to the effect of vertical wind shear on the thermodynamic structure of the eyewall convection. Hurricane Rita provides an excellent dataset to study the mesoscale structure of a tropical cyclone in vertical wind shear. It is one of the most well observed storms in history, simultaneously observed by three different aircraft over an extended period of time during the Hurricane Rainband and Intensity Change Experiment (RAINEX). Section 2 outlines the different steps of the thermodynamic retrieval method. Section 3 evaluates the thermodynamic retrieval using a WRF simulation. Section 4 analyzes the kinematic and thermodynamic structure of Hurricane Rita on 23 September 2005, and section 5 summarizes the results and provides conclusions.

2 Method

The retrieval of the temperature and pressure perturbations from Doppler radar data is performed in three distinct steps. First, the radar data (and optionally other observational data) are combined into a three-dimensional analysis of wind and precipitation fields using the software tool called Spline Analysis at Mesoscale Utilizing Radar and Aircraft Instrumentation (SAMURAI, Bell et al. (2012a) and https://github.com/mmbell/samurai). Second, reference state temperature and pressure fields are calculated to facilitate the retrieval and the interpretation of the perturbations. Third, the temperature and pressure perturbations are retrieved by variationally solving a set of modified momentum equations. Details of each of the three steps are described in the following subsections.

2.1 Wind Retrieval

The SAMURAI software estimates the most likely state of the atmosphere based on observations. It can combine different types of observations such as radar data, dropsonde data, flight track data, atmospheric motion vectors and other data types, specifying the error characteristics individually for each type of observation. It is possible to incorporate model fields from global or mesoscale models as background estimates, and to add balance or physical constraints such as mass continuity. SAMURAI solves for the most likely atmospheric state by minimizing a cost function in incremental form $J(\hat{\mathbf{x}})$ that avoids the inversion of the background error covariance matrix by using a control variable $\hat{\mathbf{x}}$:

$$J(\hat{\mathbf{x}}) = \frac{1}{2}\hat{\mathbf{x}}^T\hat{\mathbf{x}} + \frac{1}{2}(\mathbf{HC}\hat{\mathbf{x}} - d)^T\mathbf{R}^{-1}(\mathbf{HC}\hat{\mathbf{x}} - d) \tag{1}$$

where $\mathbf{H}$ denotes the linearized observation operator, $\mathbf{C}$ denotes the square root of the background error covariance matrix, $\mathbf{R}$ denotes the observation error covariance matrix, and $d \equiv \mathbf{y} - h(\mathbf{x}_b)$ denotes the difference between the observations $\mathbf{y}$ and the nonlinear observation operator applied to the background state estimate $h(\mathbf{x}_b)$. For linear operators such as radial velocity or in situ measurements h and $\mathbf{H}$ are equivalent. For more details on the variational cost function see Gao et al. (2004). The cost function is minimized using a conjugate gradient algorithm including a cubic spline transform and low pass filter operations as part of the $\mathbf{C}$ operator. SAMURAI solves for the moist-air-density-weighted wind components (ρu, ρy, and ρw), temperature T, water vapor mixing ratio q_v, and dry-air density ρ_a. The control variable is $\mathbf{x} = \{\rho u, \rho v, \rho w, T', q_v', \rho_a'\}$, where the thermodynamic quantities are defined relative to a hydrostatic reference state. The SAMURAI output file

contains the three wind components (u,v, and w), temperature, pressure, water vapor mixing ratio or radar reflectivity, dry-air density, and additionally the spatial derivatives of the wind field and other derived quantities. Note that the estimate of the thermodynamic state of the atmosphere is usually based on very limited in situ observations not sufficient to construct a full 3D field. Extensive sampling or a background estimate can mitigate this shortcoming to some extent. The accuracy of the wind field is highly dependent on the radar sampling geometry. In the case of a well-resolved geometry without Doppler errors the accuracy of the wind field is estimated to be less than 2 m s^{-1} (Hildebrand et al., 1996). SAMURAI has three spatial filters that can be used to both smooth the analysis and spread information from the observations throughout the domain. A Fourier spectral filter allows for elimination of high wavenumber features in the spectral domain. This filter has the sharpest response, and the filter wavelength is specified as the maximum wavenumber allowed in each spatial dimension. The second filter is the 'spline cutoff' which operates on the finite element basis during the spline transform and is described in detail by Ooyama (2002). It is implemented as a third derivative constraint on the cubic B-spline representation of the analysis, such that an increasing weight will further damp the third derivative. The cutoff wavelength is given in terms of the number of nodal points and determines the amount of smoothing. This filter has a very sharp response function that can be considered 'semi-spectral', and is equivalent to a sixth order polynomial. The third filter is the Gaussian recursive filter, which is described in detail by Purser et al. (2003). This filter models a Gaussian low-pass filter through an efficient recursive operator. It has the broadest response function, but produces a smooth Gaussian covariance for a delta function input. The filter wavelength is given in terms of the number of nodal points, and is equivalent to a second order polynomial. The filters can be used individually or can be combined to produce different spectral responses. Interested readers are referred to Bell et al. (2012a) for additional technical details of SAMURAI.

2.2 Gradient-Wind-Balanced Reference State

Buoyancy is not defined uniquely, it is defined with respect to a reference state. The conventional definition of buoyancy b is based on Archimedes principle and states that an air parcel will accelerate vertically in the case that the density of the parcel ρ_p and the density of the environment ρ_0 differ:

$$b = -g\frac{\rho_p - \rho_0}{\rho_0} = -g\frac{\rho'}{\rho_0} = g\left[\frac{\theta'_v}{\theta_{v,0}} + (R/c_p - 1)\frac{p'}{p_0} - q'_l\right] \tag{2}$$

where g is the gravitational acceleration, R is the specific gas constant, c_p is the specific heat capacity at constant pressure and density is a function of virtual potential temperature θ_v, pressure p and liquid water mixing ratio q_l. Primes represent the differences between parcel and environment, e.g. $\rho' = \rho_p - \rho_0$.

The vertical momentum equation states that buoyancy is not the only mechanism causing vertical acceleration. The vertical acceleration is caused by the sum of the pressure gradient force and the gravitational force, which can be rewritten in terms of buoyancy and vertical perturbation pressure gradient force:

$$\frac{Dw}{Dt} = -\frac{1}{\rho}\frac{\partial p}{\partial z} - g = -\frac{1}{\rho}\frac{\partial p'}{\partial z} + b \tag{3}$$

where w is the vertical velocity, D/Dt the material derivative, t the time, p the pressure and z the height. The vertical acceleration Dw/Dt is uniquely defined. The partitioning into buoyancy and vertical perturbation pressure gradient depends on the definition of the perturbation and reference states.

This ambiguity of the buoyancy definition makes the interpretation of buoyancy challenging and emphasizes the importance of an appropriate reference state definition. For ordinary tropical convection, the horizontal mean is a good choice because the horizontal changes in environmental temperature and pressure are small. For rapidly rotating vortices, however, the pressure and temperature surfaces slope significantly with radius, complicating the choice of the reference state definition. Studies on the importance of the buoyancy force on the convection in the tropical cyclone eyewall (Zhang et al., 2000, Braun, 2002, Eastin et al., 2005) have shown seemingly contradicting results, due in part to different reference state definitions. A comparison of these different reference states will be shown later on in this section. Smith et al. (2005) proposed the use of a vortex in thermal wind balance as the reference state. They argue that this way, the reference state contains the fraction of the temperature and pressure fields that are balanced by the mean tangential wind field, whereas the unbalanced fraction of the fields can accelerate air parcels. This gradient-wind-balanced reference state can be calculated without approximation from the azimuthally-averaged tangential wind field and vertical temperature and pressure profiles at large radius (Smith, 2006). Combining the vertical and radial derivatives of the gradient wind and hydrostatic balance relationships, respectively, gives a linear first-order partial differential equation, which can be solved using

the method of characteristics. The characteristics are the surfaces of constant pressure:

$$\frac{dz}{dr} = \frac{1}{g}\left(\frac{\bar{V}_T^2}{r} + f\bar{V}_T\right) \tag{4}$$

The variation in density potential temperature along these characteristics is:

$$\frac{\partial \ln \bar{\theta}_\rho}{\partial r} = \frac{1}{g}\frac{\partial}{\partial z}\left(\frac{\bar{V}_T^2}{r} + f\bar{V}_T\right) \tag{5}$$

where $\bar{V}_T$ is the azimuthally averaged tangential wind, r is the radius, z is altitude, f is the Coriolis parameter, g is the gravitational acceleration, and $\bar{\theta}_\rho$ is the azimuthally averaged density potential temperature, which includes the contribution of condensate loading to density. Equations 4 and 5 can be used to calculate the temperature and pressure fields of the balanced state by integrating the thermal wind equation inward from the outer boundaries, where the temperature and pressure is given by vertical temperature and pressure profiles.

The SAMURAI analysis obtained in the first step of the retrieval (section 2.1) is used to calculate the balanced vortex reference state. The Cartesian wind components are converted to radial and tangential wind components, and the tangential wind is averaged azimuthally. The vertical temperature and pressure profiles needed to anchor the inward integration of the thermal wind equation are calculated from the azimuthally-averaged temperature and pressure fields at the outer edge of the SAMURAI domain. The temperature and pressure fields of the SAMURAI analysis are primarily based on dropsonde observations, which means that the SAMURAI profiles are basically an average of the soundings located at the outer edge of the domain.

The assumption of gradient wind balance is not justified in the boundary layer due to increased amounts of friction. We use a simple parameterization of the wind field in the boundary layer to minimize the introduction of errors. The tangential wind field is assumed to be constant with height in the boundary layer, assuming the values of the wind field at 2 km altitude. This simple parameterization minimizes the effects of the boundary layer wind field on the temperature and pressure retrieval. However, its simplicity also precludes the interpretation of the temperature and pressure fields within the boundary layer. Thus, the interpretation of the results will focus on the regions above the boundary layer.

To illustrate the importance of the reference state definition for the interpretation of the results, a comparison of the buoyancy fields calculated for different reference states is performed using output from a WRF simulation. Details about this simulation will be discussed

in the next chapter. The gradient-wind-balanced reference state is compared to a hydrostatic reference state, which uses the horizontal domain average as the reference value, and to the reference states used by Zhang et al. (2000), Braun (2002), and Eastin et al. (2005) (Fig. 7).

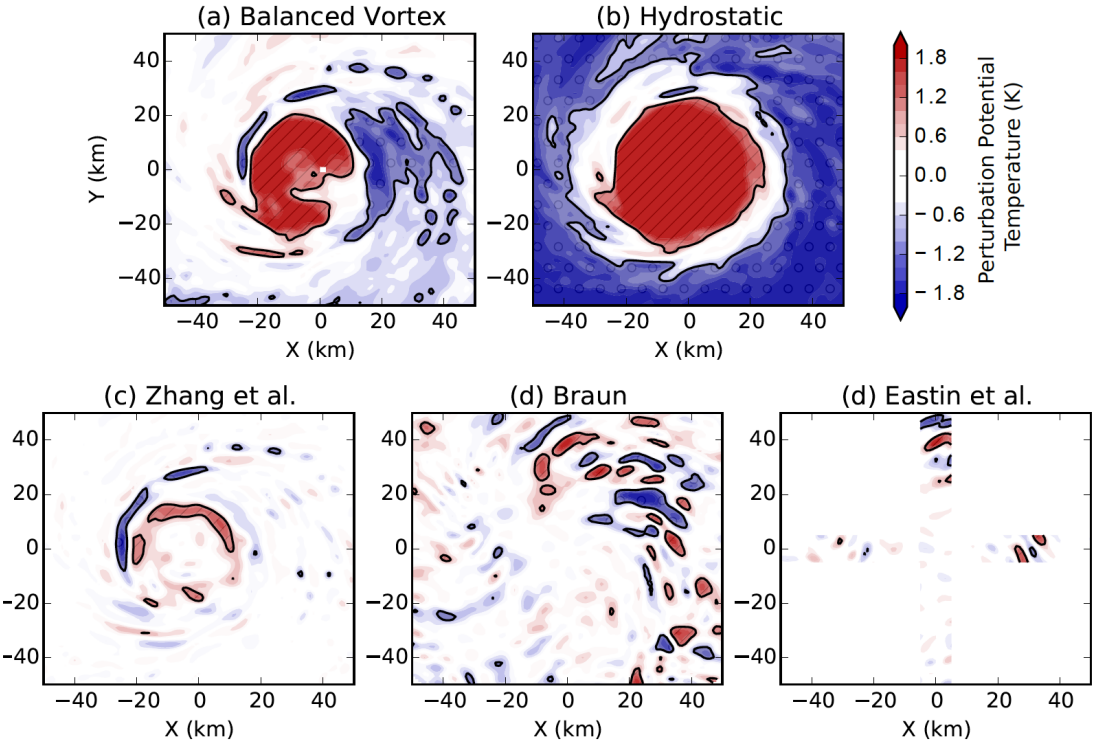

Figure 7: *Perturbation potential temperature (K) at 4 km calculated using different reference state definitions, (a) balanced vortex, (b) horizontally uniform hydrostatic reference state, (c) local (12x12 km box) reference state following Zhang et al. (2000), (d) wavenumber-0 and -1 reference state following Braun (2002), and (e) 20-km running mean reference state following Eastin et al. (2005). Values exceeding 1K are hatched and highlighted, values below -1K are stippled and highlighted.*

The buoyancy fields vary greatly for the different reference states. The balanced vortex reference state (Fig. 7a) shows an area of positive buoyancy in the western semicircle and an area of negative buoyancy to the east of the center, with smaller-scale anomalies outside. The buoyancy distribution with respect to the hydrostatic reference state (Fig. 7b) basically only reflects the warm-core structure of the tropical cyclone. The inner region is warmer than the horizontal average, and the outer region is colder than the horizontal average, thus it appears that the inner region is positively buoyant and the outer region is negatively buoyant. Here, the hydrostatic reference state uses the domain-average temperature field. If, instead, the hydrostatic reference state had been chosen to use the temperature field at the edge of the domain, as is typically done for thermodynamic retrievals, the structure

of the anomalies would remain the same but the buoyancy would be positive everywhere. Zhang et al. (2000) defined their buoyancy with respect to a local reference state (Fig. 7c). They calculated their reference state using the values from four neighboring points on a grid with a horizontal spacing of 6 km. To simulate their reference state, the reference value for this demonstration was calculated from a 12-km x 12-km box around each grid point from the 1-km resolution WRF data. Their buoyancy pattern exhibits a fine-scale structure, with anomalies close to the center. Braun (2002) defined his reference states as the azimuthal wavenumbers zero and one of a Fourier decomposition (Fig. 7d). This method ensured that the warm core and the estimation of the vortex center location do not contribute to the buoyancy calculation. Their buoyancy pattern shows a very fine-scale structure. The buoyancy with respect to a 20-km Bartlett-filtered running mean reference state along the flight track of a figure-4 flight pattern (Fig. 7e), as used by Eastin et al. (2005), shows only a few areas of small-scale anomalies. The figure also illustrates the limited spatial coverage that results from using flight level data. All of these definitions are valid, but they lead to different interpretations of the relationship between vertical motion and the buoyancy field.

2.3 Thermodynamic Retrieval

The retrieval of temperature and pressure perturbations presented in this study is based on seminal work by Gal-Chen (1978), and subsequent studies by Roux (e.g. Roux, 1985, Viltard and Roux, 1998, Roux et al., 1993) and Liou (e.g. Liou, 2001, Liou et al., 2003). Our work expands on these previous studies by using a different reference state definition to account for the tropical cyclone environment, by specifying derivatives directly within the retrieval, and by effectively linking the vertical levels using cubic B-splines. The retrieval minimizes a cost function using a Galerkin approach, with cubic B-spline finite elements as a basis. It has the same spatial filtering capabilities as SAMURAI, with a Fourier spectral filter, a spline cutoff filter, and a Gaussian recursive filter. Moreover, in contrast to other techniques, observations of variable gradients can be used directly as retrieval input. This section outlines the derivation of the set of equations used to construct the cost function. Minimizing this cost function then yields an estimate of the most likely thermodynamic state of the atmosphere.

Following the traditional retrievals, we start with the momentum equations in Cartesian coordinates on a constant f-plane, neglecting momentum transport by precipitation, frictional

forces and subgrid-scale processes.

$$\frac{\partial u}{\partial t} + u\frac{\partial u}{\partial x} + v\frac{\partial u}{\partial y} + w\frac{\partial u}{\partial z} = fv - \frac{1}{\rho}\frac{\partial p}{\partial x} \tag{6}$$

$$\frac{\partial v}{\partial t} + u\frac{\partial v}{\partial x} + v\frac{\partial v}{\partial y} + w\frac{\partial v}{\partial z} = -fu - \frac{1}{\rho}\frac{\partial p}{\partial y} \tag{7}$$

$$\frac{\partial w}{\partial t} + u\frac{\partial w}{\partial x} + v\frac{\partial w}{\partial y} + w\frac{\partial w}{\partial z} = -\frac{1}{\rho}\frac{\partial p}{\partial z} - g \tag{8}$$

The pressure gradient terms are transformed into non-dimensional expressions by using the Exner function $\pi = (p/p_0)^{R_d/c_p}$. Density is expressed in terms of pressure, temperature and moisture using density potential temperature $\theta_\rho = T_\rho \left(\frac{p_0}{p}\right)^{R_d/c_p}$, where the density temperature $T_\rho = \frac{p}{\rho R_d}$ includes contributions of dry air and water in its various states via the total density $\rho = \rho_a + \rho_m + \rho_r$, with subscripts a, m, r representing dry air, non-precipitating moisture (including vapor and condensate), and precipitation (including rain and ice), respectively.

The thermodynamic variables are separated into basic state and perturbations, where the basic state, denoted by the overbar, is a function of radius r and height z only.

$$\theta_\rho = \bar{\theta}_\rho(r,z) + \theta'_\rho \tag{9}$$

$$\pi = \bar{\pi}(r,z) + \pi' \tag{10}$$

Our basic (or reference) state was chosen to be in thermal wind balance:

$$c_p\bar{\theta}_\rho\frac{\partial\bar{\pi}}{\partial z} = -g \tag{11}$$

$$\frac{\bar{V}_T^2}{r} + f\bar{V}_T = c_p\bar{\theta}_\rho\frac{\partial\bar{\pi}}{\partial r} \tag{12}$$

where the gradient wind balance relationship is expressed in cylindrical coordinates using the tangential velocity $\bar{V}_T$. The hydrostatic balance relationship can be used to simplify the vertical momentum equation, and the horizontal derivatives of the reference state pressure field ($\frac{\partial\bar{\pi}}{\partial x}$ and $\frac{\partial\bar{\pi}}{\partial y}$, calculated in the previous section) can be used to specify the horizontal gradients of the basic state pressure field. The terms in the momentum equations are expanded into basic state and perturbations and the nonlinear term are neglected in the vertical momentum equation. Initial tests of the retrieval with only these three modified momentum equations showed good results for the pressure retrieval, but unsatisfactory results for the

temperature retrieval. The vertical momentum equation links the pressure and temperature fields together, however, it is the only equation containing θ'_ρ. The pressure term in the vertical momentum equation is several orders of magnitude larger than the temperature term, which caused a poor temperature retrieval performance. To mitigate this problem we followed Roux (1985) and combined the derivatives of the horizontal and vertical momentum equations to add two more equations containing only θ'_ρ terms. This yields the final set of equations, containing two equations for π', two equations for θ'_ρ, and one equation for both variables:

$$\frac{1}{c_p\bar{\theta}_\rho}\left(\frac{\partial u}{\partial t}+u\frac{\partial u}{\partial x}+v\frac{\partial u}{\partial y}+w\frac{\partial u}{\partial z}-fv\right)+\frac{\partial\bar{\pi}}{\partial x}=A=-\frac{\partial\pi'}{\partial x} \tag{13}$$

$$\frac{1}{c_p\bar{\theta}_\rho}\left(\frac{\partial v}{\partial t}+u\frac{\partial v}{\partial x}+v\frac{\partial v}{\partial y}+w\frac{\partial v}{\partial z}+fu\right)+\frac{\partial\bar{\pi}}{\partial y}=B=-\frac{\partial\pi'}{\partial y} \tag{14}$$

$$\frac{1}{c_p\bar{\theta}_\rho}\left(\frac{\partial w}{\partial t}+u\frac{\partial w}{\partial x}+v\frac{\partial w}{\partial y}+w\frac{\partial w}{\partial z}\right)=C=-\frac{\partial\pi'}{\partial z}+\frac{g}{c_p\bar{\theta}_\rho^2}\theta'_\rho \tag{15}$$

$$\frac{-c_p\bar{\theta}_\rho^2}{g}\left(\frac{\partial A}{\partial z}-\frac{\partial C}{\partial x}\right)=D=\frac{\partial\theta'_\rho}{\partial x} \tag{16}$$

$$\frac{-c_p\bar{\theta}_\rho^2}{g}\left(\frac{\partial B}{\partial z}-\frac{\partial C}{\partial y}\right)=E=\frac{\partial\theta'_\rho}{\partial y} \tag{17}$$

The time tendency terms are difficult to quantify from real data. Hence, we will neglect them in general, with further analysis of that assumption described later in the verification section. To solve these equations, we minimize an incremental form of a variational cost function using a conjugate gradient algorithm identical to the approach used in SAMURAI. The control variable state vector takes the shape of $\mathbf{x}=\{\pi',\theta'\}$.

There are several distinctions in this approach compared to previous methods. The reference state definition varies with radius and height to account for the tropical cyclone environment. The cost function minimization algorithm has an efficient filtering mechanism to control the resolved scales, eliminating the need for smoothing penalty constraints in the cost function itself. The use of the cubic B-spline basis for the underlying representation of the thermodynamic structure provides several benefits over a grid point representation. In this approach the thermodynamic structure is represented by a series of nodal coefficients that determine the amplitude of overlapping cubic B-spline finite elements. The first and second spatial derivatives of the structure in all three dimensions are therefore exact for a given set of nodal coefficients, providing higher numerical accuracy than a finite-difference representation of the derivatives. The variational analysis is obtained by solving directly for the nodal

coefficients that give consistent pressure and temperature gradients in Equations 12 - 17, indirectly producing a three-dimensional function that represents the pressure and temperature itself. Using this approach, the seminal problem of linking vertical levels in the retrieval is accomplished without the necessity of an arbitrary constant at each level (Gal-Chen, 1978), without the necessity of microphysical constraints (Roux et al., 1993), and without the necessity of the thermodynamic equation (Liou et al., 2003). A thorough verification of this new thermodynamic retrieval methodology is presented in the next chapter.

3 Retrieval Evaluation

The performance of the newly developed thermodynamic retrieval is assessed and its uncertainties are quantified using a WRF simulation of Hurricane Rita. The WRF simulation provides both kinematic and thermodynamic variables, thus it is possible to evaluate the thermodynamic quantities derived from the model's kinematic fields with the thermodynamic fields of the model.

3.1 Data

The simulation uses version 3.6.1 of WRF with four nested domains of 18, 6, 2 and 2/3 km resolution and 300, 250, 250 and 400 grid points square, respectively. The three inner domains are vortex-following using the pressure minimum at 700 hPa. The simulation uses the following physics parameterizations: rapid and accurate radiative transfer model (RRTM) long wave radiation (Mlawer et al., 1997), Dudhia shortwave radiation (Dudhia, 1989), the Noah land-surface model (Ek et al., 2003), the Yonsei University boundary layer scheme (Hong et al., 2006), Thompson aerosol-aware microphysics (Thompson and Eidhammer, 2014) and modified surface fluxes for tropical cyclones (Garratt formulation; Davis et al. (2008)). The outer two domains use the Kain-Fritsch cumulus parameterization (Kain and Fritsch, 1990) while the inner two domains resolve convection explicitly. The WRF simulation was run from 18 - 23 September, and captured both the period of rapid intensification and the secondary eyewall formation of Hurricane Rita.

Figures 8 and 9 show the evolution of Hurricane Rita in the WRF simulation from 0000 UTC 20 September to 1800 UTC 21 September, during which Rita strengthens from a Category-1 to a Category-5 hurricane.The evaluation of the retrieval will focus on this period. At 0000 UTC 20 September, the simulated storm is a category-1 hurricane. The convection is concentrated in a broad region in the southern half of the domain, at a radius of about 30 km. By 0000 UTC 21 September, Rita strengthens to a category-3 hurricane. The eyewall is concentric, with the most active convection to the south. Rita further strengthens and becomes a category-5 hurricane at 1800 UTC 21 September. The radius of the eyewall radius shrinks to about 20 km, and a secondary eyewall is visible at a radius of about 50 km.

The sigma-level output of the innermost WRF domain was converted to Cartesian coordinates using SAMURAI for the eight time steps shown in Fig. 8, equivalent to step 1 of the retrieval method. In contrast to a wind field derived from observations, however, the wind field here does not contain any errors. The resolution of the Cartesian grid is 1-km in the

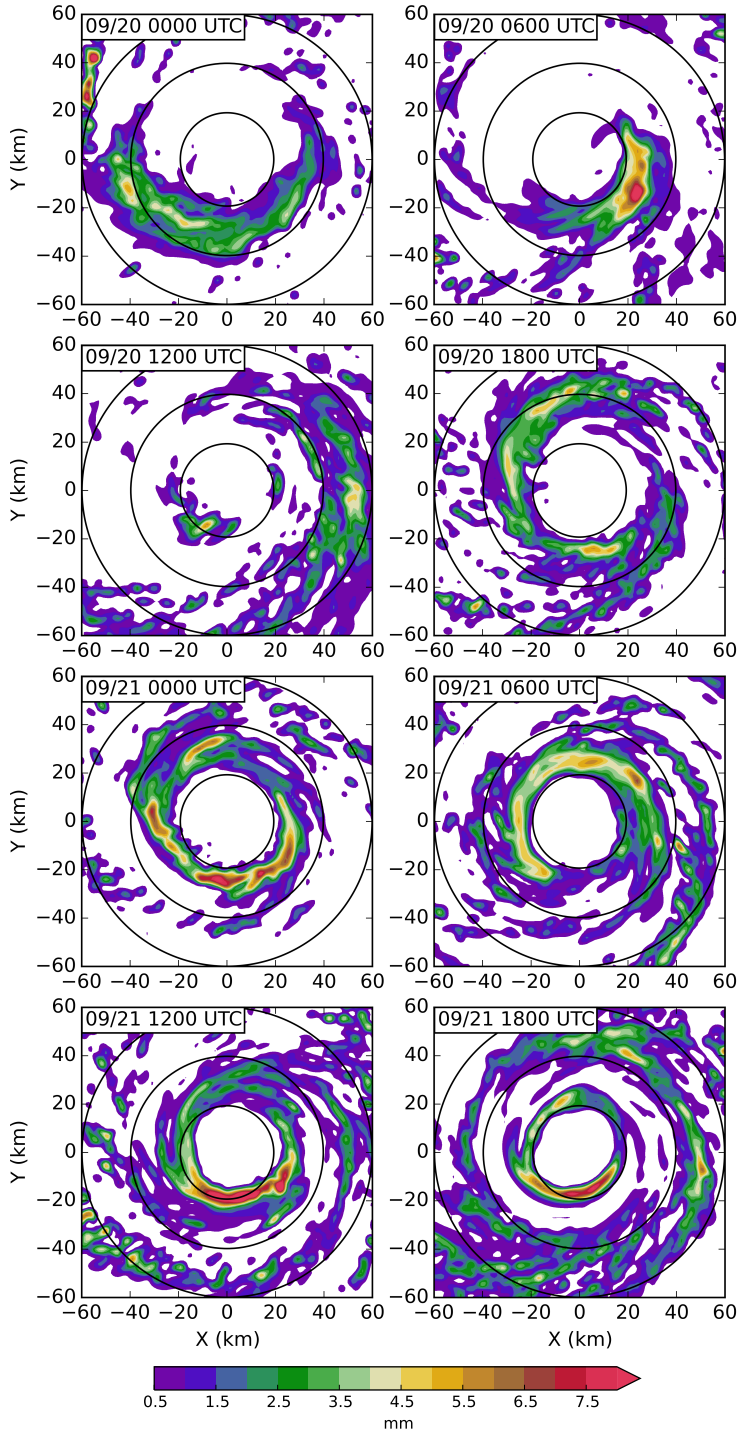

Figure 8: *Horizontal cross sections of WRF precipitation mixing ratio at 2 km altitude (shaded, g kg^{-1}) from 0000 UTC 20 September 2005 to 1800 UTC 21 September in increments of 6 hours. Black solid circles represent range rings of 20, 40, and 60 km around the storm center.*

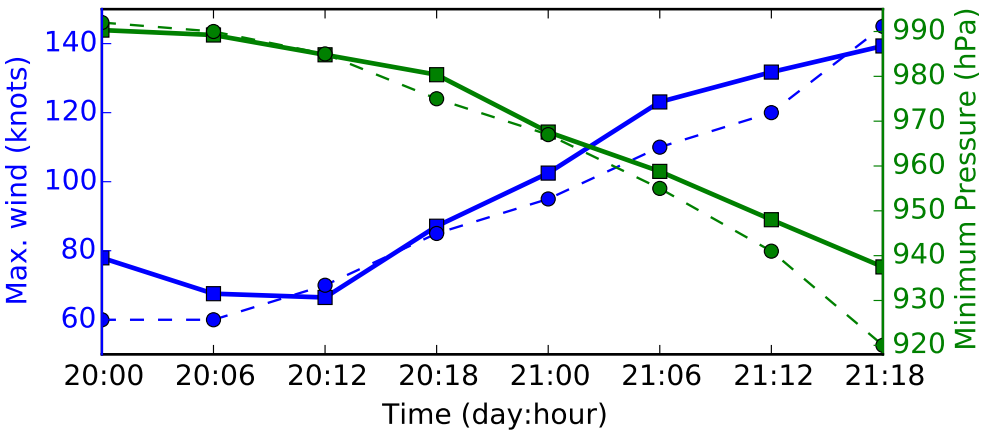

Figure 9: *WRF maximum 2km-altitude wind speed (blue solid, knots) and best track 1-min sustained wind speed (blue dashed, knots), and WRF minimum sea level pressure (green solid, hPa) and best track minimum sea level pressure (green dashed, hPa) for the times shown in Fig. 8.*

horizontal and 0.5-km in the vertical, with a domain size of 150 km x 150 km x 16 km. The balanced vortex reference state is calculated from the gridded SAMURAI analyses according to step 2 of the retrieval method. The wind field of step 1 and the reference pressure and temperature fields of step 2 are then used as input for the retrieval of the temperature and pressure perturbations in step 3.

3.2 Retrieval Equations

The retrieval equations neglect sub-grid scale processes and friction. This simplification is justified if the residuals of the retrievals equations are small, or in other words, if the left-hand side and the right-hand side of the retrieval equations are approximately equal.

The impact of sub-grid scale processes and friction is small for the pressure retrieval, as exemplified by equation 13. The main patterns of the left-hand side and the right-hand side of the equation are very similar (Figs. 10a, 10b). However, the kinematic (left-hand) side shows more structure, higher maximum values and non-zero values at larger radii, compared to the smoother thermodynamic (right-hand) side. The pressure retrieval (Fig. 10c) resolves the main features of the pressure gradient pattern. At larger radii, it looks more similar to the thermodynamic WRF variables than the kinematic WRF variables, with a smoother pattern and more values close to zero. The sensitivity of the retrieval to the input resolution was tested by smoothing the WRF fields (Fig. 10d) by increasing the spline filter length

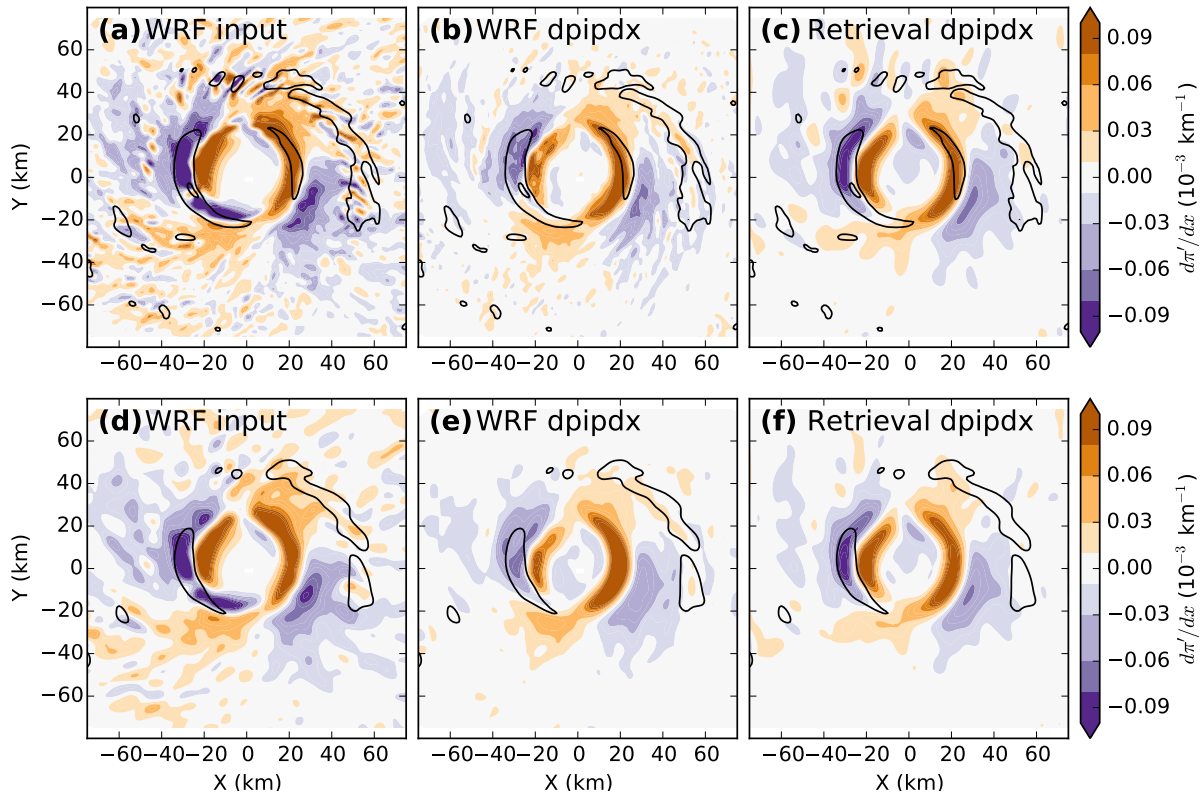

Figure 10: *Comparison of different terms of the pressure retrieval equation in x-direction at 8 km altitude for 1800 UTC 21 September 2005: (a) left-hand side of equation 13 as calculated from the WRF output, (b) right-hand side of equation 13 calculated from the thermodynamic WRF output, and (c) horizontal derivative of the retrieved pressure. (d-f) are the same as (a-c), but for smoothed input fields.*

from 4 to 10 grid points in step 1 of the retrieval. The retrieved pressure gradient field (Fig. 10f) looks almost identical to the one retrieved from the higher-resolution input. These results show that it is justified to neglect sub-grid scale processes and friction in the pressure retrieval equations above the boundary layer and that the pressure retrieval of mesoscale features is not sensitive to small-scale variations in the kinematic input fields.

The input fields for the temperature retrieval are a combination of the derivatives of the horizontal and vertical momentum equations, thus, they are inherently more noisy than the input fields for the pressure retrieval. The patterns of the left-hand side and the right-hand side of equation 16 look similar in the eyewall region, but the left-hand side shows much more structure at outer radii (Fig. 11a), with a lot of small-scale variability, whereas the right-hand side (Fig. 11b) shows values near zero outside the eyewall region. The retrieval

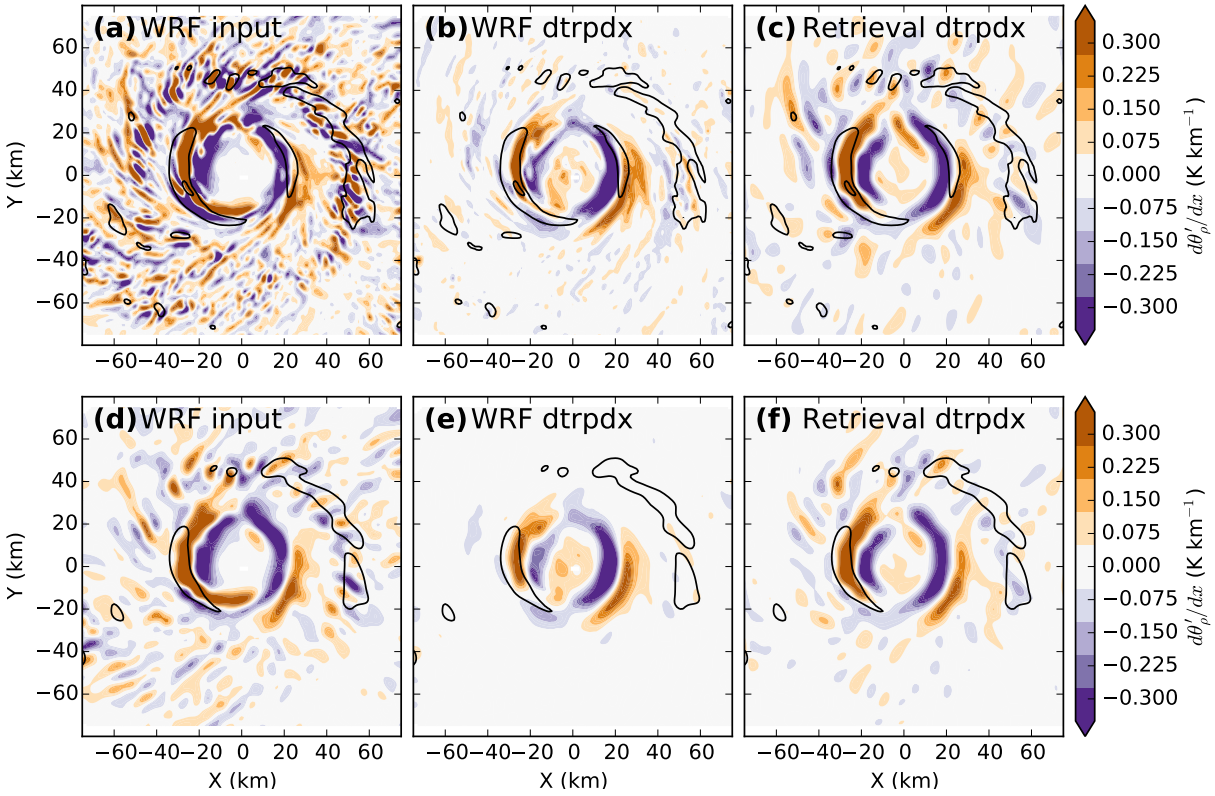

Figure 11: *Comparison of different terms of the temperature retrieval equation in x-direction at 8 km altitude for 1800 UTC 21 September 2005: (a) left-hand side of equation 16 as calculated from the WRF output, (b) right-hand side of equation 16 calculated from the thermodynamic WRF output, and (c) horizontal derivative of the retrieved pressure. (d-f) are the same as (a-c), but for smoothed input fields.*

(Fig. 11c) gets rid of most of the small-scale variability in the WRF kinematic input fields and resembles the WRF thermodynamic field more closely. However, some of the variability outside the eyewall region is still visible. Smoothing the input field (Fig. 11d) removes a lot of the small-scale variability in the input, but, as with the pressure retrieval, the temperature retrieval remains largely unchanged.

Comparison of the left-hand and right-hand sides of the retrieval equations using horizontal cross sections shows that neglecting sub-grid scale processes and friction above the boundary layer is justified and that smoothing the input fields can improve the retrieval slightly, but is a non-necessary pre-processing step. The retrieval's built-in smoothing is sufficient to filter out most of the small-scale variations. The retrieval performs best in the eyewall region, where the gradients are largest and mesoscale features of interest are broader.

3.3 Pressure Retrieval

The first and last snapshot in Fig. 8 are used to illustrate the retrieval performance at different storm intensities. A comparison of the WRF and the retrieved total normalized pressure π (Fig. 12a, 12b) at the earlier time (0000 UTC 20 September) shows very good overall agreement between the retrieved pressure and the WRF pressure, with a prominent pressure drop towards the center of the storm.

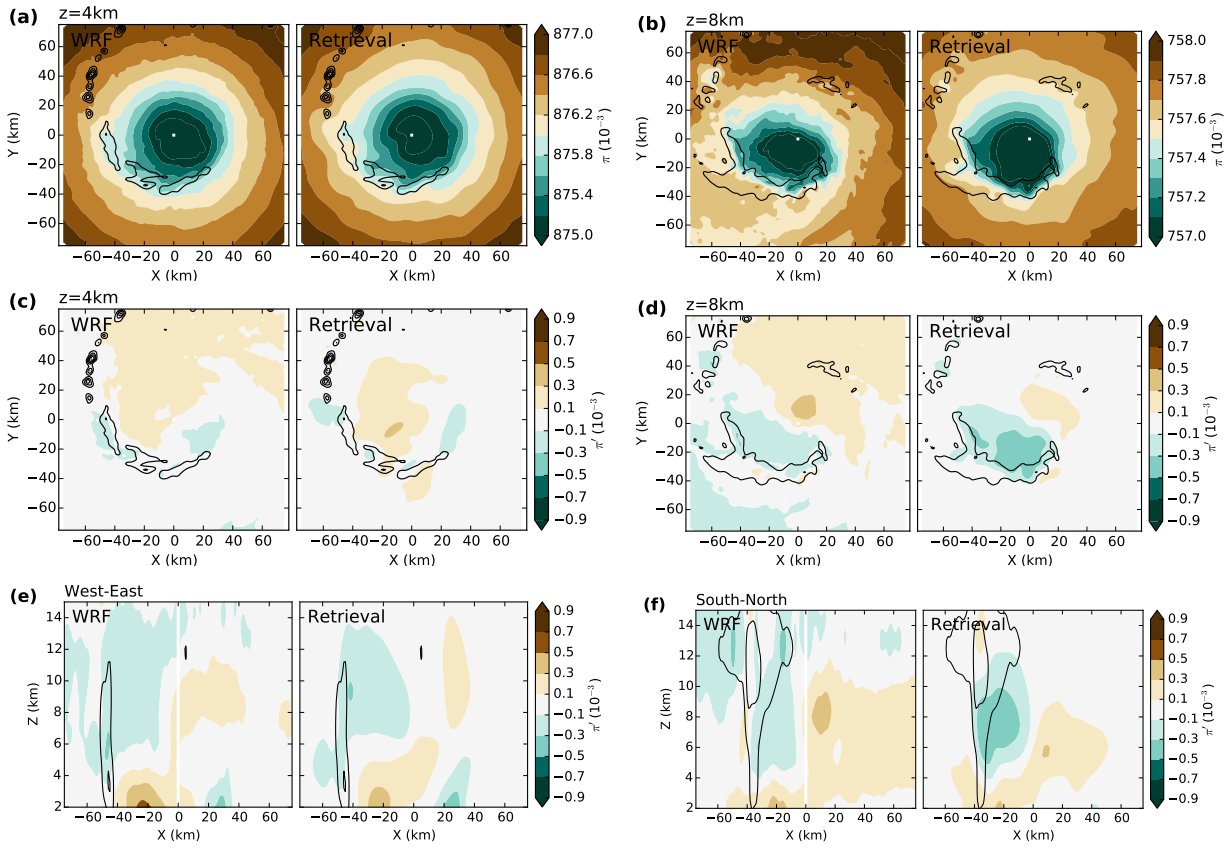

Figure 12: *Comparison of WRF output and pressure retrieval output for 0000 UTC 20 September 2005. (a)-(b) Horizontal cross sections of normalized pressure π (shaded, 10^{-3}) and (c)-(d) horizontal and (e)-(f) vertical cross sections of normalized pressure perturbation π' (shaded, 10^{-3}) at (a), (c) 4 km altitude and (b), (d) 8 km altitude. Contours of precipitation mixing ratio (g kg^{-1}, in increments of 3 g kg^{-1}) are included for easier comparison.*

The total normalized pressure π is the sum of the mean normalized pressure $\bar{\pi}$ calculated from the mean tangential wind field in step 2 of the retrieval method, and the normalized pressure perturbation retrieved in step 3. The spatial correlation coefficient (SCC, Liou (2001)) of the total normalized pressure at this earlier time is a perfect 1.000 (Table 1).

The retrieval performs slightly better at 4 km than at 8 km, which can be attributed to issues with the boundary conditions due to the asymmetric pressure structure at outer radii at 8 km altitude. The perturbation pressure π' reveals the small variations in the pressure field that are largely masked in the total pressure field by the prominent radial pressure drop. The horizontal cross sections of π' at 4 km and 8 km (Fig. 12c, 12d) show that the retrieval correctly identifies the regions of positive and negative perturbations along with the perturbation magnitudes. At 4 km (Fig. 12c), both WRF and retrieval show a broad positive region, accompanied by two small negative areas. At 8 km (Fig. 12d), the retrieval correctly places the negative perturbation just inside the area of convection, with a positive perturbation towards its northeast. The perturbations towards the domain boundaries are not resolved. The vertical cross sections (Fig. 12e, 12f) show good agreement between the WRF pressure perturbations and the retrieved pressure perturbations. Locations and magnitudes are depicted correctly, with small discrepancies towards the boundaries, where the retrieval tends towards zero and the WRF simulation displays non-zero values.

At the latter time, 1800 UTC 21 September (Fig. 13), the magnitude of the mean pressure drop and the magnitude of the perturbations are much larger. The mean normalized pressure drop at 4 km is about 13 x 10^{-3} compared to 2 x 10^{-3} at the earlier time, and the perturbations now cover more than twice the range compared to the earlier time. Again, the retrieved total normalized pressure π (Fig. 13a, 13b) shows very good agreement with the WRF simulation at both vertical levels. The retrieval correctly identifies the pronounced wavenumber-1 pattern in the pressure perturbation π' at both vertical levels (Fig. 13c, 13d), with the maximum negative perturbation collocated with the ring of convection at 4 km altitude. As at the earlier time, the perturbations towards the boundaries are smaller than in the WRF simulation. The vertical cross sections (Fig. 13e, 13f) show the collocation of the negative pressure perturbations with the eyewall convection at all vertical levels, and the positive perturbations located slightly further radially outward, in both the WRF simulation and the retrieval.

Cross sections for the earlier and the latter time indicate a good performance of the pressure retrieval. Statistical measures for all 8 different timesteps confirm the performance (Table 1). The root-mean-square (RMS) of the normalized pressure perturbation π' is used as a measure for the perturbation magnitude. The RMS of the retrieval and the WRF simulation are of similar magnitude and increase with increasing strength of the vortex, with the retrieval RMS increasing from 0.08 to 0.29 x 10^{-3} and the WRF RMS increasing from 0.13 to 0.37 x 10^{-3}. The root-mean-squared error (RMSE) ranges from 0.1 to 0.18 x 10^{-3}, which corresponds

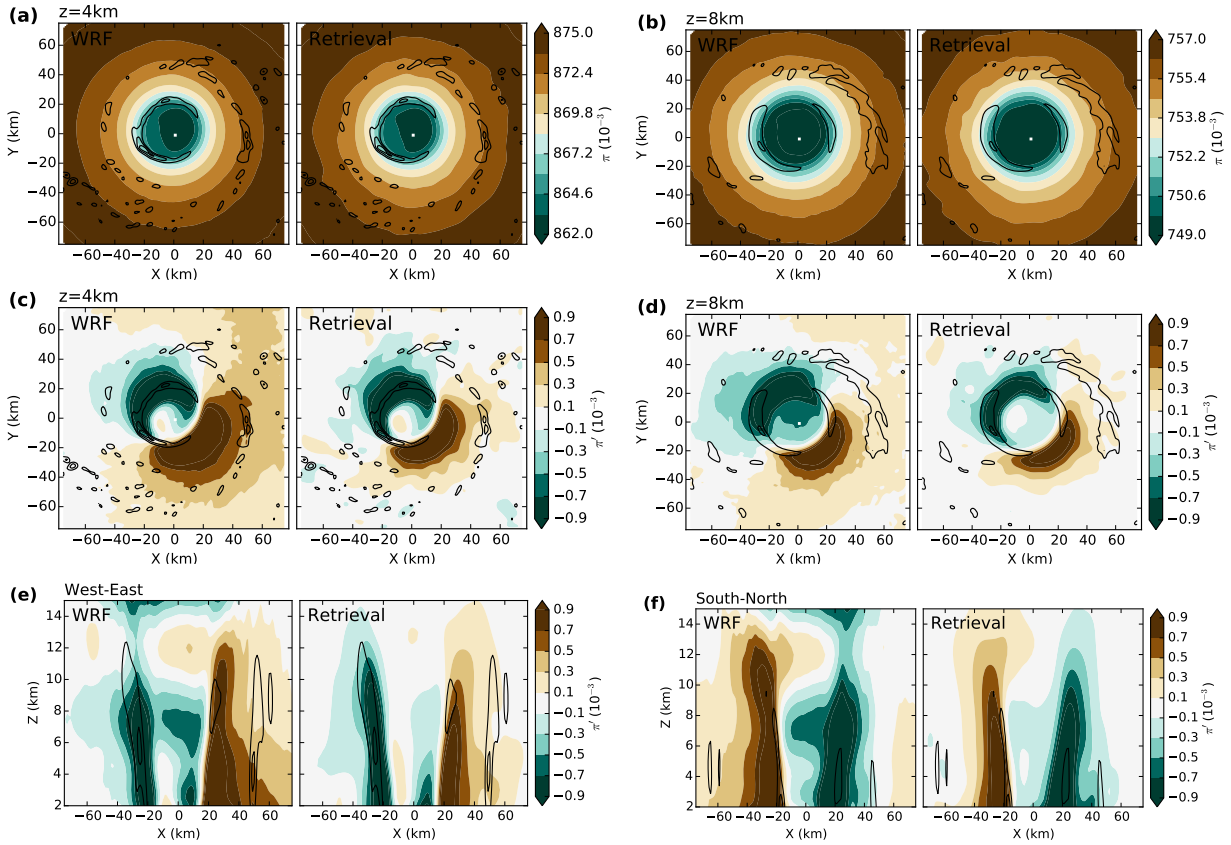

Figure 13: *Comparison of WRF output and pressure retrieval output for 1800 UTC 21 September 2005. (a)-(b) Horizontal cross sections of normalized pressure π (shaded, 10^{-3}) and (c)-(d) horizontal and (e)-(f) vertical cross sections of normalized pressure perturbation π' (shaded, 10^{-3}) at (a), (c) 4 km altitude and (b), (d) 8 km altitude. Contours of precipitation mixing ratio (g kg^{-1}, in increments of 3 g kg^{-1}) are included for easier comparison.*

to an RMSE of approximately 0.4 hPa. The spatial correlation coefficient for the total normalized pressure shows a perfect score of 1.0 at a precision of three significant digits. The SCC for the pressure perturbations is always above 0.5, and generally increases with increasing storm intensity. The two times that perform worse than expected (1800 UTC 20 September and 0000 UTC 21 September) also exhibit low RMS values, which indicates that the retrieval is more challenging when perturbation magnitudes are small. The last column of the table adds a metric to evaluate how well the retrieval is able to correctly identify the areas with significant positive or negative anomalies. Retrieving small pressure and temperature perturbations is challenging and inherently contains uncertainties. The scientific interpretation of the perturbation fields in later chapters will focus on the patterns and the relative magnitudes of the perturbations rather than the exact magnitudes of the

Table 1: *Statistics for the evaluation of the pressure retrieval against the WRF output in terms of normalized pressure π (10^{-3}) and normalized pressure perturbation π' (10^{-3}) for eight different times (0000 UTC 20 September 2005 to 1800 UTC 21 September 2005): root-mean square of π' for retrieval (RMS TD) and WRF output (RMS WRF), root-mean-square error of π' (RMSE), spatial correlation coefficients (SCC) for π and π', and the percentage of grid points with correctly retrieved sign (% sign). See text for details about the calculation of the SCC and the % sign.*

dd hh UTC	RMS TD	RMS WRF	RMSE	SCC π	SCC π'	% sign
20 00 UTC	0.08	0.13	0.11	1.000	0.51	0.94
20 06 UTC	0.08	0.12	0.10	1.000	0.53	0.91
20 12 UTC	0.11	0.14	0.10	1.000	0.75	0.86
20 18 UTC	0.08	0.14	0.12	1.000	0.48	0.82
21 00 UTC	0.09	0.13	0.11	1.000	0.63	0.87
21 06 UTC	0.15	0.22	0.14	1.000	0.79	0.89
21 12 UTC	0.29	0.37	0.18	1.000	0.88	0.85
21 18 UTC	0.29	0.37	0.17	1.000	0.91	0.93

perturbations at any given point. Thus, the '% sign' metric calculates the percentage of the grid points for which the retrieval correctly determines the sign of the perturbation, using only grid points where the retrieved (positive or negative) pressure perturbation exceeds 0.1 x 10^{-3} (which is the shading threshold for all pressure perturbation plots). The metric shows that the sign is determined correctly for over 80% of the grid points in all cases, exceeding 90% in three cases. The two times with lower SCC values (1800 UTC 20 September and 0000 UTC 21 September) also perform at over 80%, again pointing to the fact that the perturbations were small in these cases. Overall, both visual inspection and statistical evaluation confirm the good performance of the pressure retrieval.

3.4 Temperature Retrieval

The temperature retrieval performance is examined in detail for the same two times as the pressure retrieval, 0000 UTC 20 September and 1800 UTC 21 September. The total density potential temperature θ_ρ is the sum of the mean density potential temperature $\bar{\theta_\rho}$ calculated from the mean tangential wind field in step 2 of the retrieval method, and the density potential temperature perturbations θ'_ρ retrieved in step 3.

At the earlier time, comparison between the WRF and the retrieval total density potential temperature θ_ρ at 4 km (Fig. 14a) shows that the retrieval correctly identifies the location of the temperature maximum and the overall structure of the temperature field. The tem-

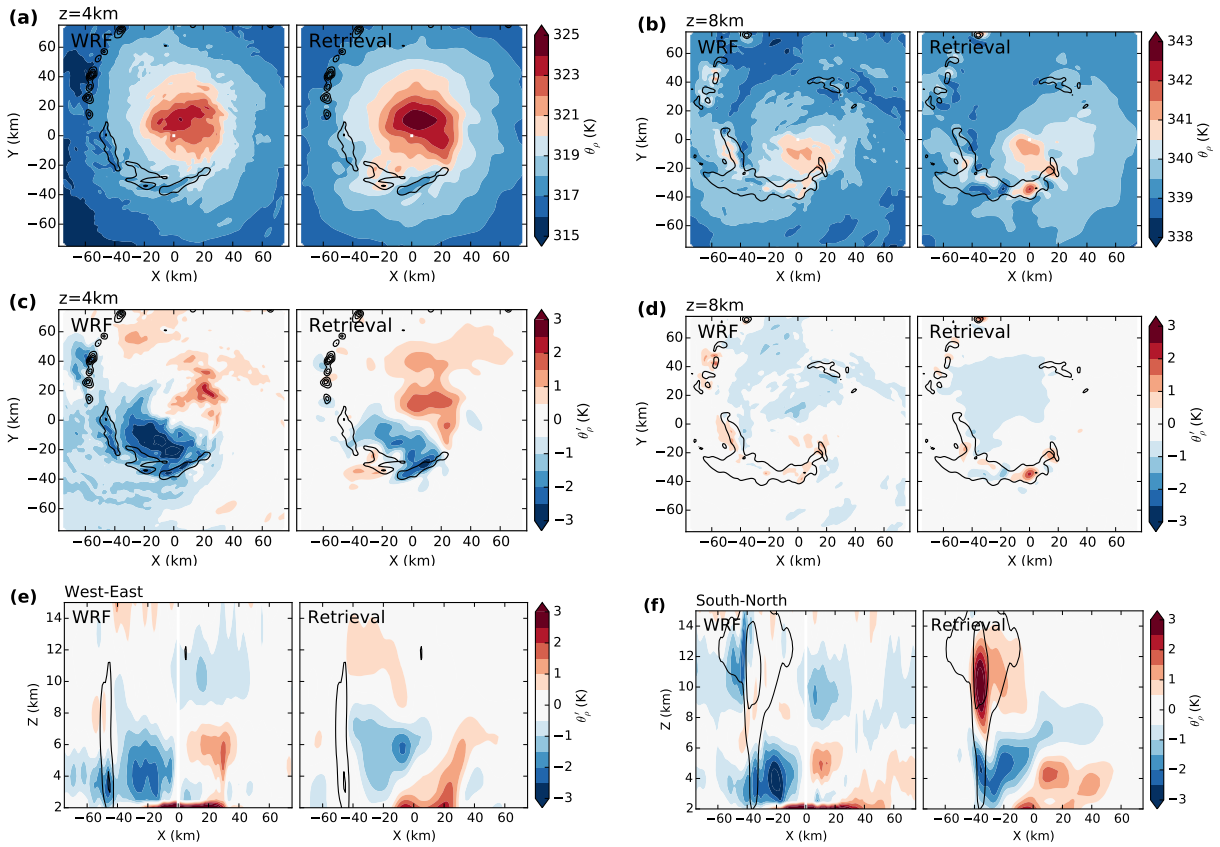

Figure 14: *Comparison of WRF output and temperature retrieval output for 0000 UTC 20 September 2005. (a)-(b) Horizontal cross sections of density potential temperature θ_ρ (shaded, K) and (c)-(d) horizontal and (e)-(f) vertical cross sections of density potential temperature perturbation θ'_ρ (shaded, K) at (a), (c) 4 km altitude and (b), (d) 8 km altitude. Contours of precipitation mixing ratio (g kg^{-1}, in increments of 3 g kg^{-1}) are included for easier comparison.*

perature maximum in the WRF simulation is shifted southward at 8 km compared to the lower level, which is also reflected in the retrieval (Fig. 14b). Subtracting off the balanced temperature contribution reveals a wavenumber-1 pattern in the temperature perturbation field θ'_ρ at 4 km (Fig. 14c), with negative perturbations just inside the convection to the southwest and positive perturbations northeast of it. The retrieval correctly identifies this wavenumber-1 pattern, but some small discrepancies occur. The retrieval is smoother than the WRF simulation and underestimates the small negative perturbation towards the southwestern boundary. The perturbations at 8 km (Fig. 14d) are relatively small. The WRF simulation and the retrieval both show an extended negative area in the northern half of the domain and small positive areas within the region of convection. Vertical cross sections

(Fig. 14e, 14f) show a good agreement of the WRF simulation and the retrieval up to about 8 km. Above that, the retrieved temperature perturbations in the west-east cross section seem to have a slight positive bias. The south-north cross section shows a pronounced positive perturbation collocated with the maximum reflectivities at 9-12 km height, which is not apparent in the WRF simulation.

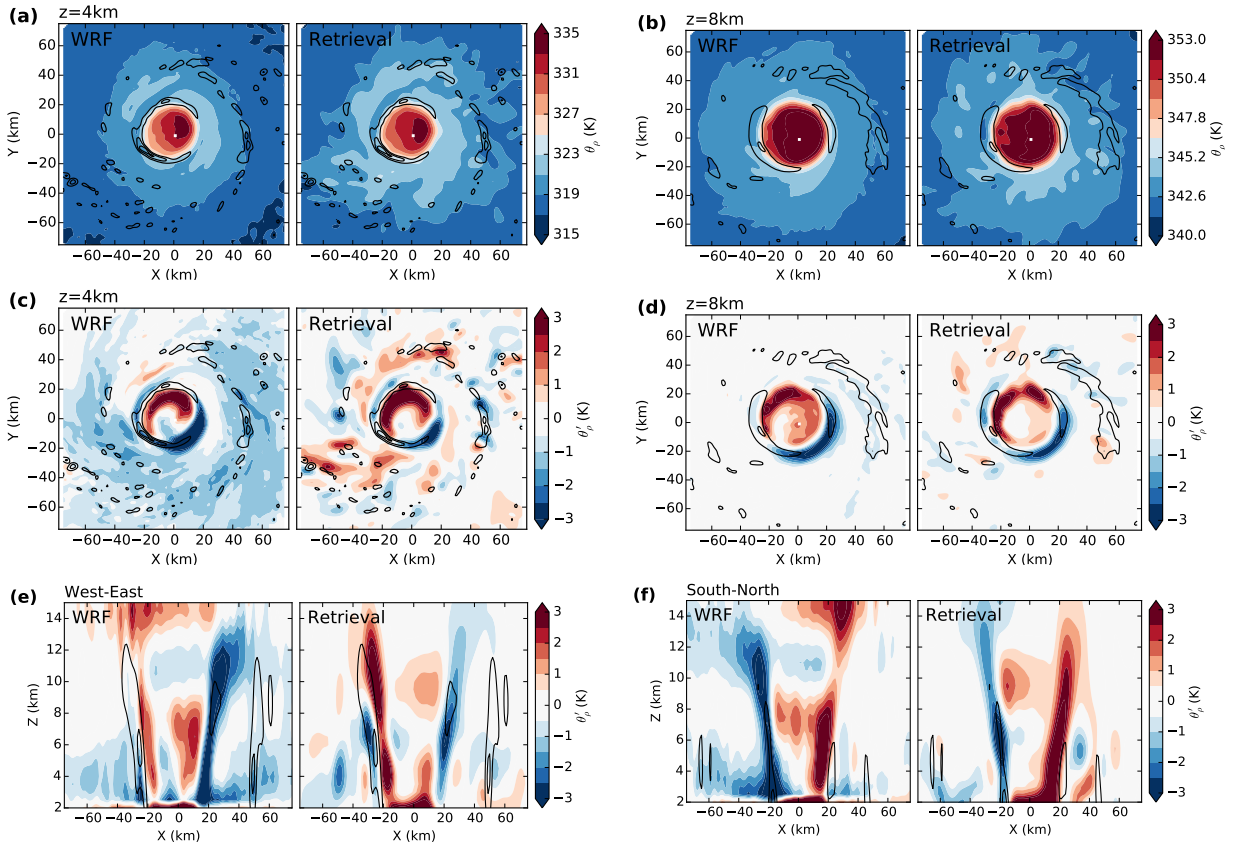

Figure 15: *Comparison of WRF output and temperature retrieval output for 1800 UTC 21 September 2005. (a)-(b) Horizontal cross sections of density potential temperature θ_ρ (shaded, K) and (c)-(d) horizontal and (e)-(f) vertical cross sections of density potential temperature perturbation θ'_ρ (shaded, K) at (a), (c) 4 km altitude and (b), (d) 8 km altitude. Contours of precipitation mixing ratio (g kg^{-1}, in increments of 3 g kg^{-1}) are included for easier comparison.*

At the latter time, 1800 UTC 21 September, the total temperature difference between the domain boundary and the center is approximately 20 K, compared to 10 K at the earlier time, and the magnitudes of the temperature perturbations increase from about 1.5 K to over 3 K. The retrieval of the total density potential temperature looks very good (Fig. 15a, 15b). Subtracting off the balanced temperature contribution shows that the main regions

Table 2: *Statistics for the evaluation of the temperature retrieval against the WRF output in terms of density potential temperature θ_ρ (K) and density potential temperature perturbation θ'_ρ (K) for eight different times (0000 UTC 20 September 2005 to 1800 UTC 21 September 2005): root-mean square of θ'_ρ for retrieval (RMS TD) and WRF output (RMS WRF), root-mean-square error of θ'_ρ (RMSE), spatial correlation coefficients (SCC) for θ_ρ and θ'_ρ, and the percentage of grid points with correctly retrieved sign (% sign). See text for details about the calculation of the SCC and the % sign.*

dd hh UTC	RMS TD	RMS WRF	RMSE	SCC θ_ρ	SCC θ'_ρ	% sign
20 00 UTC	0.43	0.66	0.59	0.999	0.50	0.80
20 06 UTC	0.53	0.78	0.62	0.999	0.61	0.85
20 12 UTC	0.43	0.61	0.56	0.999	0.47	0.77
20 18 UTC	0.38	0.60	0.65	0.999	0.19	0.59
21 00 UTC	0.45	0.72	0.75	0.999	0.25	0.59
21 06 UTC	0.54	0.74	0.73	0.999	0.38	0.68
21 12 UTC	0.73	0.88	0.73	0.999	0.60	0.72
21 18 UTC	0.71	0.92	0.84	0.999	0.53	0.70

of perturbation are linked to the eyewall, with a narrow arc of positive values toward the northwest of the center and a narrow arc of negative values towards the southeast but at a slightly larger radius. This pattern is prominent in both the WRF simulation and the retrieval at 4 km (Fig. 15c) and at 8 km (Fig. 15d). The pattern outside the eyewall region is close to zero in WRF simulation and retrieval at 8 km, but it differs at 4 km. The WRF retrieval has mostly negative values outside the eyewall region, whereas the retrieval shows a more diverse pattern. The vertical cross sections show that the temperature anomalies are closely tied to the convection. In the western and northern eyewall the positive anomalies are located inside the eyewall in both WRF simulation and the retrieval (Fig. 15e, 15f). In the eastern and southern eyewall the negative anomalies are collocated with the convection in both WRF simulation and the retrieval. Small discrepancies between WRF simulation and retrieval are apparent in the center, where the positive temperature perturbation is located higher up (8-11 km) in the retrieval than in the WRF simulation (6-8 km). Moreover, the columns of positive perturbation in the western and northern eyewall are deeper in the retrieval, whereas the WRF simulation has a minimum at around 10 km height and increasing values above.

Table 2 summarizes the performance of the temperature retrieval. The retrieval does show skill, especially at higher storm intensities. However, the temperature retrieval is more challenging than the pressure retrieval, which manifests in the verification. The retrieval RMS values for θ'_ρ range from 0.38 K to 0.73 K, the WRF simulation RMS values are

slightly higher, ranging from 0.60 K to 0.92 K. The RMSE values are well below 1 K, ranging from 0.56 K to 0.85 K. The spatial correlation of the total temperature field θ_ρ is almost perfect with a value of 0.999 in all eight cases. The spatial correlation of the perturbation temperature field θ'_ρ reaches values of 0.19 to 0.61. These values are slightly lower than the SCC values for π', indicating that the temperature retrieval is more challenging than the pressure retrieval. The last column again contains the metric calculating the percentage of points where the retrieval correctly determines the sign of the perturbation, but only using points where the retrieved (positive or negative) temperature perturbation exceeds 0.5 K (which is also the shading threshold in all temperature perturbation plots). The percentage of correctly identifying the sign is well above 0.5 in every case and as high as 0.85. The lowest scores occur at the same two times as for the pressure retrieval, and again the retrieval RMS magnitudes are comparatively low in these cases, indicating that the retrieval performance is poorer when the perturbations are small.

3.5 Sensitivity Tests

The evaluation of the retrieval in the previous section yielded good results. The robustness of these results with respect to the resolution of the input and with respect to the formulation of the time tendency term is tested in this section.

3.5.1 Input Resolution

The retrieval equations contain the temperature and pressure gradients. Hence, smoothing the input field yields smaller gradients and probably a smoother retrieval output. This smoothing effect is illustrated in Figs. 16 and 17 for the temperature perturbations. The pressure perturbations exhibit a similar behavior (not shown).

The top panels (Figs. 16a and 17a) show the original WRF simulation and retrieval (as in Figs. 14, 15), respectively, where the input field was smoothed with a spline cutoff length scale of 4 grid points. The bottom panels (Figs. 16b and 16b) show the smoother WRF simulation and retrieval, where all WRF fields were smoothed with a spline cutoff length scale of 10 grid points. The larger spline cutoff length scale results in fields with less structure and lower maximum values. The dipole pattern at 0000 UTC 20 September (Fig. 16) is evident in all four panels, but the maximum values which exceed 2 K in the top panels are about 1 K less in the bottom panels. Moreover, the top panels show multiple local maxima and minima, whereas the bottom panels show only one maximum and one minimum.

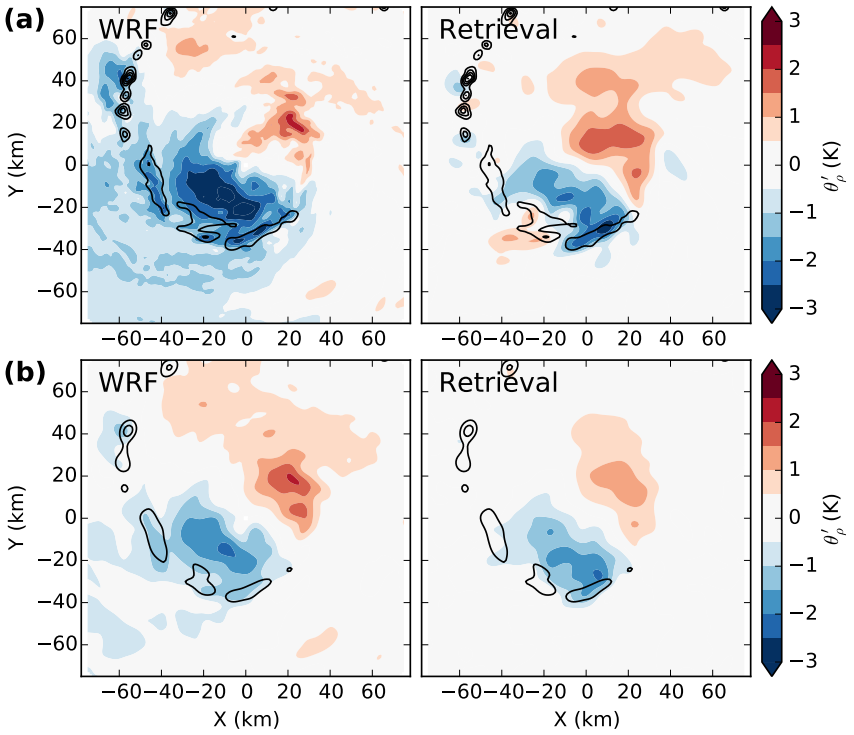

Figure 16: *Comparison of WRF output and temperature retrieval output for 0000 UTC 20 September 2005 at 4 km altitude for different input resolutions. Density potential temperature perturbation θ'_ρ (shaded, K) (a) as in Fig. 14 and (b) with smoothed input as described in the text.*

The temperature perturbations at the latter time, 1800 UTC 21 September, show a similar pattern. The main pattern of the two ring-like features is captured in all four panels, but the top panels show a lot more detail, with narrower, more intense rings. The retrieval with the smoothed input outperforms the original retrieval. The RMSE values decrease from 0.59 K to 0.46 K for the earlier case, and from 0.84 K to 0.59 K in the latter case. The SCC for θ'_ρ increases from 0.5 to 0.59 for the earlier case, and from 0.53 to 0.73 in the latter case. The sign percentage increases from 0.8 to 0.87 for the earlier time, and from 0.70 to 0.85 for the latter time. The RMS values for both the WRF simulation and the retrieval decrease by about 0.1 K for both cases. Hence, if the focus of the retrieval is on the mesoscale patterns, a smoother input field or higher filtering within the retrieval may be preferable. However, if smaller-scale features are of interest, a sufficiently high resolution of the input is necessary, but comes at the cost of lower confidence in the retrieved quantities.

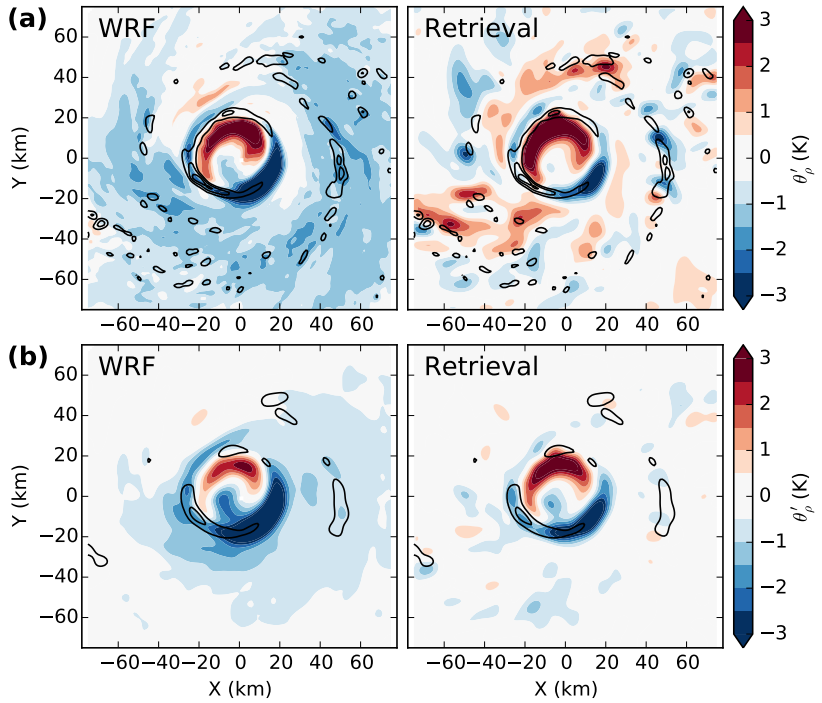

Figure 17: *Comparison of WRF output and temperature retrieval output for 1800 UTC 21 September 2005 at 4 km altitude for different input resolutions. Density potential temperature perturbation θ'_ρ (shaded, K) (a) as in Fig. 15 and (b) with smoothed input as described in the text.*

3.5.2 Time Tendency Term

Guimond et al. (2011) found the results of their latent heat retrieval to be quite sensitive to the time tendency term. While it is desirable to include this term in the retrieval, it is usually not feasible to include when working with airborne radar data. A complete scan of the eyewall using a tail Doppler radar takes on the order of 20 minutes. Even if the flight track allows for two consecutive complete scans, the time tendency term calculated from that is very small because of the large time difference between the two scans. However, it is important to investigate the shortcomings that result from neglecting the time tendency term in the retrieval. Retrievals including the time tendency term were performed, and the time tendency term was calculated from the forward difference for two different intervals, 1-minute and 20-minutes. Comparison of the retrieval output for the different intervals with the WRF simulation and a retrieval run with no time tendency term included shows that the time tendency term changes the retrieval output only slightly (Figs. 18 and 19). The overall patterns of all three retrievals look very similar, however, the 1-min-retrieval captures more detail.

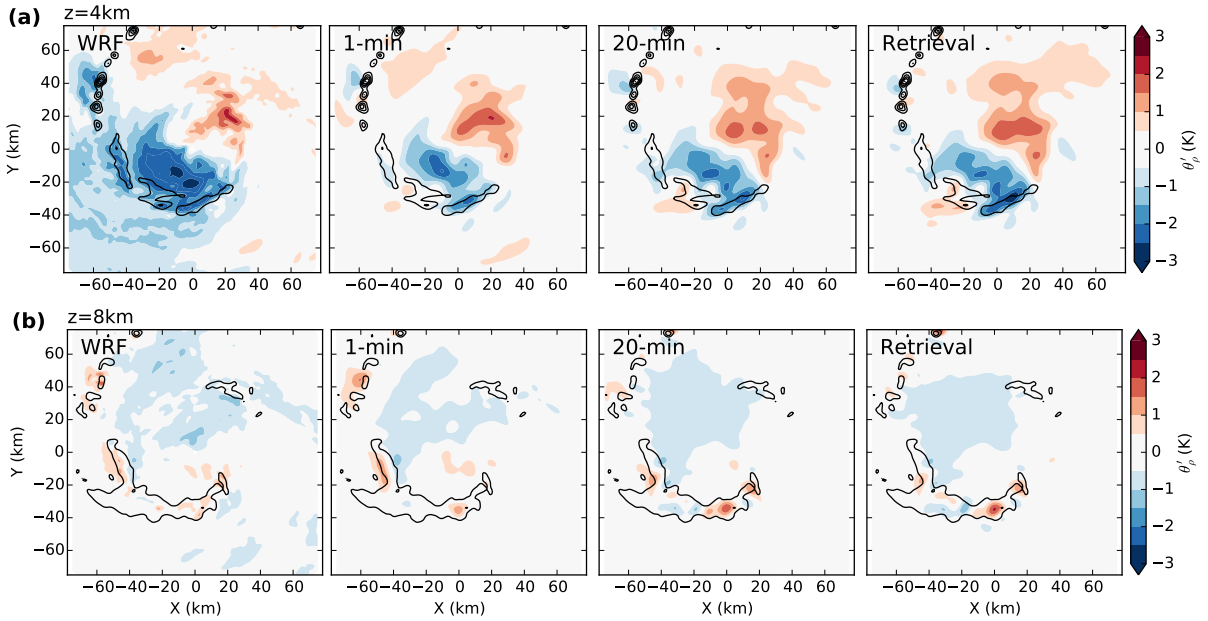

Figure 18: *Comparison of WRF output and output from temperature retrievals including different time tendency terms for 0000 UTC 20 September 2005 at (a) 4 km altitude and (b) 8 km altitude. Density potential temperature perturbation θ'_ρ (shaded, K) is shown (from left to right) for WRF output, retrieval with 1-min time tendency term, retrieval with 20-min time-tendency term, and retrieval without time tendency term.*

At the earlier time, the 1-min-retrieval at 4-km altitude (Fig. 18a) resolves the area of positive perturbation located inward of the convective band toward the upper boundary, whereas this area is not resolved in the 20-min-retrieval or the retrieval without time tendency. Similarly, at 8-km altitude (Fig. 18b), the 1-min-retrieval is the only retrieval that shows structure within the area of negative perturbations north of the center. The other retrievals show a broad area of negative values. The differences between the 20-min-retrieval and the retrieval without time tendency term are subtle.

During the more intense phase of the storm, 1800 UTC 21 September (Fig. 19), the three retrievals again look very similar. At 4 km (Fig. 19a), none of the retrievals correctly depict the broad area of negative perturbations outside the eyewall that is apparent in the WRF simulation. However, they all show an area of positive perturbations spiraling outward outside the northwestern part of the eyewall, and an area of negative values in the northwestern corner of the domain. The 1-min retrieval is relatively smooth, whereas the 20-min retrieval is more cellular. At 8 km (Fig. 19b), non-zero perturbations occur mainly in and around the eyewall. All three retrievals locate these perturbations correctly, however

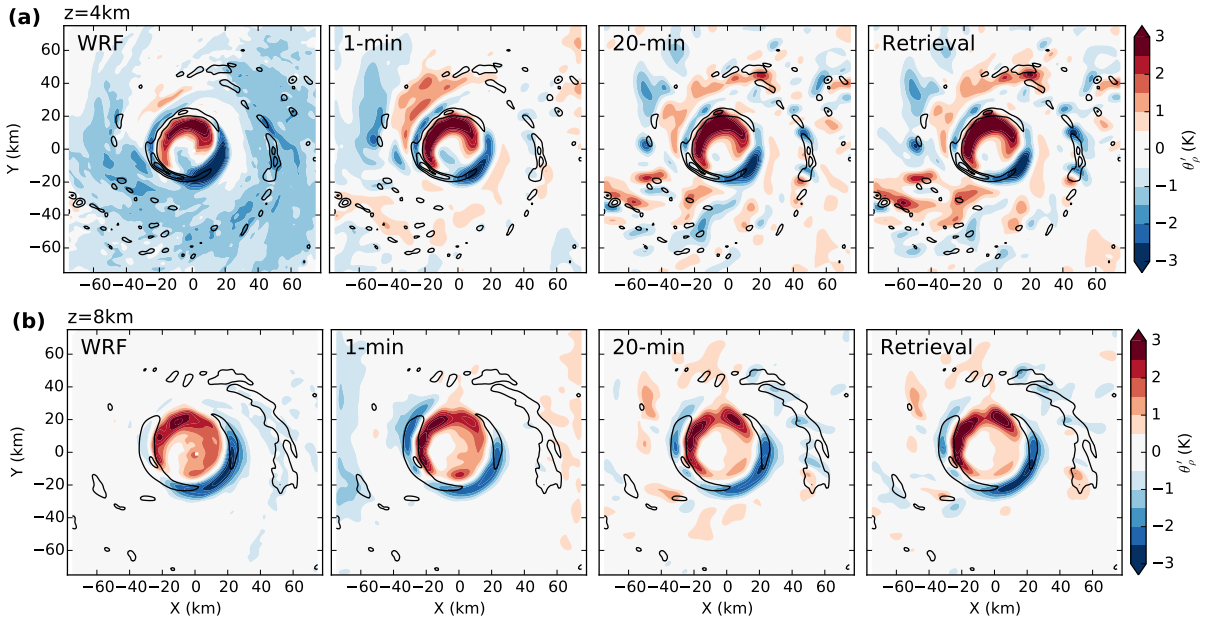

Figure 19: *Comparison of WRF output and output from temperature retrievals including different time tendency terms for 1800 UTC 21 September 2005 at (a) 4 km altitude and (b) 8 km altitude. Density potential temperature perturbation θ'_ρ (shaded, K) is shown (from left to right) for WRF output, retrieval with 1-min time tendency term, retrieval with 20-min time-tendency term, and retrieval without time tendency term.*

they also incorrectly place some smaller-magnitude perturbations outside the eyewall region.

Neglecting the time tendency term degrades the quality of the retrieval only slightly. The only viable option with real data would be to add a 20-min (over even longer period) time tendency term, but adding this term basically did not show any effect with the WRF tests. The results of this sensitivity test stress, however, that it is important to focus the interpretation of the results on the perturbation patterns rather than on the absolute magnitudes of the perturbations.

4 Observed Structure of Hurricane Rita

After the successful validation of the retrieval in the previous chapter, my attention now turns to the application of the retrieval to real data. The structure of a major hurricane in vertical wind shear is examined in terms of its radar-derived kinematic and thermodynamic properties.

4.1 Hurricane Rita

Hurricane Rita formed in the Caribbean as the result of the interaction of a remnant surface trough and a tropical wave. It was first classified as a tropical depression at 0000 UTC 18 September 2005 located north of the Dominican Republic, and intensified to tropical storm strength within the next 18 hours (Figs. 20, 21). It moved northwestward and first strengthened slowly as it approached the Florida Straits, and then strengthened more rapidly afterwards over the very warm waters of the Gulf of Mexico. Within 36 hours, Rita had strengthened from tropical storm to Category-5 status at 1800 UTC 21 September. It reached its estimated peak intensity of 155 knots (and minumum central pressure of 897 mb) by 0300 UTC 22 September, before weakening due to structural changes on 22 September, and increased vertical wind shear and slightly cooler waters on 23 September. Rita made landfall

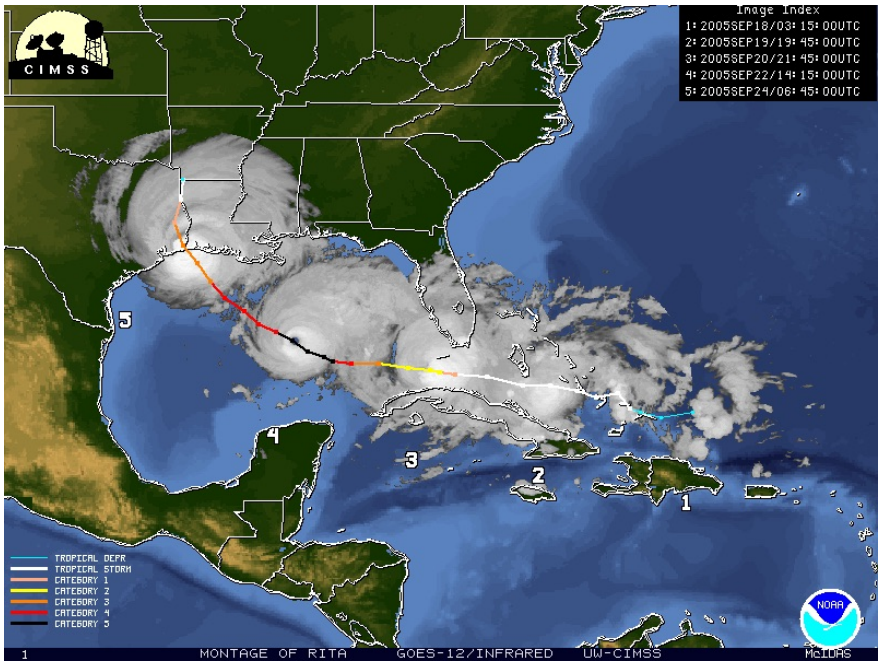

Figure 20: *Montage of GOES-12 infrared satellite imagery of Hurricane Rita and its best track. Source: Cooperative Institute for Meteorological Satellite Studies.*

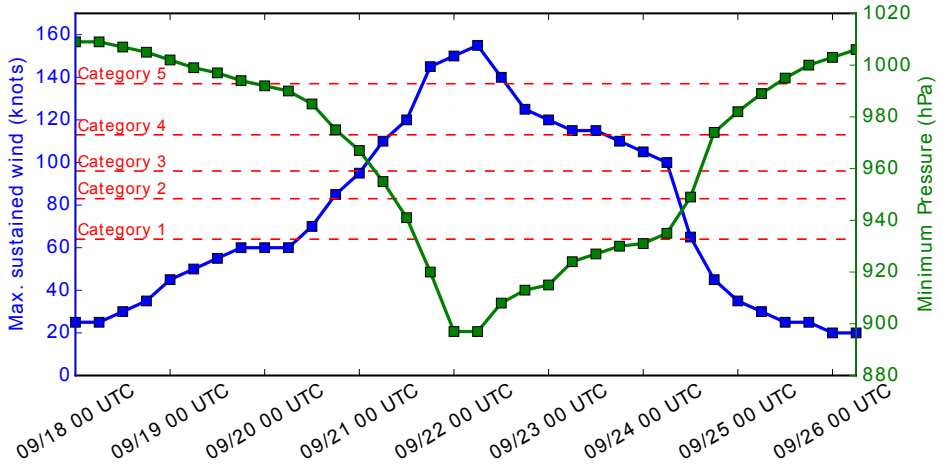

Figure 21: *National Hurricane Center best track data of Hurricane Rita's maximum sustained winds (knots, blue line) and minimum pressure (hPa, green line).*

at 0740 UTC 24 September in southwestern Louisiana as a Category 3 Hurricane with an estimated intensity of 100 knots. One of the largest evacuations in U. S. history was conducted in anticipation of Rita's landfall. The storm surge that accompanied Rita devastated entire communities in coastal areas of southwestern Louisiana, and was estimated to be as high as 15 feet. Downed trees and power lines left well over one million customers without power for days and even weeks. Seven direct fatalities were reported. The total damage of Rita is estimated at about $12 billion (NHC TC Report; Knabb et al. (2011)).

The entire lifecycle of Hurricane Rita was observed in detail by the Hurricane Rainband and Intensity Change Experiment (RAINEX; Houze et al., 2006)). Previous observational studies about Hurricane Rita mainly focussed on its structure during rapid intensification on 21 September and the eyewall replacement cycle on 22 September 2005. Didlake and Houze (2013a,b) documented the structure of the convective and stratiform sectors of the rainbands of Hurricane Rita on 21 September 2005. Bell et al. (2012b) examined the symmetric evolution of the hurricane as it underwent eyewall replacement, and Didlake and Houze (2011) analyzed the kinematics of the secondary eyewall on 22 September 2005. This dissertation focuses on the sheared structure of Hurricane Rita observed on the following day, 23 September 2005. Rita weakened from a Category-4 to a Category-3 hurricane during the mission, while being impacted by increased south-southwesterly vertical wind shear.

Table 3: *Number of radar files used per period and radar data source.*

	2040 UTC	2110 UTC	2140 UTC	2210 UTC	total
ELDORA	1374	1085	1086	1265	4810
N42	394	321	74	211	1000
N43	384	302	200	0	886
total	2152	1708	1360	1476	6696

4.2 Data

RAINEX was the first experiment to use the high-resolution radar ELDORA in tropical cyclones, and the first experiment to simultaneously use three airborne dual-Doppler radars (NRL P-3, N42, N43). The data used in this study were collected during a period of 132 minutes, from 2022 UTC to 2235 UTC. The data were split into four consecutive periods of approximately 30 minutes each, such that every period contains enough data to provide a complete view of the entire eyewall. The first period lasts from 2022 to 2100 UTC, the second period from 2100 to 2130 UTC, the third period from 2130 to 2200 UTC, and the last period from 2200 to 2235 UTC.

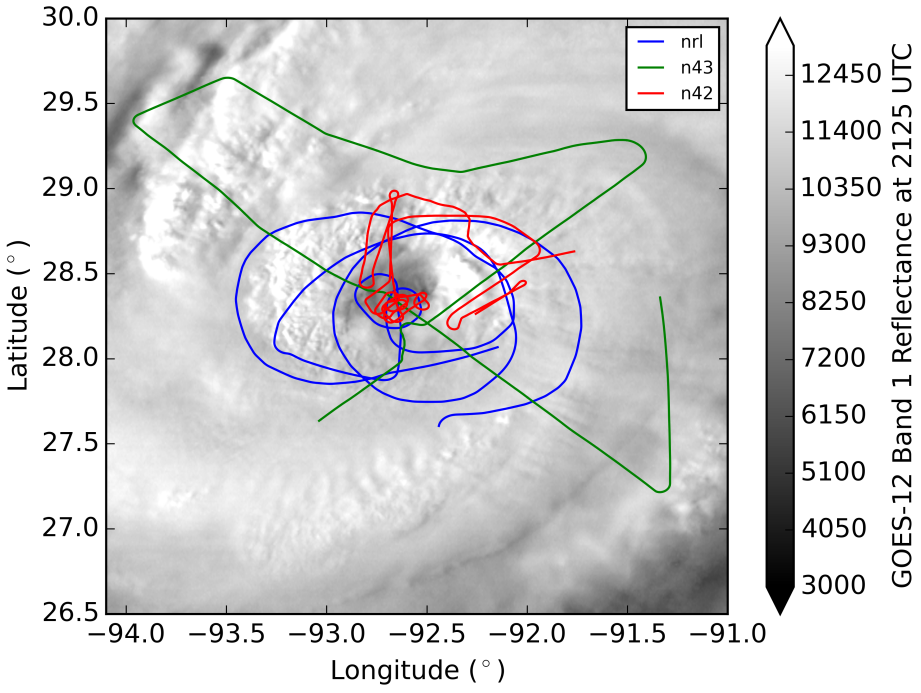

Figure 22: *Flight tracks of NRL P-3 (blue), NOAA 43 (green), and NOAA 42 (red) into Hurricane Rita during the period of interest (2020 UTC to 2230 UTC), overlaid on GOES-12 Band 1 Reflectance at 2125 UTC 23 September 2005.*

From now on, the different periods will be referred to by their respective reference times (2040 UTC, 2110 UTC, 2140 UTC, and 2210 UTC), where the storm's center position at reference time is used to define the center position of the respective analysis domain. The main data source for all four periods is airborne radar data. Three aircraft, each equipped with a tail dual-Doppler radar, sampled Rita simultaneously (Fig. 22). Figure-four flight patterns (N43) were combined with circumnavigation flight patterns (NRL P-3) and eyewall penetration flight patterns (N42) to provide complimentary data sets, providing a great combination of data ideal for synthesizing the Doppler winds into wind analyses. A total of 6696 radar sweep files was used (Table 3), complemented by dropsonde data and flight level data from the NOAA aircraft.

4.3 Radar Data Quality Control

Each radar sweep file was quality controlled before being used as SAMURAI input. First, navigation corrections were applied to correct for biases in the recorded aircraft position and orientation. The navigation corrections were estimated using a new method (Cai et al., 2015), which generalizes the previous methods of Testud et al. (1995), Georgis et al. (2000), and Bosart et al. (2002). The method uses surface echoes and near-aircraft echoes (when available) recorded during a straight and level calibration flight leg to assess the errors in the aircraft inertial navigation system. Second, an automatic editing script (Appendix A, Bell et al. (2013)) is applied to remove the majority of the bad data. This includes the removal of areas with low returns and high spectrum width, and the removal of ground clutter. Moreover, the script dealiases the Doppler velocity using a Bargen-Brown algorithm (Bargen and Brown, 1980).

An example ELDORA sweep file illustrates the value of the automated editing script (Fig. 23b). All low-return areas are removed, as well as most of the ground clutter and the second trip echos (even good data is identified as second-trip echo to the left of the aircraft[1]). Some manual editing is still necessary to remove the remaining ground clutter signatures and especially to remove side lobes (Fig. 23c). In this example, the side lobes are easy to identify, but when they occur in regions that also contain good data it can be challenging to distinguish between side-lobe echos and weather returns. Additional dealiasing was sometimes required during the manual editing step as well.

[1]In some cases the automated editing script with "low" thresholds actually removed more good data than the script with "medium" thresholds, although it was designed to be more conservative. With bad data close to the radar and good data further out, it seems that removing more data before calling the "defreckle" command might be beneficial. Otherwise the "defreckle" command acts to delete the entire ray of data.

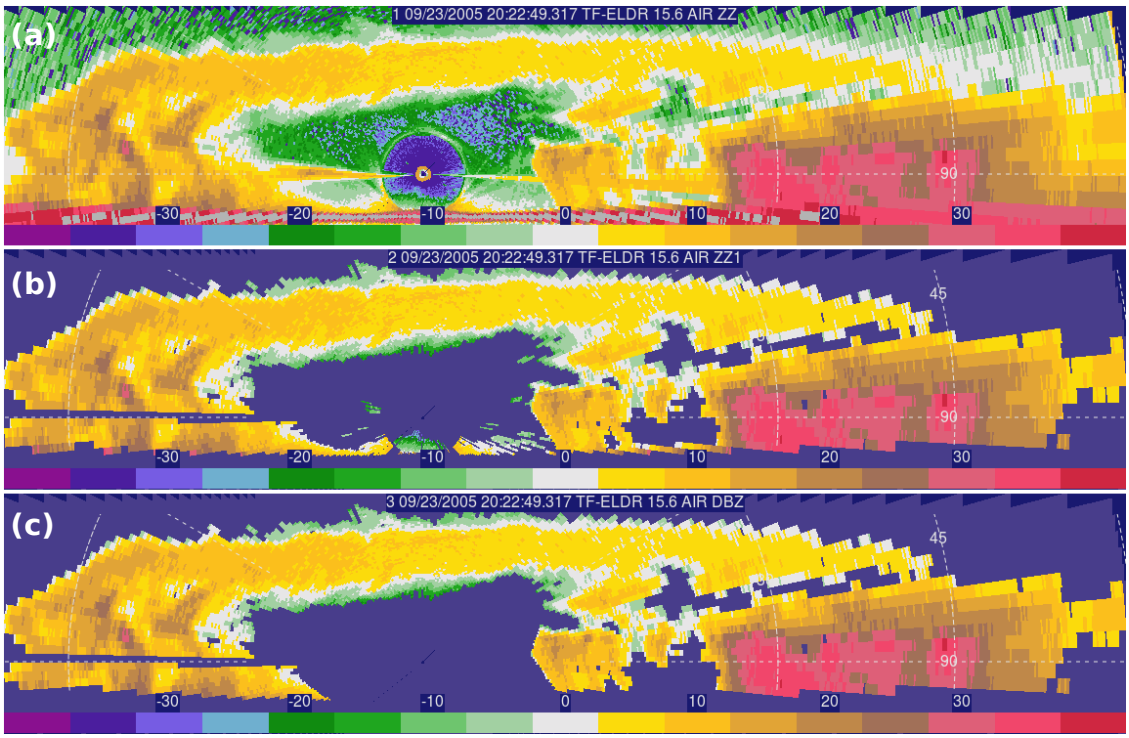

Figure 23: *Stepwise quality control process of airborne radar data as exemplified by one ELDORA sweep file: (a) raw, navigation-corrected reflectivity data, (b) application of an automatic editing script, followed by (c) manual editing.*

4.4 Retrieval

The retrieval of temperature and pressure perturbations from real data adds a couple more challenges compared to the retrieval from model output as performed in section 3. In most cases, the data coverage is not complete. Some regions within the domain will be out of the range of the radar, while other regions won't contain enough hydrometeors to return a usable signal. Moreover, the Cartesian wind components are not measured directly, they are derived from Doppler velocities from different viewing angles. Thus, the quality of the wind field depends on the scanning geometry.

As outlined in the methodology section, the first step of the method is to combine the radar data and complementary in-situ flight track, dropsonde and atmospheric-motion-vector observations into a gridded SAMURAI analysis. A domain size of 120 km x 120 km x 15 km is used, with a horizontal resolution of 1 km and a vertical resolution of 0.5 km. The SAMURAI analysis is performed in two iterations, using higher filters in the first iteration and lower filters in the second iteration to get a smooth analysis. A hybrid variational setting was used (see Appendix in Foerster et al. (2014)), limiting the elevation angle to 45° and neglecting

the projection of the vertical wind in the Doppler velocity. More details of the SAMURAI configuration can be found in Appendix B.

The second step of the method is to calculate the reference state for the pressure and temperature retrieval from the azimuthally-averaged wind field and from a vertical temperature and pressure profile at the edge of the domain. The center of the storm is determined by finding the maximum mean vorticity, similar to the method of Marks et al. (1992). The mean center of the storm is defined as the average of the centers between 2 km and 8 km altitude. The temperature and pressure profiles used to anchor the balanced vortex calculation are derived from the azimuthally-averaged SAMURAI temperature and pressure field at a radius of 60 km. The inward integration of the thermal wind equation (Smith, 2006) then allows to determine the mean temperature and pressure field that balances the mean tangential wind field.

The gaps in data coverage are either small enough or located favorably to not significantly affect the reference state calculation. The coverage out to 60 km radius is good enough to calculate an average tangential wind speed, although a slight bias might be introduced because the data gaps are located predominantly towards the south. The data gap in the eye of Hurricane Rita at levels above 4 km implicates that no reference pressure and temperature can be calculated in that area. Fortunately, the thermal wind equation is integrated inwards and not outwards, hence the data gap in the eye does not affect other regions. In contrast, a data gap at larger radii would preclude the computation of the mean temperature and pressure everywhere inward of that radius. The third and final step of the method is the retrieval of the pressure and temperature perturbations as described in chapter 2.3. Details of the retrieval configuration can be found in Appendix C.

4.5 Results

The kinematic and thermodynamic structure of Hurricane Rita will be investigated with respect to its variability over time, its response to vertical wind shear, and the characteristics of the eyewall convection.

4.5.1 Storm Structure and Evolution

Horizontal cross sections of radar reflectivity, horizontal wind field and vertical motion at 2 km (Fig. 24), 5 km (Fig. 25), and 8 km (Fig. 26) show that the main features of the storm structure are generally consistent across all four times, but that details vary from

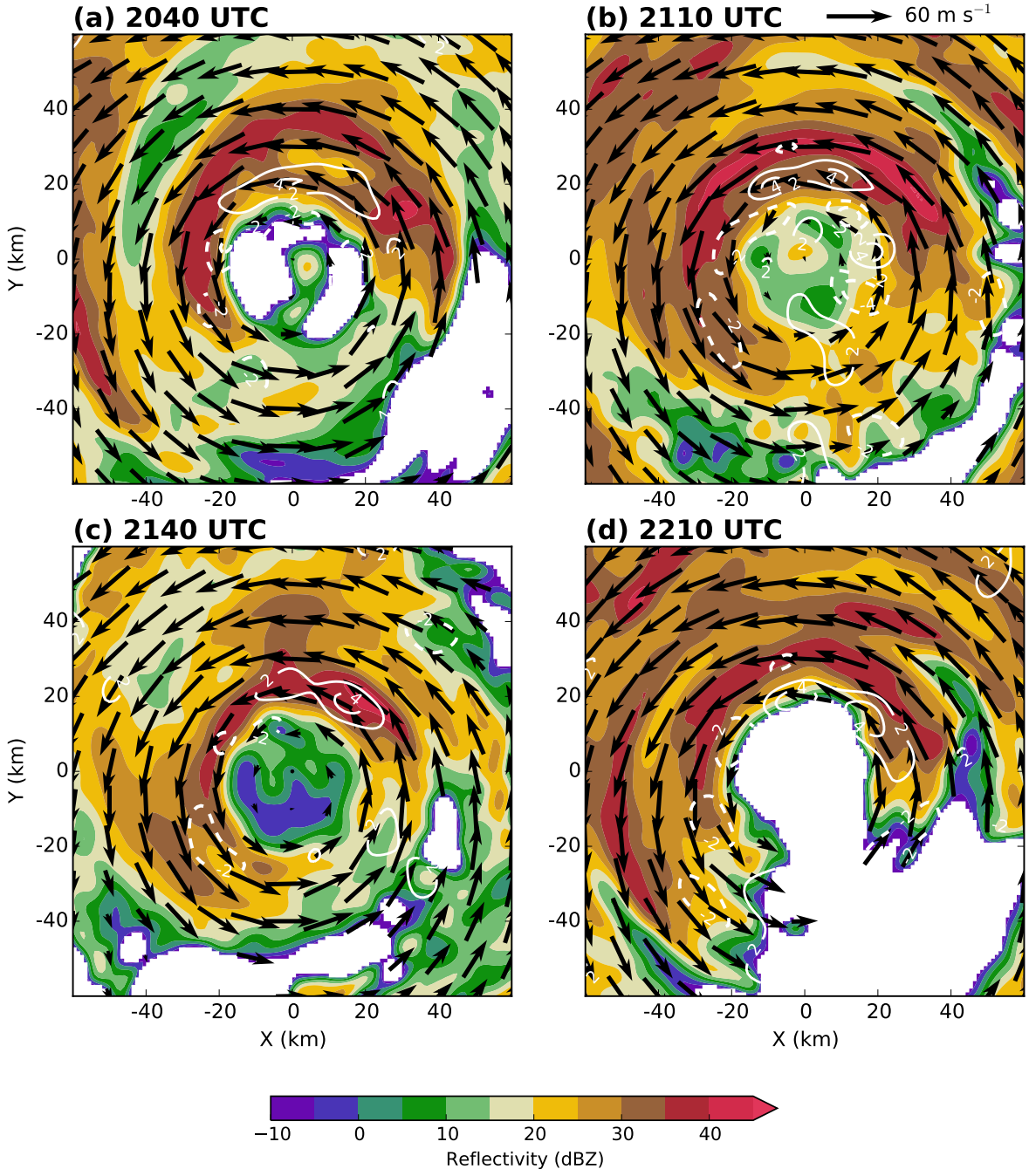

Figure 24: *Horizontal cross sections of SAMURAI radar reflectivity (shaded, dBZ), horizontal velocity (black arrows, m s^{-1}), and vertical velocity (white contours, m s^{-1}) at 2 km altitude for (a) 2040 UTC, (b) 2110 UTC, (c) 2140 UTC, and (d) 2210 UTC.*

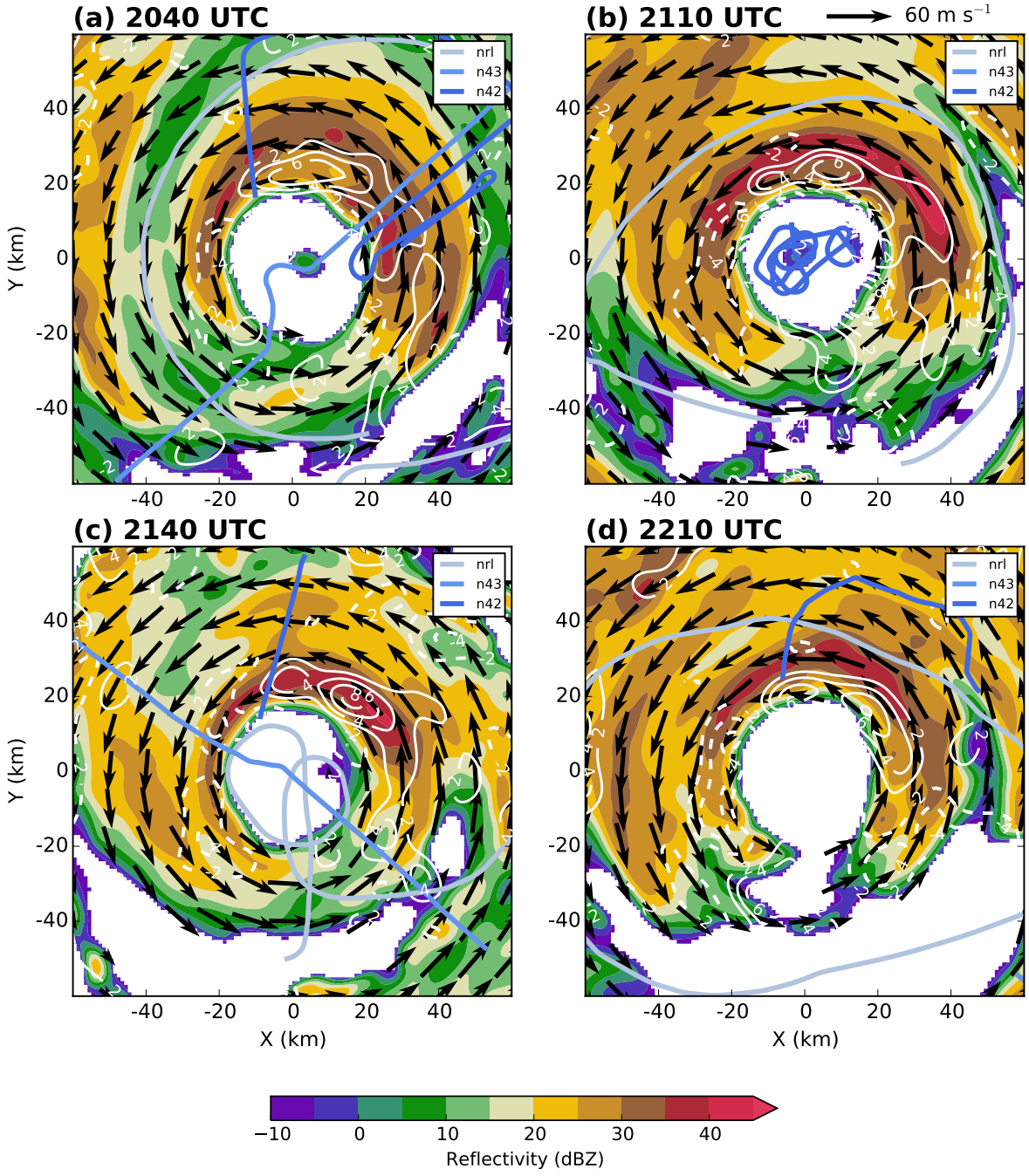

Figure 25: *Horizontal cross sections of SAMURAI radar reflectivity (shaded, dBZ), horizontal velocity (black arrows, m s^{-1}), and vertical velocity (white contours, m s^{-1}) at 5 km altitude for (a) 2040 UTC, (b) 2110 UTC, (c) 2140 UTC, and (d) 2210 UTC. Flight tracks of NRL P-3, NOAA 42, and NOAA 43 are overlaid.*

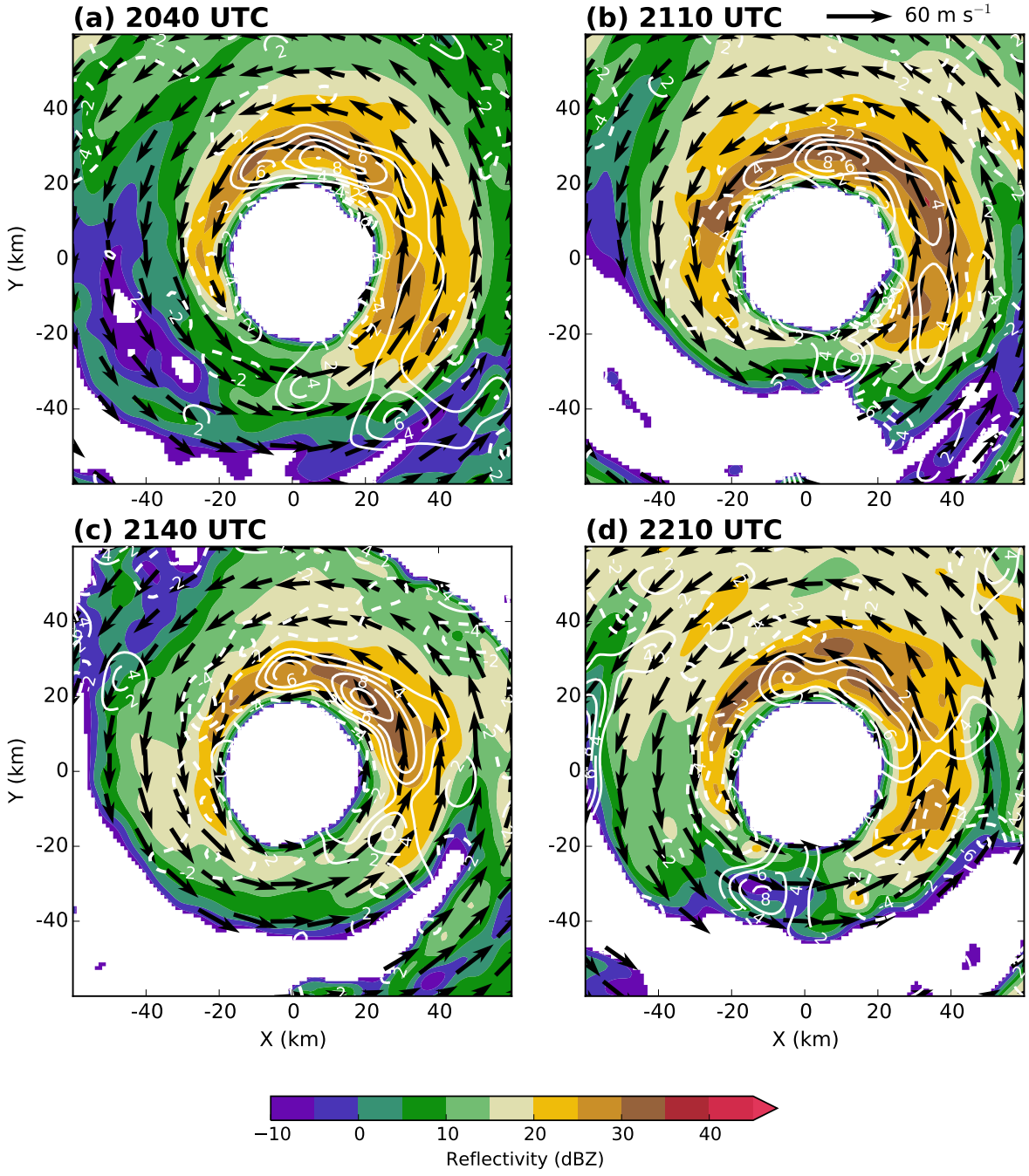

Figure 26: *Horizontal cross sections of SAMURAI radar reflectivity (shaded, dBZ), horizontal velocity (black arrows, m s^{-1}), and vertical velocity (white contours, m s^{-1}) at 8 km altitude for (a) 2040 UTC, (b) 2110 UTC, (c) 2140 UTC, and (d) 2210 UTC.*

Table 4: *Statistics of the center position of Hurricane Rita and its vertical tilt derived from SAMURAI analyses on 23 September 2005. Center positions for the four periods are in degrees latitude and longitude. The tilt it calculated between 8 km and 2 km altitude, and the tilt direction is defined using the meteorological convention.*

time	center lat (°)	center lon (°)	tilt magnitude (km)	tilt direction (°)
2040 UTC	-92.56	28.23	5.0	53
2110 UTC	-92.63	28.30	5.0	37
2140 UTC	-92.68	28.38	2.2	63
2210 UTC	-92.74	28.45	4.2	45

time to time. The data coverage for all times is very good in the northern semicircle. Some gaps in coverage exist towards the southern edge of the domain and in the eye, which is in part due to the flight patterns and in part due to a lack of hydrometeors. The eyewall is located at a radius of around 25 km. All times show a clear shear signature, with the highest radar reflectivities at all vertical levels in the northern semicircle, which roughly coincides with the left-of-shear semicircle (as will be shown later). The highest vertical velocities are consistently in the eastern and northern part of the eyewall, whereas the western part shows predominantly downward motion. The highest maximum reflectivities occur at 2110 UTC, where two regions exceed 40 dBZ at 5 km altitude. The vertical velocities in the northern part of the eyewall at 5 km are collocated with the highest reflectivity values for 2140 UTC, and located radially inward of the highest reflectivity values for the other three times. As observed in several previous studies, new cells usually form in the southeastern (downshear-right) part of the eyewall, mature as they rotate into the northern (downshear-left) part, and dissipate in the western (upshear-left) part of the eyewall.

The SAMURAI analyses can be used to estimate storm motion and vertical tilt of the storm. The tilt is defined as the difference between the center positions at 8 km and 2 km. The vortex center positions show the linear, northwesterly track of Hurricane Rita during the observation period (Fig. 28, Table 4). Rita moved at a speed of 5.3 m s^{-1} and with a heading of 321°. The tilt magnitude changes slightly from period to period, but the shear direction was always oriented toward the northeast (Fig. 27). At 2040 UTC the tilt rotates anticyclonically with height, at 2210 UTC the tilt changes more or less linearly with height, and at 2110 and 2140 UTC the tilt patterns are more complex. The direction of the vertical wind shear is defined using estimates from the SHIPS database (Statistical Hurricane Intensity Prediction Scheme; DeMaria and Kaplan (1994)). The shear values are averages between the SHIPS data for 1800 UTC 23 September and for 0000 UTC 24 September. The deep-layer shear (200-850 hPa) is 12.3 m s^{-1} in north-northeasterly direction (21.5°), and the shallow-layer

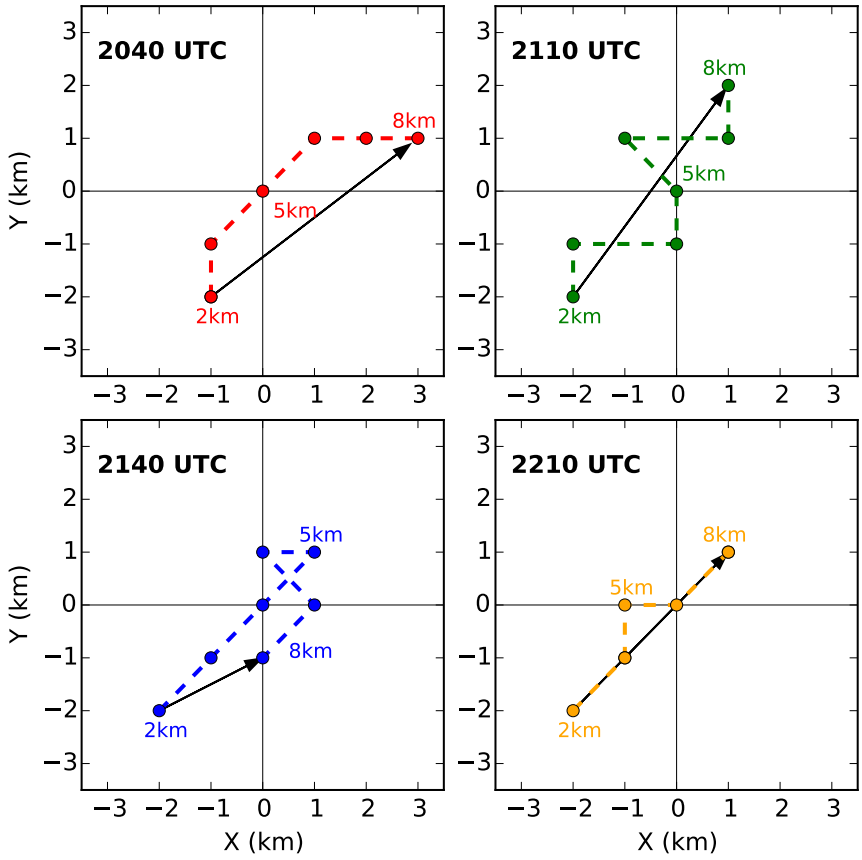

Figure 27: *Center position with respect to the average storm center (see Table 4) for each vertical level between 2 km and 8 km altitude in increments of 1 km for the four periods: 2040 UTC, 2110 UTC, 2140 UTC, and 2210 UTC. The tilt vector is added for each period.*

shear (500-850 hPa) is 1.5 m s^{-1} in northeasterly direction (56°). Hence, the tilt direction for all four periods is located downshear or even slightly downshear-right.

The center positions are used as point of origins to transform the SAMURAI analyses from Cartesian to cylindrical coordinates. This enables the computation of the azimuthally-averaged storm structure (Fig. 29). All four times show maximum mean tangential wind speeds in excess of 50 m s^{-1} at low levels at a radius of about 30 km. 2110 UTC shows the highest overall mean radar reflectivities. At 2110 UTC, the highest mean radar reflectivities are collocated with the highest tangential wind speeds, as is the case at 2210 UTC. In contrast, 2040 UTC and 2140 UTC show two reflectivity maxima, one being located radially inside of the tangential wind maximum (around 25 km radius), and one being located radially outside (around 35 km radius). 2210 UTC also has an additional radar maximum at large radii (around 55 km).

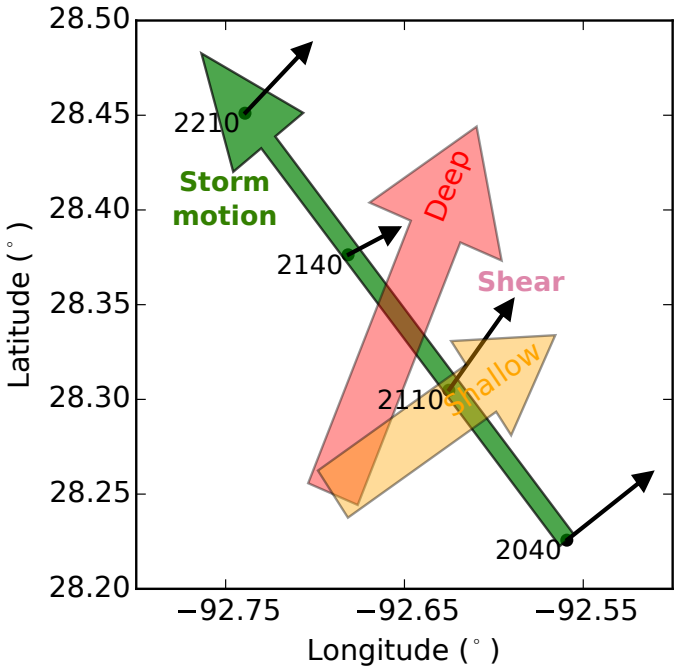

Figure 28: *Schematic of storm center positions, tilt directions, storm motion and environmental shear for all four periods. The center positions (black circles) and the tilt (small black arrows) are derived from center positions between 2 and 8 km of the respective SAMURAI analyses (see text). The storm motion is illustrated by the large green arrow. The red arrow indicates the SHIPS deep-layer shear direction, and the orange arrow indicates the SHIPS shallow-layer shear direction.*

Fig. 30 shows the mean temperature increase ($\bar{T}$(r,z) - $\bar{T}$(r = 60 km, z)) and pressure drop ($\bar{p}$(r,z) - $\bar{p}$(r = 60 km, z)) from the edge of the domain toward the center of the storm, which were calculated using the mean tangential wind fields displayed in Fig. 29. The pressure drop is most pronounced at lower levels, with a maximum pressure drop of Δp $>$ 26 hPa in all cases. The temperature increase with decreasing radius is smallest at 4 km altitude, and increases above. 2040 UTC and 2210 UTC show a maximum in the temperature increase at 6 to 9 km altitude, whereas the increase is more linear with height for 2110 UTC.

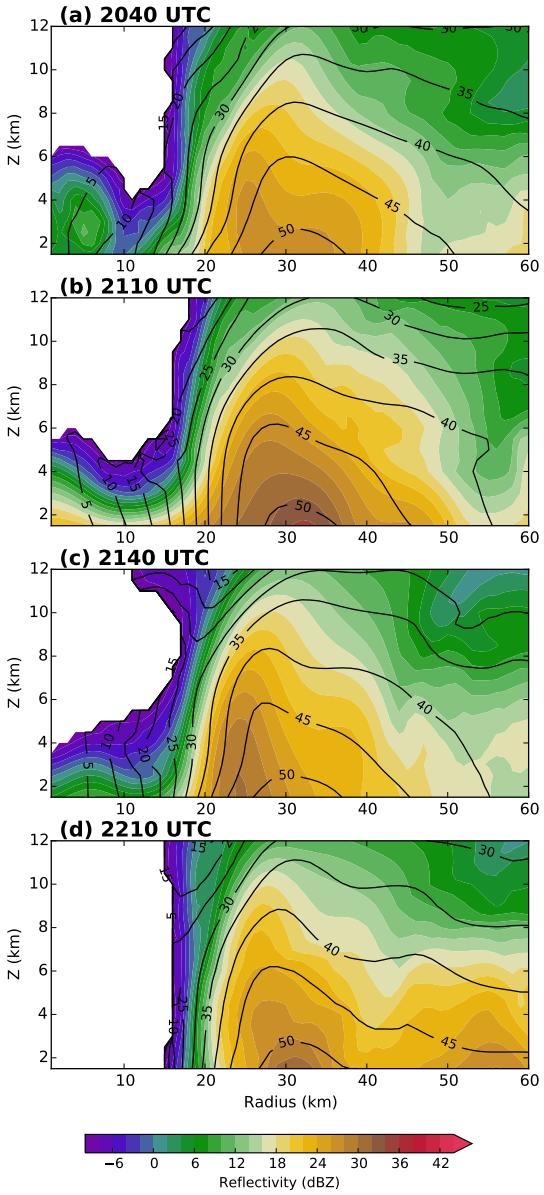

Figure 29: *Azimuthally-averaged storm structure of radar reflectivity (shaded, dBZ) and tangential wind speed (m s^{-1}) for (a) 2040 UTC, (b) 2110 UTC, (c) 2140 UTC, and (d) 2210 UTC.*

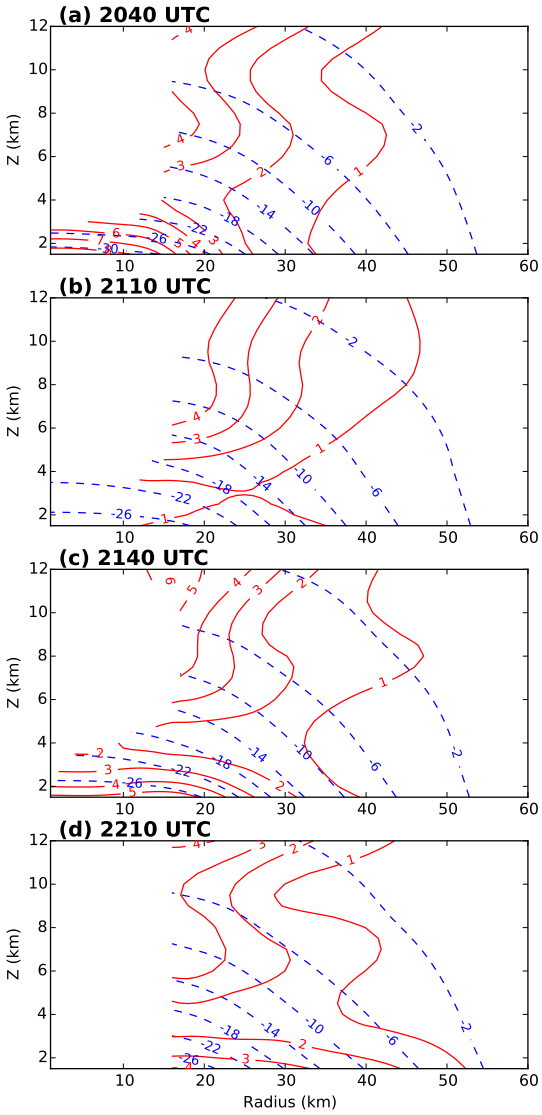

Figure 30: *Mean pressure deficit (blue dashed, hPa) and mean temperature increase (red solid, K) relative to the mean pressure and temperature at a radius of 60 km at each respective vertical level for (a) 2040 UTC, (b) 2110 UTC, (c) 2140 UTC, and (d) 2210 UTC.*

4.5.2 Thermodynamic Structure

The retrieved pressure and temperature fields (Figs. 31, 32) show a lot of structure, with the temperature field being more noisy than the pressure field, which is consistent with the results of the retrieval evaluation. Both variables show a strong wavenumber-1 pattern for most times and vertical levels, reflecting the impact of vertical wind shear on the structure of Hurricane Rita. Vertical wind shear is known to induce wavenumber-1 patterns in many quantities, and the kinematic storm structure in the last section hinted at the existence of wavenumber-1 patterns in the radar reflectivity and vertical motion fields.

The kinematic and thermodynamic variables are decomposed into azimuthal wavenumbers in order to investigate the effects of shear separately from other effects. The SAMURAI analyses in cylindrical coordinates are used to compute a discrete one-dimensional Fourier transform for each range ring, for a radial spacing of 1-km and an azimuthal spacing of 1°. In case of missing data along a range ring the data were interpolated across the gap using cubic one-dimensional splines.

4.5.3 Impact of Shear: Wavenumber-1

Previous observational and modeling studies have found wavenumber-1 patterns in various different kinematic and thermodynamic properties which were due to shear. In general, the upward motion is found to be located in the downshear quadrants, the radar reflectivity is maximized in the left-of-shear quadrants, and the vorticity anomalies downshear are positive at small radii and negative at large radii. The three-dimensional thermodynamic structure has been investigated using numerical modeling studies (e.g. Jones, 2000), but previous observational studies like Reasor and Eastin (2012) had sampling limitations that precluded full assessment of the three-dimensional thermodynamic structure. Our dataset allows to expand on these previous studies. In contrast to the Reasor and Eastin (2012) study we can examine the thermodynamic structure at all vertical levels, not just at flight level. The four consecutive periods enable us to examine the consistency of the wavenumber-1 patterns and to identify possible evolutions.

The horizontal cross sections of radar reflectivity and vertical velocity (Figs. 24, 25, and 26) showed that the vertical velocity has a strong wavenumber-1 component, with the strongest upward motion in the eastern and northern quadrants of the eyewall for all four periods. Location and strength of the updrafts varied only slightly from period to period. The wavenumber-1 vertical velocity asymmetries confirm this pattern (Fig. 33). The

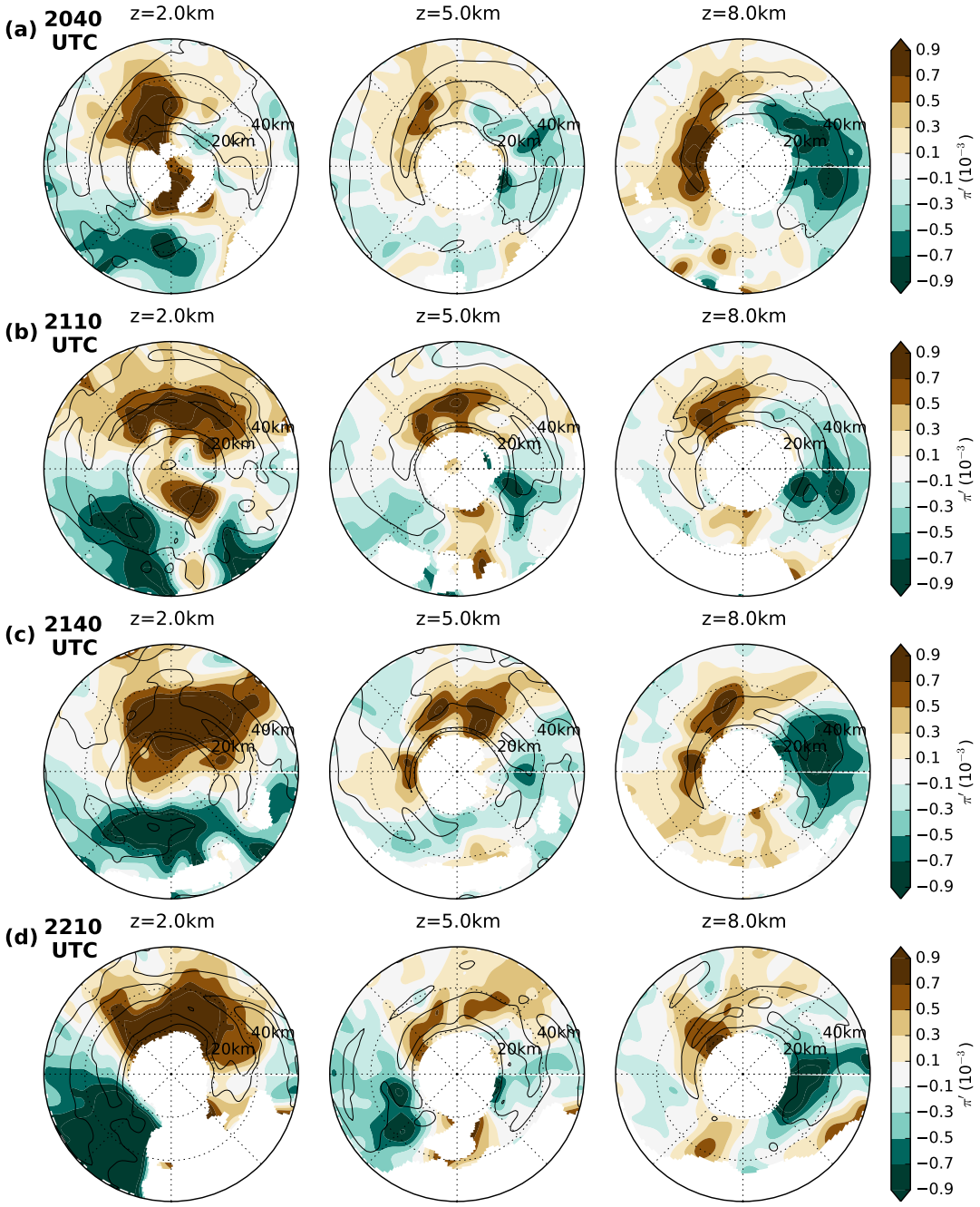

Figure 31: *Horizontal cross sections of perturbation pressure (shaded, 10^{-3}) for 2 km (left), 5 km (center), and 8 km altitude (right) for 2040 UTC, 2110 UTC, 2140 UTC, and 2210 UTC. Radar reflectivity (black contours at 20, 30, 40, and 50 dBZ) is added for orientation.*

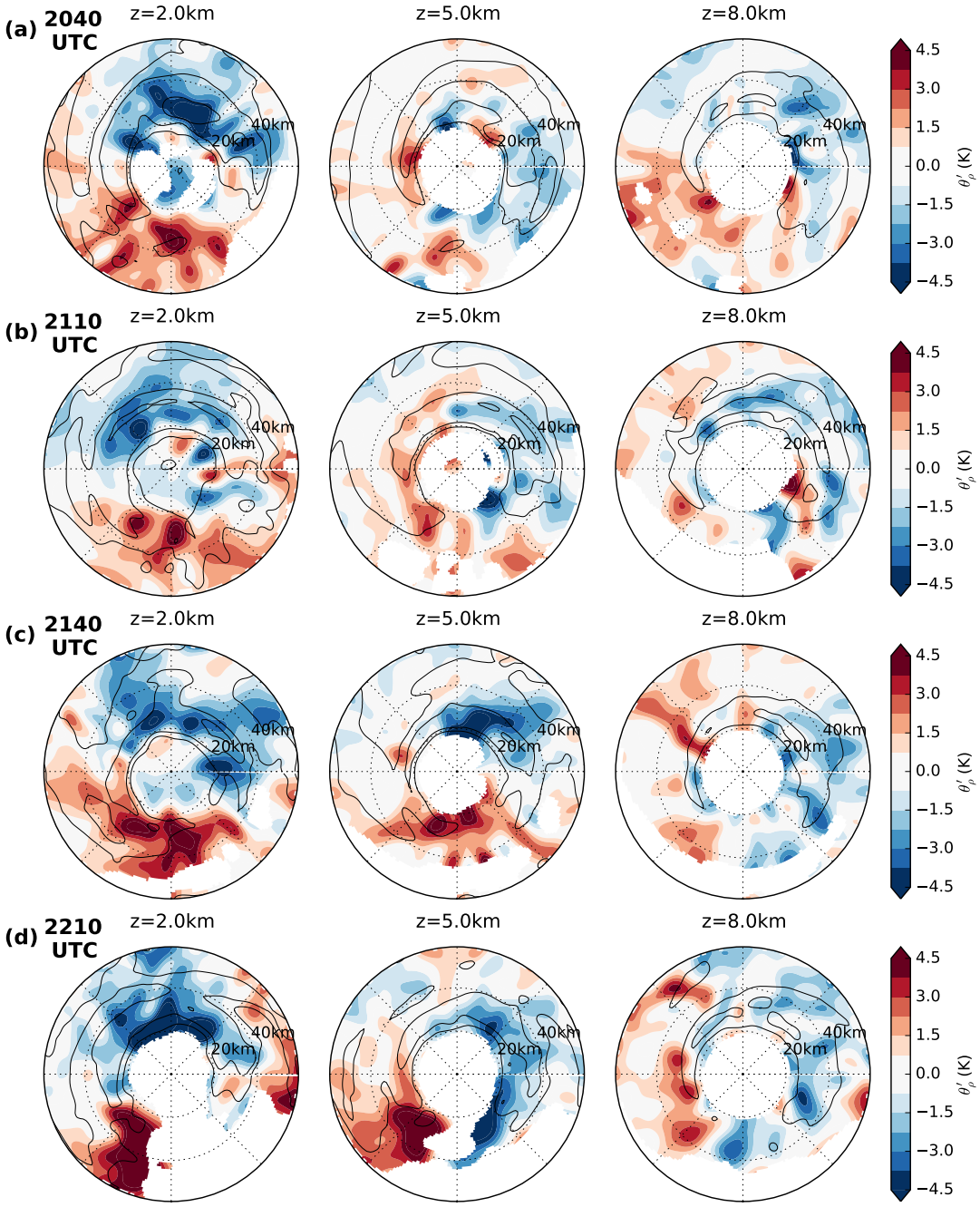

Figure 32: *Horizontal cross sections of perturbation density potential temperature (shaded, K) for 2 km (left), 5 km (center), and 8 km altitude (right) for 2040 UTC, 2110 UTC, 2140 UTC, and 2210 UTC. Radar reflectivity (black contours at 20, 30, 40, and 50 dBZ) is added for orientation.*

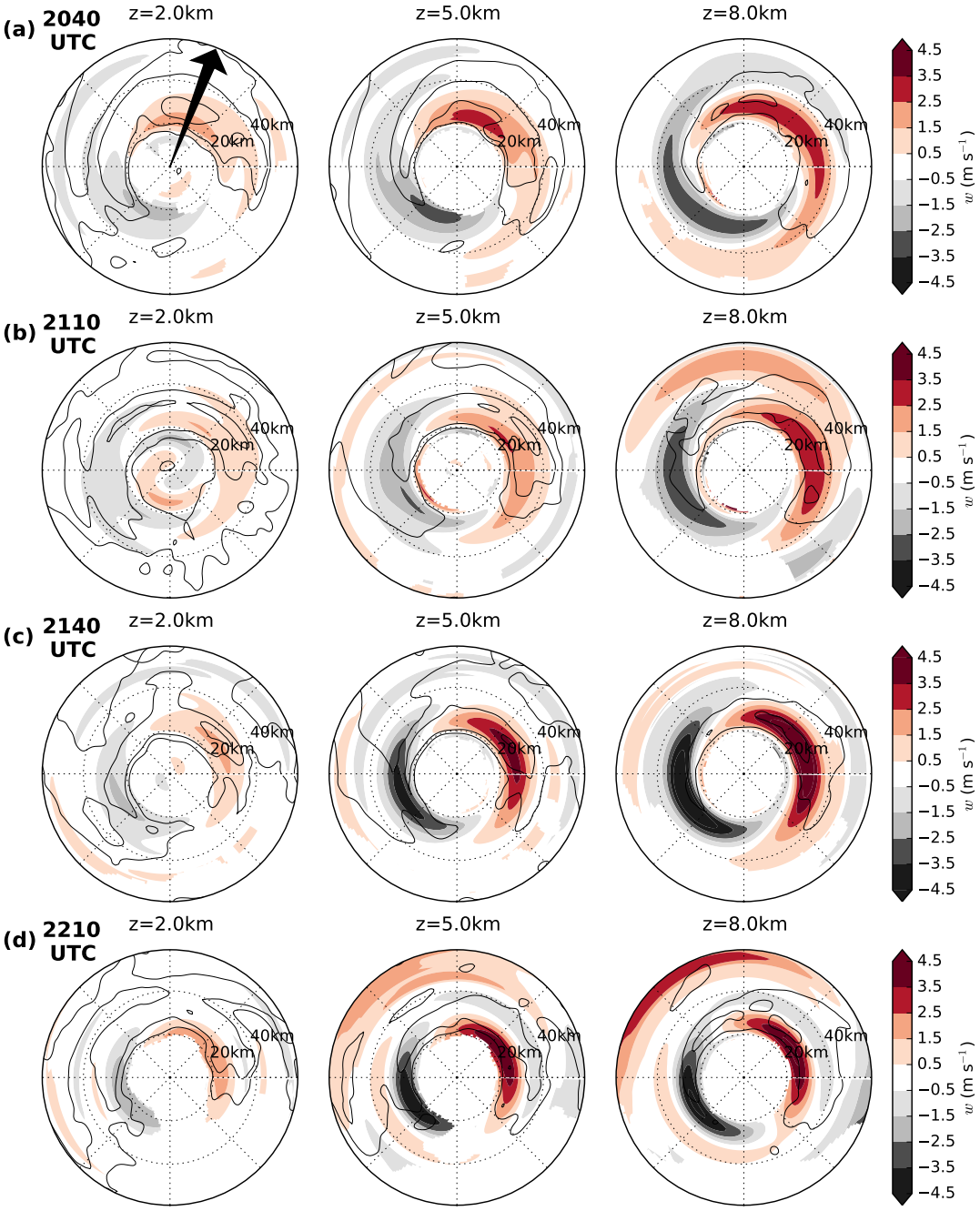

Figure 33: *Horizontal cross sections of the wavenumber-1 component of vertical velocity (shaded, m s^{-1}) for 2 km (left), 5 km (center), and 8 km altitude (right) for 2040 UTC, 2110 UTC, 2140 UTC, and 2210 UTC. The black arrow in the top left panel illustrates the shear direction. Radar reflectivity (black contours at 20, 30, 40, and 50 dBZ) is added for orientation.*

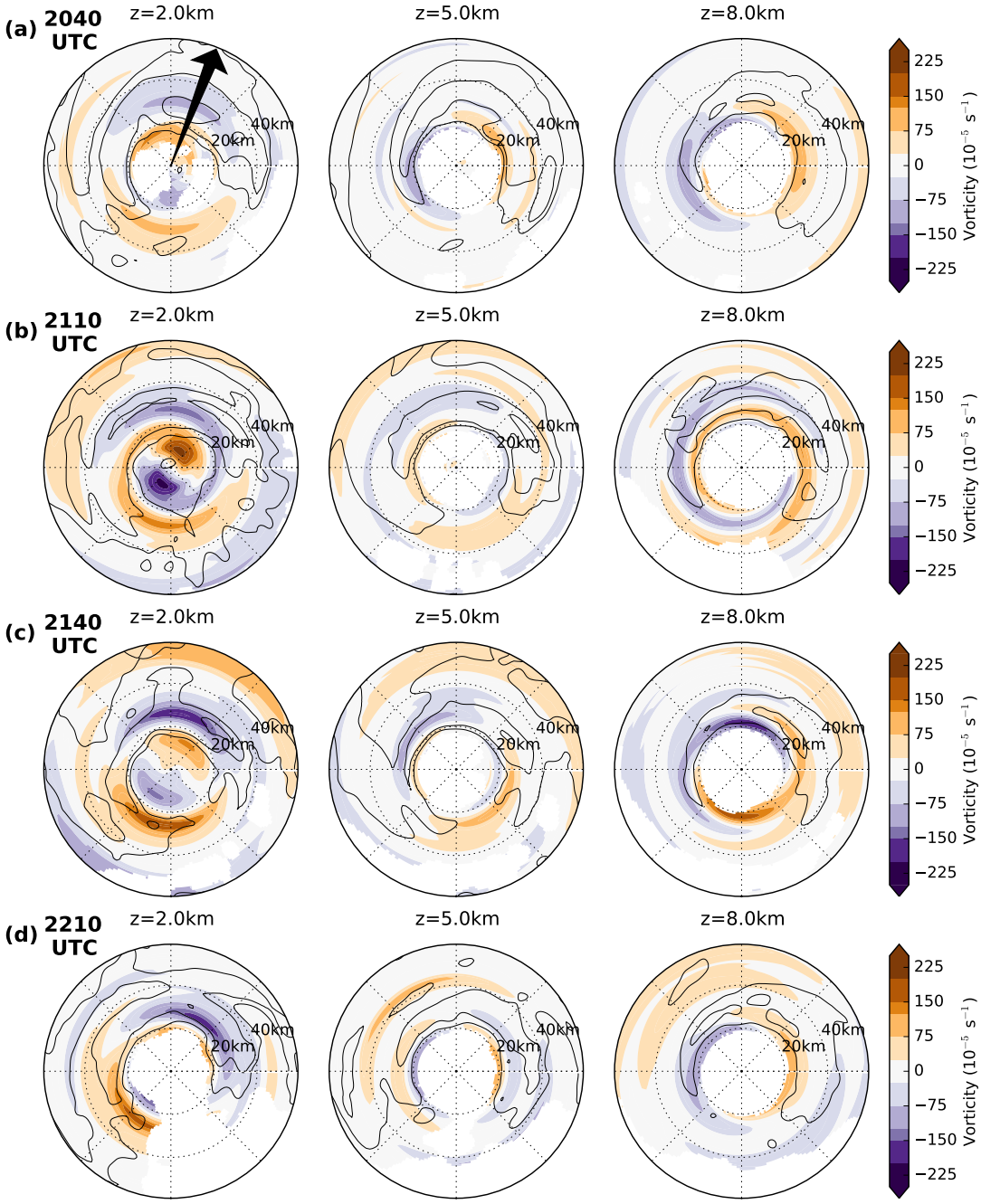

Figure 34: *Horizontal cross sections of the wavenumber-1 component of vertical vorticity (shaded, 10^{-5} s^{-1}) for 2 km (left), 5 km (center), and 8 km altitude (right) for 2040 UTC, 2110 UTC, 2140 UTC, and 2210 UTC. The black arrow in the top left panel illustrates the shear direction. Radar reflectivity (black contours at 20, 30, 40, and 50 dBZ) is added for orientation.*

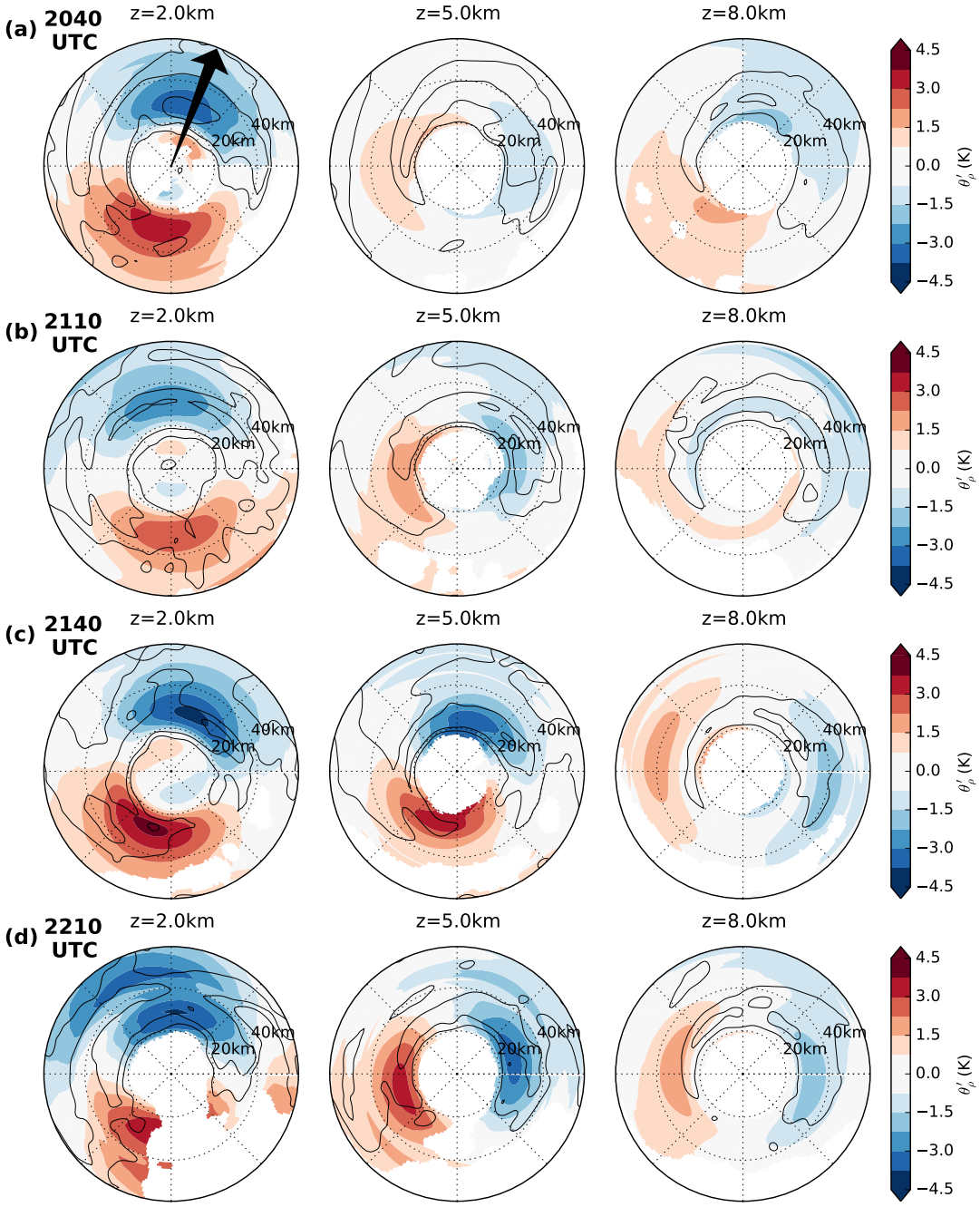

Figure 35: *Horizontal cross sections of the wavenumber-1 component of perturbation density potential temperature (shaded, K) for 2 km (left), 5 km (center), and 8 km altitude (right) for 2040 UTC, 2110 UTC, 2140 UTC, and 2210 UTC. The black arrow in the top left panel illustrates the shear direction. Radar reflectivity (black contours at 20, 30, 40, and 50 dBZ) is added for orientation.*

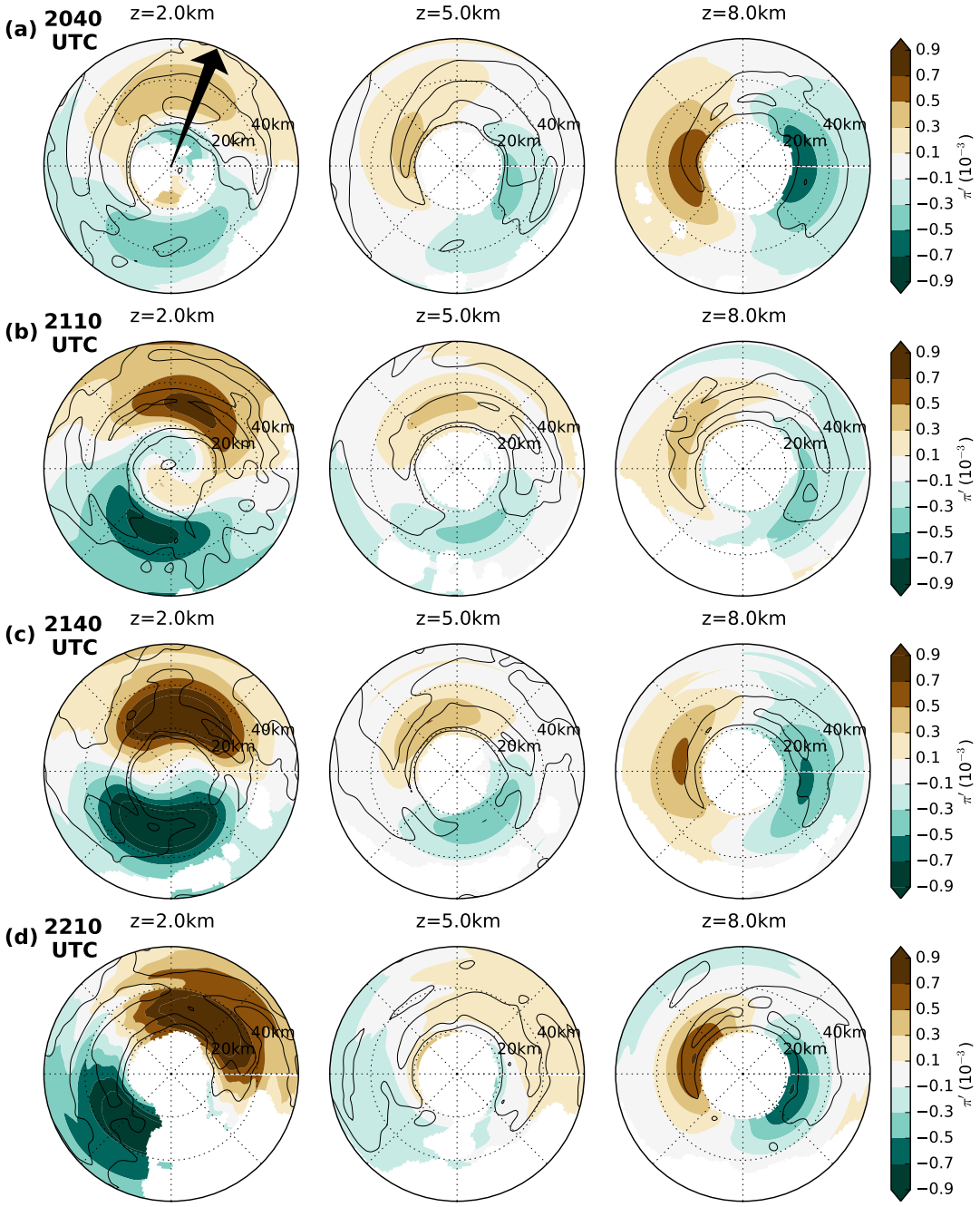

Figure 36: *Horizontal cross sections of the wavenumber-1 component of perturbation pressure (shaded, 10^{-3}) for 2 km (left), 5 km (center), and 8 km altitude (right) for 2040 UTC, 2110 UTC, 2140 UTC, and 2210 UTC. The black arrow in the top left panel illustrates the shear direction. Radar reflectivity (black contours at 20, 30, 40, and 50 dBZ) is added for orientation.*

wavenumber-1 vertical velocity maximum is located in the northeastern eyewall between 20 and 35 km for all vertical levels and periods. The vertical velocity magnitude increases with height. Small variations occur on top of this very consistent pattern. The vertical velocity is stronger in the latter two periods. During the first period, 2040 UTC, the maximum is rotated slightly anti-clockwise compared to the other periods, with the maximum more toward the north than the east. During the last period, 2210 UTC, the maximum is located farther radially inward than during the other periods, located at the inner edge of the 20 dBZ contour. No significant rotation of the vertical velocity with height is evident.

The wavenumber-1 vorticity asymmetries at 2 km for all four periods (Fig. 34) look very similar to the wavenumber-1 vorticity asymmetries in Hurricane Guillermo at 2 km (Reasor and Eastin, 2012), with positive anomalies inside the RMW cyclonically downstream of the regions of highest vertical velocities, and an oppositely oriented dipole outside. The vorticity patterns at upper levels are more diverse. At 2040 UTC, the wavenumber-1 asymmetries at 5 km and 8 km look very similar, with anomalies confined to the inner 30 km, at the inner edge of the eyewall, and positive values located in the convectively active regions toward the east and northeast. This pattern might be attributed to vortex stretching in active convection. The patterns during the other periods vary much more, both with height and radius.

As mentioned above, a novel aspect of this study is the unprecedented look at the thermodynamic fields of the entire vortex. The wavenumber-1 asymmetries of density potential temperature perturbations θ'_ρ show a very consistent picture over time. All periods show an anticyclonic rotation with height and little dependance of the dipole's azimuthal location with radius. Radially, the anomalies are centered around approximately 30 km. The shift in azimuthal location at larger radii at 2 km height during the last period, 2210 UTC, is most likely an effect of the large fraction of missing data in the southeastern quadrant. The cold anomalies at 2 km are located in the northern and northeastern part of the eyewall. At 5 km, the cold anomalies are rotated toward the east for periods 2040 UTC, 2110 UTC, and 2110 UTC. Only 2140 UTC shows little anticyclonic rotation with height between 2 and 5 km. At 8 km, the cold anomaly for all periods in located toward the northeast or east, meaning that it rotates little between 5 and 8 km for 2040 UTC, 2110 UTC, and 2110 UTC, whereas it rotates anti-cyclonically by almost 90° for 2140 UTC. The magnitude of the anomalies decreases with height.

The wavenumber-1 asymmetries of normalized pressure perturbations π' also show a very consistent picture over time. Radially, the anomalies are centered around approximately 30

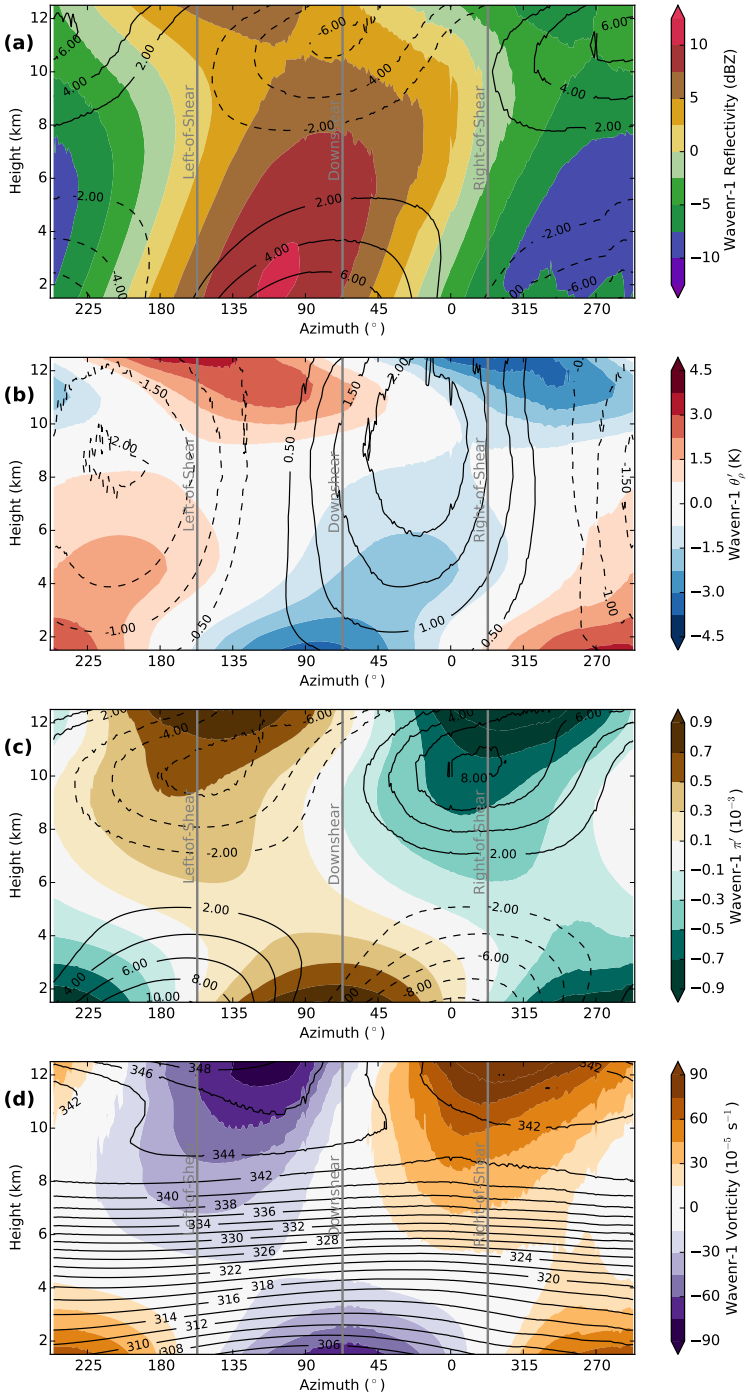

Figure 37: *Azimuth-height composites of the wavenumber-1 components of the eyewall region (20 km $\leq r \leq$ 40 km) of all four periods combined: (a) Radar reflectivity (shaded, dBZ) and tangential velocity (contoured, m s^{-1}), (b) density potential temperature perturbation (shaded, K) and vertical velocity (contoured, m s^{-1}), (c) pertubation pressure (shaded, 10^{-3}) and radial velocity(contoured, m s^{-1}), and (d) vorticity (shaded, 10^{-5} s^{-1}) and isentropes $\bar{\theta}_\rho + \theta'_{\rho 1}$ (contoured, K).*

km. In contrast to the temperature perturbations, however, the pressure perturbations rotate cyclonically with height. At 2 km, the positive pressure perturbations are located in the northern and northeastern part of the eyewall. At 5 km, the positive pressure perturbations are located in the western and northwestern part of the eyewall, with the exception of the last period, which stays at roughly the same location as at the 2 km level. The 8 km level shows a very consistent pattern for all periods again, with the positive pressure perturbations to the west and northwest. The pressure perturbations are weakest at midlevels.

The different patterns of azimuthal rotation with height can be seen more clearly in azimuth-height composites of the wavenumber-1 components (Fig. 37). Data of the eyewall region (20 km $\leq$ r $\leq$ 40 km) of all four periods are used to create these composites. The azimuthal distribution of radar reflectivity shows the highest radar reflectivities in the downshear-left quadrant, and an anti-cyclonic rotation with height. The azimuthal distribution of temperature perturbations also shows an anti-cyclonic rotation with height, whereas the pressure perturbations show a cyclonic rotation with height. The vertical velocity is the only variable that shows an upright wavenumber-1 pattern, with strongest upward motion in the downshear-right quadrant. Tangential and radial velocities show patterns with opposite orientation for levels below and above 6 km altitude. The isentropes ($\bar{\theta}_\rho + \theta'_{\rho 1}$) illustrate the adiabatic lifting in the right-of-shear quadrants, and the adiabatic subsidence in the left-of-shear quadrants.

The consistency over time of all wavenumber-1 anomalies suggests that the thermodynamic response to vertical wind shear is quite robust. A common approach to examine the vortex structure with respect to shear is to split the data into shear-relative quadrants (e.g. Hence and Houze, 2011, DeHart et al., 2014, Foerster et al., 2014). The shear direction is 21.5°. Hence, east roughly corresponds to "downshear right" (Fig. 38), which is commonly regarded as the convective-initiation quadrant. North roughly corresponds to "downshear left", the quadrant with the highest radar reflectivities due to mature convection. West roughly corresponds to "upshear left", the quadrant containing dissipating cells. And south roughly corresponds to "upshear right", the quadrant with the shallowest convection. The average behavior of the vortex within each quadrant and over time is assessed by calculating spatio-temporal averages. First, the dataset for each period is split up into quadrants, then the datasets of all four periods are combined quadrantwise. Vertical cross sections representing the mean structure of each quadrant over time are calculated by averaging the data within each quadrant and over all four periods.

The spatio-temporal averages of radar reflectivity and tangential velocity illustrate the vari-

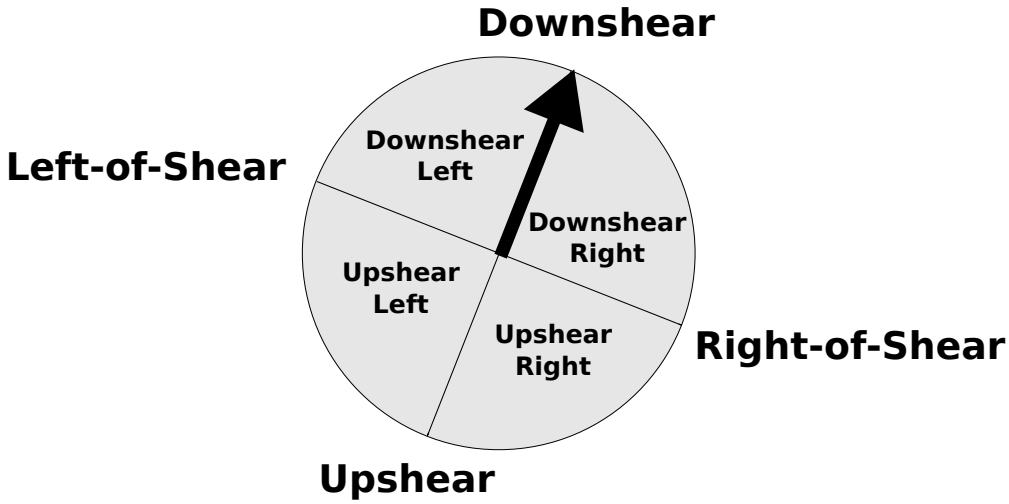

Figure 38: *Definition of shear-relative quadrants with respect to the shear direction of 21.5°, illustrated by the black arrow.*

ability from quadrant to quadrant (Fig. 39). The radar reflectivity exhibits the typical pattern of convective initiation, maturation and dissipation. The downshear-right quadrant contains deep, new convection. The 20-dBZ surface reaches up to almost 10 km and the reflectivity values at midlevels are higher than at the ground, which indicates that the convection is still in its initial stage. The downshear-left quadrant contains the most intense convection, with radar reflectivities exceeding 35 dBZ just outside of 30 km radius, and a very broad region of high reflectivity values. The 20-dBZ surfaces reaches up to 11 km at 35 km, and reaches all the way out to 55 km radius. The upshear-left quadrant contains deep convection, but it is not as intense or as wide-spread as in the previous quadrant. The highest reflectivities are inside of 30 km radius. The upshear-right quadrant contains by far the shallowest convection. The 20-dBZ surface barely reaches 1.5 km.

The tangential velocity largely follows the reflectivity pattern. In the downshear-right quadrant no clear RMW is discernible above 6 km. The 45 m s^{-1} isotach has a similar shape to the 20-dBZ surface, with a flat top and an almost rectangular shape. The isotaches inside of 20 km radius are almost upright. In the downshear-left quadrant the RMW slopes outward with height, going from about 26 km radius at 1 km altitude out to about 32 km at 12 km. The isotaches at the inner edge of the eyewall exhibit the largest slope of all quadrants, whereas the isotachs fall off slowly outside the RMW. In the upshear-left quadrant the RMW is pronounced, and located radially outside of the reflectivity maximum. In the upshear-right quadrant the vertical gradient in tangential velocity is very weak. The RMW,

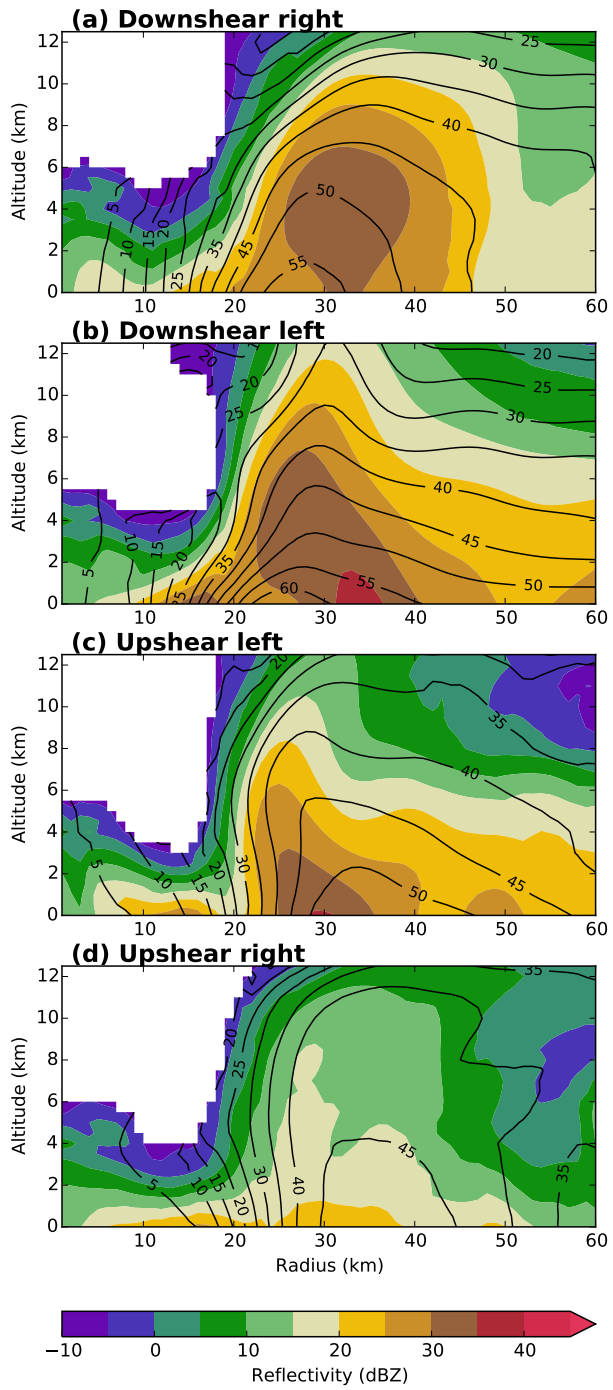

Figure 39: *Shear-relative, spatio-temporal averages of radar reflectivity (shaded, dBZ) and tangential wind speed (contours, m s^{-1}) for each quadrant. The variables are averaged azimuthally within each shear-relative quadrant and over all four periods.*

only discernible at low levels, is located outside of 30 km. Overall, the shear-relative spatio-temporal averages of radar reflectivity and tangential wind speed of Hurricane Rita on 23 September match very well with the structure that was found in other sheared storms, and illustrates the convective evolution from initiation to maturation to dissipation.

The differences between the four shear-relative quadrants are also evident in wavenumber-1 perturbation pressure and radial wind speed (Fig. 40). The downshear right quadrant exhibits the typical pattern of low-level inflow and upper level outflow in active eyewall convection, with deep low-level inflow, reaching up to about 3.5 km and penetrating inward to about 20 km radius, and deep upper level outflow above 6 km, its strength increasing with height. The low-level inflow is collocated with positive pressure perturbations, and the upper-level outflow is collocated with negative pressure perturbations. The pressure perturbations become negative with height, which means that the pressure perturbation gradient force is directed upward. The convectively-mature, downshear left quadrant exhibits outflow at low levels and weak inflow at upper levels. The radial velocity is negative toward the inner edge of the eyewall, where the air is cascading downward into the eye. The perturbation pressure at low levels is maximized at around 30 km radius. The perturbation

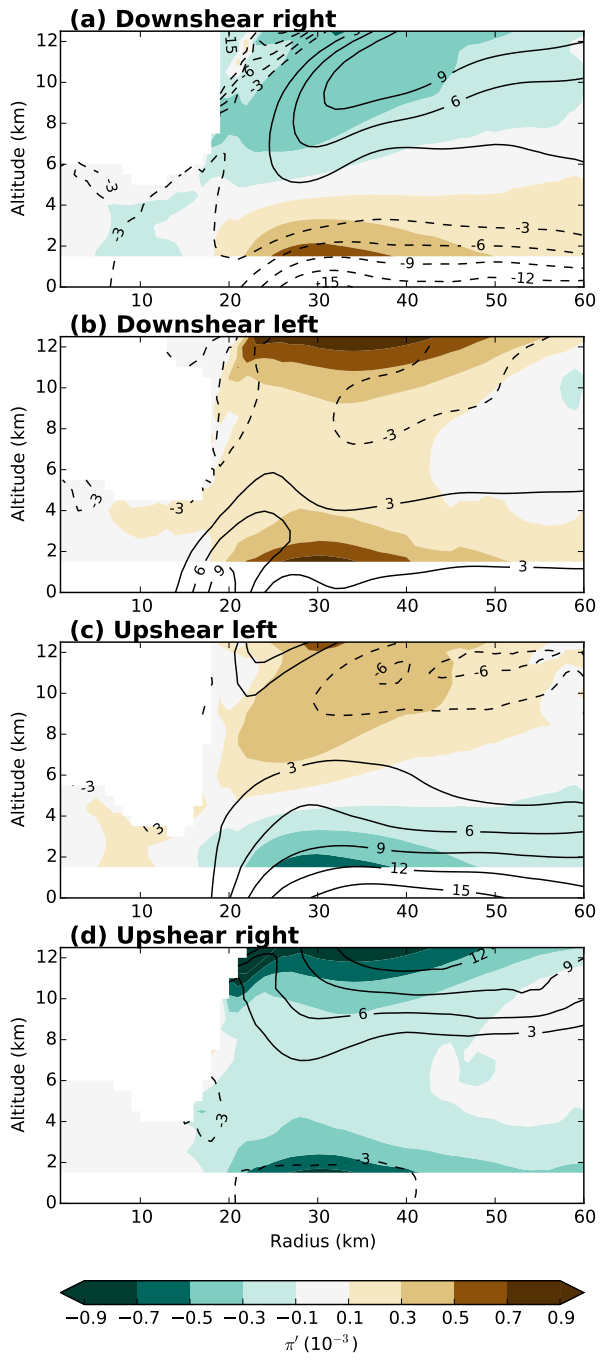

Figure 40: *Shear-relative, spatio-temporal averages of the wavenumber-1 component of perturbation pressure (shaded, 10^{-3}) and radial wind speed (contours, m s^{-1}) for each quadrant. The variables are averaged azimuthally within each shear-relative quadrant and over all four periods.*

pressure is positive at lower and upper levels and reaches a minimum at midlevels. Hence, the perturbation pressure gradient force is directed upward at low levels below about 6 km, and directed downward at the levels above.

The upshear left quadrant shows a pattern that is roughly opposite of the pattern in the downshear right quadrant. At low levels, outflow is quite deep, stretching up to 6.5 km altitude at its maximum extent. At upper levels, the outflow is confined to inner radii, meeting deep inflow at about 30 to 40 km radius. The perturbation pressure shows negative values at low levels and positive values at upper levels, with a maximum at around 30 km radius. Hence, the perturbation pressure gradient force is directed downward in this quadrant. The upshear right quadrant exhibits weak inflow at low levels and stronger outflow at upper levels. The perturbation pressure is negative at lower and upper levels, and is close to zero at midlevels, hence the perturbation pressure gradient force is directed downward below about 6 km, and directed upward above this level.

Overall, the wavenumber-1 pressure perturbations show a close connection to the radial wind field and the vorticity field. Both at low and at upper levels, positive pressure perturbations are generally collocated with inbound radial velocities, and negative pressure perturbations are collocated with

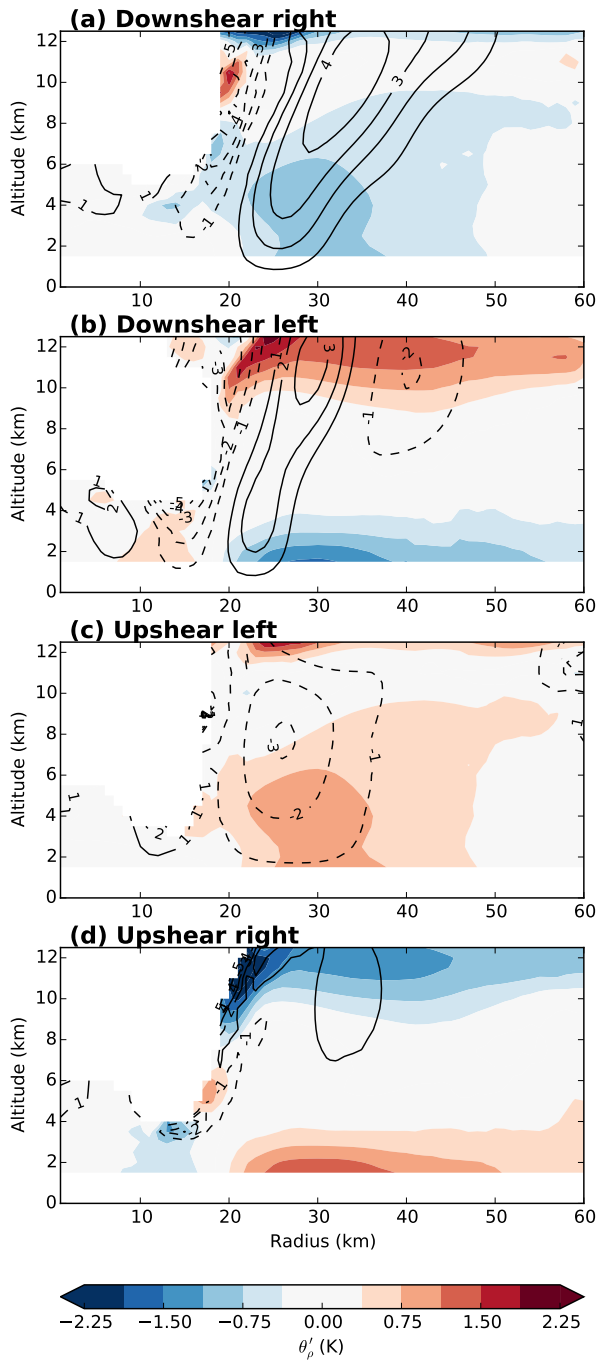

Figure 41: *Shear-relative, spatio-temporal averages of the wavenumber-1 component of density potential temperature perturbation (shaded, K) and vertical wind speed (contours, m s^{-1}) for each quadrant. The variables are averaged azimuthally within each shear-relative quadrant and over all four periods.*

outbound radial velocities.

The shear-relative wavenumber-1 density potential temperature perturbations and vertical velocities also display clear distinctions between the four shear-relative quadrants (Fig. 41). The downshear right quadrant, associated with convective initiation, shows upward motion between 20 and 50 km radius, and downward motion at the inner edge of the eyewall. The wavenumber-1 cold temperature anomalies are located in a broad area below 9 km, collocated and radially outside of the column of upward motion. The downshear left quadrant, associated with convective maturation, exhibits more a more upright column of upward motions, located between 20 and 30 km radius. As in the downshear right quadrant, strong downward motion can be seen cascading down the inner edge of the eyewall. The temperature anomalies show cold anomalies below 4 km, warm anomalies above 9 km, and values close to zero inbetween. This temperature pattern with cold anomalies at low levels and warm anomalies at upper levels results in a positive vertical potential temperature gradient, which increases the static stability at low and upper levels in this quadrant. The upshear left quadrant, associated with convective dissipation, displays only negative vertical velocities. The eyewall region between 20 and 30 km radius exhibits negative vertical velocities throughout the depth of the column, with the strongest downward

motion at midlevels around 6 to 8 km altitude. The downward motion is accompanied by warm anomalies below the level of maximum descent. The upshear right quadrant does not show any significant vertical velocities. The temperature perturbations show positive anomalies at low levels and cold anomalies in the outflow layer. This distribution results in decreased static stability at low and upper levels. Overall, the vertical velocities nicely support the interpretation of the eyewall convection in terms of initiation, maturation, and dissipation as the convective cells rotate downstream. The wavenumber-1 temperature perturbation distribution seem to impact the static stability, enhancing it in the downshear quadrants and reducing it in the upshear quadrants.

4.5.4 Mesovortices: Wavenumbers 2 and 3

The importance of the effects of vertical wind shear on the structure of tropical cyclones has been the focus of many previous studies and has been clearly shown in the previous section. Vertical wind shear primarily affects the wavenumber-1 patterns. Higher wavenumbers are associated with eyewall mesovortices and the eyewall convection itself, where mesovortices typically project onto wavenumbers 2 and 3, and the eyewall convection itself projects onto wavenumbers 4 and higher (Braun and Wu, 2007). Using a high-resolution simulation of Hurricane Bonnie (1998), Braun et al. (2006) showed that vertical velocities time-averaged over 6 hours are dominated by a shear-induced wavenumber-1 pattern, whereas instantaneous vertical motion is usually linked to individual, cyclonically rotating mesovortices within the eyewall. They suggest that the preferred location of convective initiation in the downshear direction is a result of the interaction between the eyewall mesovortices and the low-level inflow associated with vertical wind shear.

Our datasets have a temporal resolution of about 30 minutes, hence we are not able to identify individual convective cells. Nevertheless, investigating the higher wavenumbers might result in additional insight into the vortex structure. Power spectra for perturbation pressure and perturbation density potential temperature are computed to examine the relative importance of the individual wavenumbers to the thermodynamic structure of the vortex. The power spectra are calculated individually for each vertical level and each period. The power spectra of all four periods are then averaged per vertical level.

The pressure perturbation power spectra are shown for three different vertical levels, exemplifying low, mid-, and upper levels (Fig. 42). Overall, wavenumber-1 contains the most power. All three levels highlight the dominance of the lower wavenumbers with respect to the higher wavenumbers, with wavenumbers 0 to 3 containing significantly more power than

wavenumbers 4 and higher. The relative importance of wavenumbers 0 to 3 depends on the vertical level. The power in wavenumber-0 is relatively small for mid- and upper levels, whereas it is the wavenumber with the highest power for 2 km altitude. This points to the increased difficulty of defining a reference state at lower levels where friction plays a non-negligible role. The power in wavenumber-1 is equally large for 2 km and 8 km, and slightly smaller for 5 km. The magnitudes of the pressure perturbations at the different vertical levels shown in the previous section indicated this relation. The center of the domain was chosen as the center of the vortex averaged over 2 to 8 km. In most cases (i.e. when the tilt is approximately linear) this means that the center position of the individual level is closest to the vortex center at midlevels, and farther away at lower and upper levels. The power in wavenumber 2 is still quite large, with its magnitude increasing with height, being smallest at 2 km, and largest at 8 km. The power in wavenumber-3 is approximately the same for all three vertical levels, it is slightly less than in wavenumber-2, but still more than in the higher wavenumbers. This power spectrum suggests that wavenumbers 2 and 3 of the perturbation pressure might play a non-negligible role in shaping the eyewall convection.

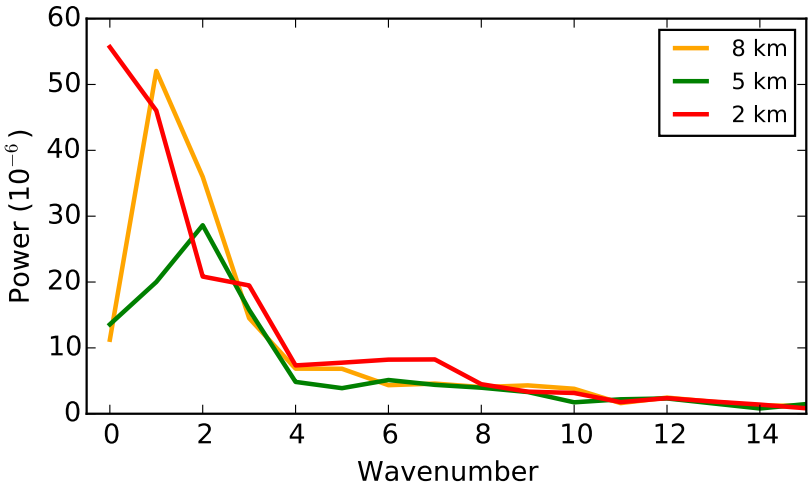

Figure 42: *Power spectrum of perturbation pressure for 2 km (red), 5 km (green), and 8 km altitude (orange), respectively.*

The temperature perturbation power spectrum (Fig. 43) displays some similarities and some discrepancies. As for the perturbation pressure, most of the power is concentrated in the lower wavenumbers, with wavenumbers 4 and higher containing significantly less power than wavenumbers 0 to 3. But, in contrast to the perturbation pressure, the dominance of wavenumber-1 over wavenumbers 2 and 3 is much larger. Wavenumber-1 contains by far the most power. The power in wavenumber 0 is very low, except for the 2 km level, which again points to the difficulty of the choice of the reference state definition in the boundary layer. The power in wavenumber-1 varies slightly with height, with the mid-levels containing

the largest value. The power drops off significantly from wavenumber 1 to wavenumber 2 for all three vertical levels, and the power in wavenumber-3 is only marginally higher. This power spectrum suggests that wavenumbers 2 and 3 are not as important for the temperature perturbations as they are for the pressure perturbations. Hence, the remainder of this section will focus on wavenumbers 2 and 3 of the pressure perturbations.

Wavenumbers 2 and 3 of perturbation pressure, tangential wind speed, radial wind speed, and vertical wind speed are presented in terms of horizontal cross sections, similar to the wavenumber-1 plots in the previous section. The wavenumber 2 and 3 perturbation pressure (Fig. 44) shows a very consistent pattern across all vertical levels and periods, with the wavenumber-2 dominating everywhere, except for the low and mid- levels at 2140 UTC, where a wavenumber-3 pattern is apparent. The perturbation pressure pattern is very consistent with radius and height, with little to no rotation in the radial or vertical direction, and most of the domain exhibiting non-zero values. The mature convection in the northern part of the eyewall is always collocated with a positive wavenumber-2 anomaly, whereas convective initiation in the eastern part of the eyewall and convective dissipation in the western part of the eyewall are collocated with negative anomalies.

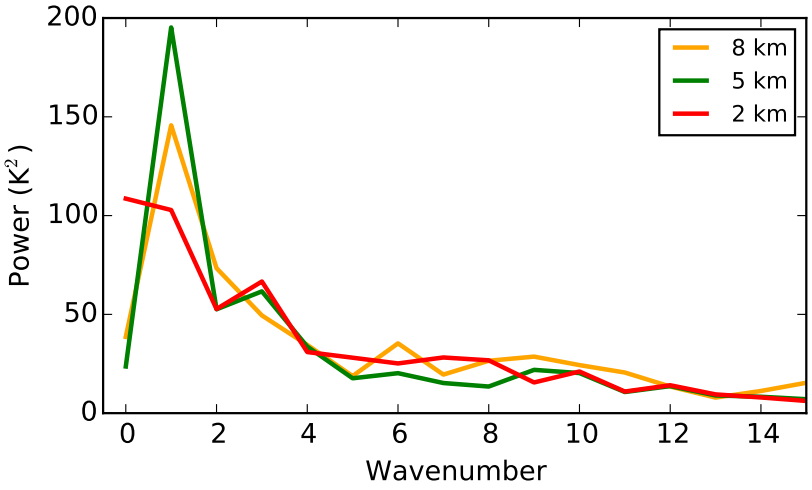

Figure 43: *Power spectrum of perturbation density potential temperature for 2 km (red), 5 km (green), and 8 km altitude (orange), respectively.*

Wavenumber-2 perturbation pressure anomalies have been linked to vortex Rossby waves in previous studies (e.g. Wang and Wu, 2004). Theory predicts that vortex Rossby waves (VRWs) propagate at approximately half the advective speed (Montgomery and Kallenbach, 1997). With an RMW of about 29 km and a tangential wind speed of 48 m s^{-1} the orbital period for Hurricane Rita is estimated to be about an hour. Thus, a wavenumber-2 VRW would rotate about 90° during a 30-min period. The perturbation pattern in Fig. 44 is roughly the same for all four periods, hence it is either stationary or it is the effect of a wave moving at the advective speed. The temporal resolution precludes a definitive answer to this

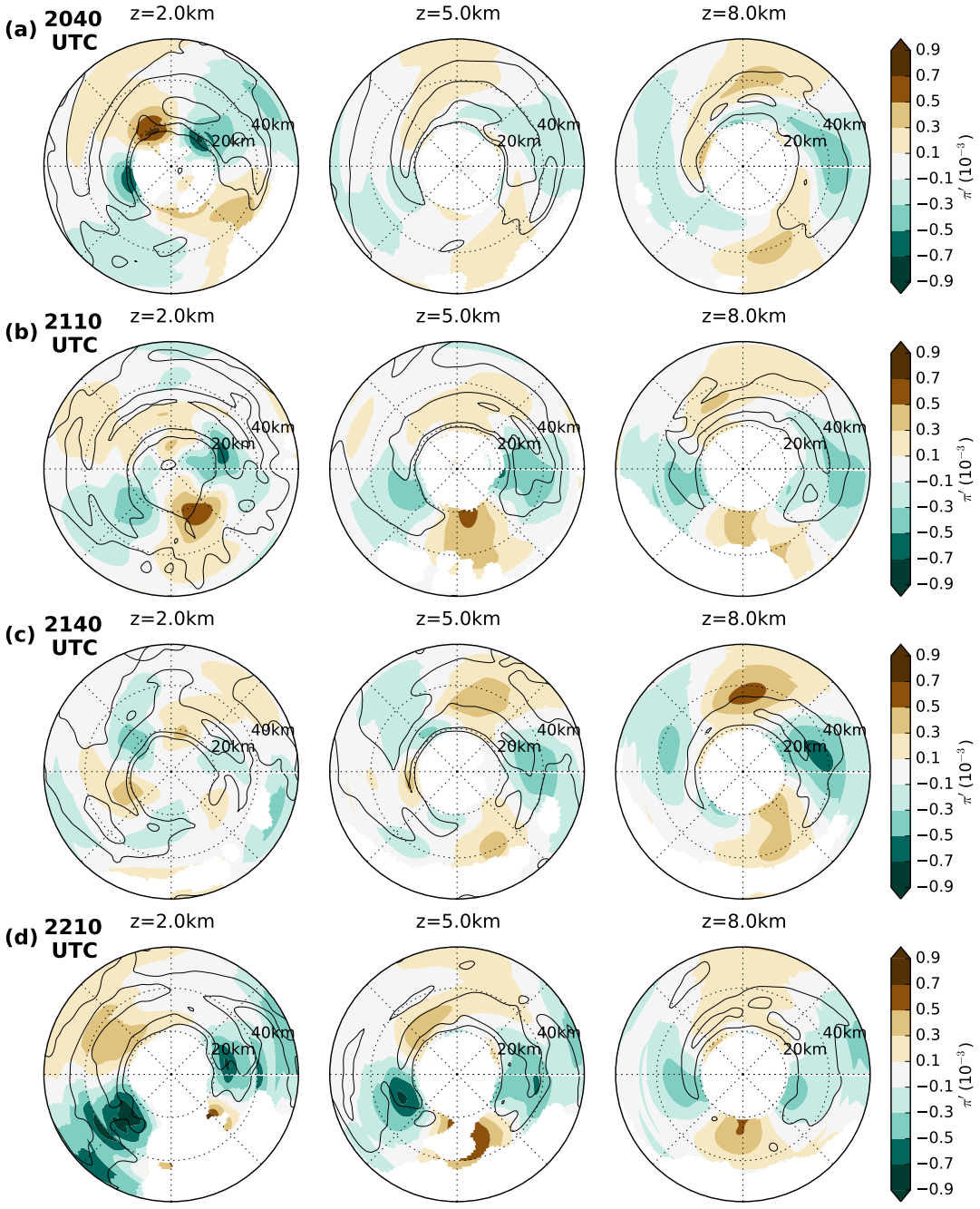

Figure 44: *Horizontal cross sections of the wavenumber-2 and -3 components of perturbation pressure (shaded, 10^{-3}) for 2 km (left), 5 km (center), and 8 km altitude (right) for 2040 UTC, 2110 UTC, 2140 UTC, and 2210 UTC. Radar reflectivity (black contours at 20, 30, 40, and 50 dBZ) is added for orientation.*

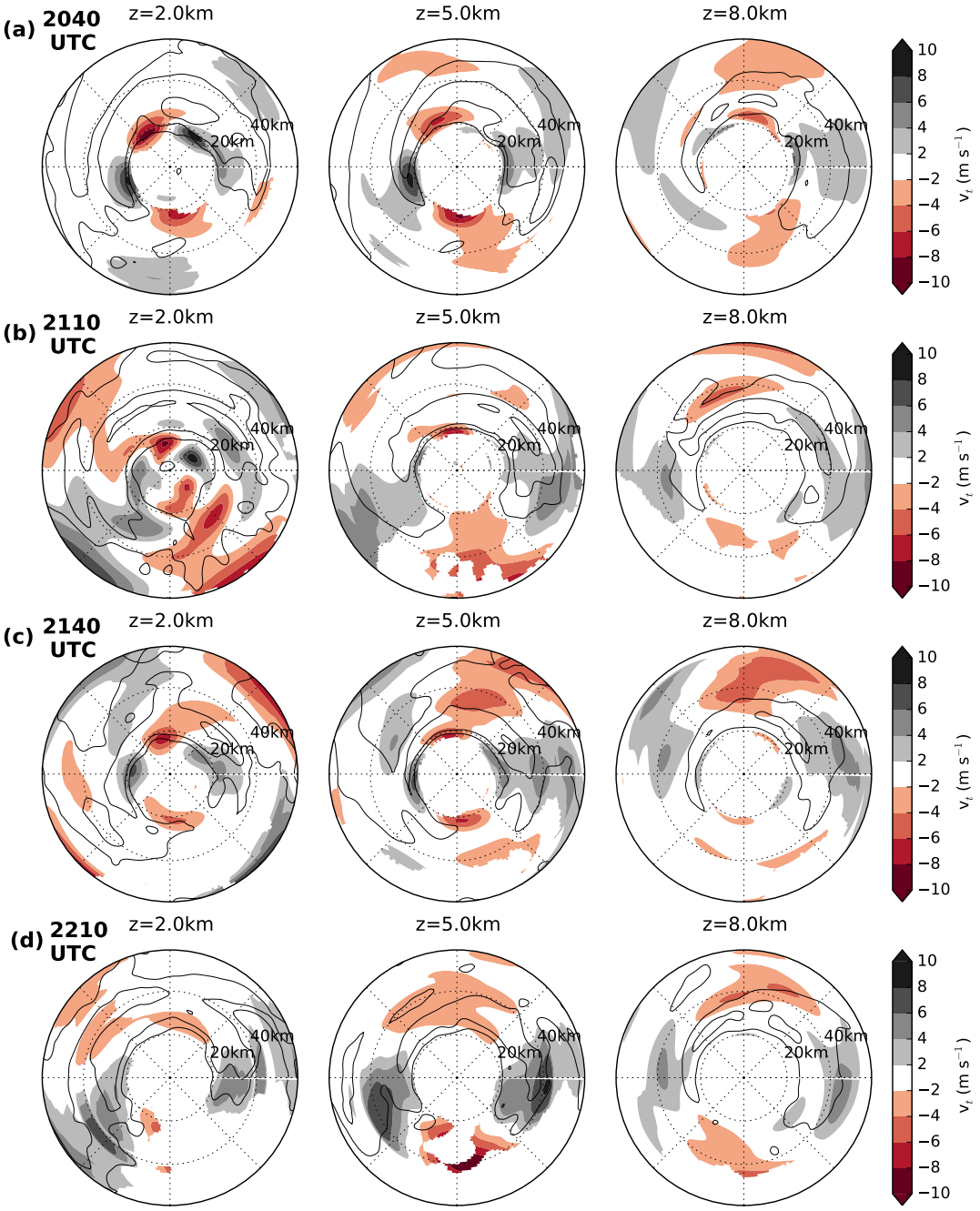

Figure 45: *Horizontal cross sections of the wavenumber-2 and -3 components of tangential velocity (shaded, m s^{-1}) for 2 km (left), 5 km (center), and 8 km altitude (right) for 2040 UTC, 2110 UTC, 2140 UTC, and 2210 UTC. Radar reflectivity (black contours at 20, 30, 40, and 50 dBZ) is added for orientation.*

question, but based on this analysis a VRW moving at half the advective speed can be ruled out as the cause for the wavenumber-2 perturbation pressure pattern.

The wavenumber 2 and 3 tangential wind field (Fig. 45) exhibits a pattern very similar to the pressure perturbations. The tangential wind anomalies are very consistent across all vertical levels and periods. The wavenumber-2 dominates everywhere. The mature convection in the northern part of the eyewall contains negative tangential velocity anomalies, whereas the eastern and western parts show positive tangential velocity anomalies.

The wavenumber-2 and -3 radial wind field (Fig. 46) appears to be rotated azimuthally by 45° compared to the perturbation pressure and tangential wind fields. Again, wavenumber-2 dominates at all vertical levels and times, and the pattern does not rotate with height. The anomalies are mostly confined to the eyewall itself and don't extend to larger radii. The positive anomalies are located in the northeast and southwest of the eyewall, whereas the negative anomalies are located to the southeast and northwest. The radial velocity anomalies are smallest at the 2 km level and at 2110 UTC, and strongest at mid- and upper levels at 2040 UTC and 2140 UTC.

The wavenumber-2 and -3 radial and tangential velocities are combined into wind vectors to get a better picture of the flow field relative to the pressure perturbations (Fig. 47). To highlight the eyewall region the plotting domain was limited to 40 km radius. The most notable feature in these plots of the wavenumber-2 and 3 flow field is the deformation flow pattern occuring in about 50% of the cross sections. The deformation flow is strongest at 2040 UTC and 2140 UTC, stretching across at least two of the vertical levels. The deformation flow is oriented such that the inflow is located toward the southeast and northwest, and the outflow is located toward the southwest and northeast. The inflow is mostly collocated with positive pressure perturbations, and the outflow is mostly collocated with negative pressure perturbations. The flow field also shows that positive tangential velocity perturbations are usually collocated with a transition from positive to negative pressure perturbations, and negative tangential velocity perturbations are collocated with a transition from negative to positive pressure perturbation. Thus, the tangential flow pattern is consistent with the horizontal pressure gradients for cyclonic flow. However, at 2140 UTC, the pressure pattern is dominated by a wavenumber 2, whereas the velocity is dominated by a wavenumber 3, which means that the relationship between pressure perturbation and flow field is not as clear in this case, or that the pressure perturbation is only linked to the wavenumber-2 flow field and not to its wavenumber-3 component.

The wavenumber-2 and -3 vertical velocities (Fig. 48) again show the predominance of the

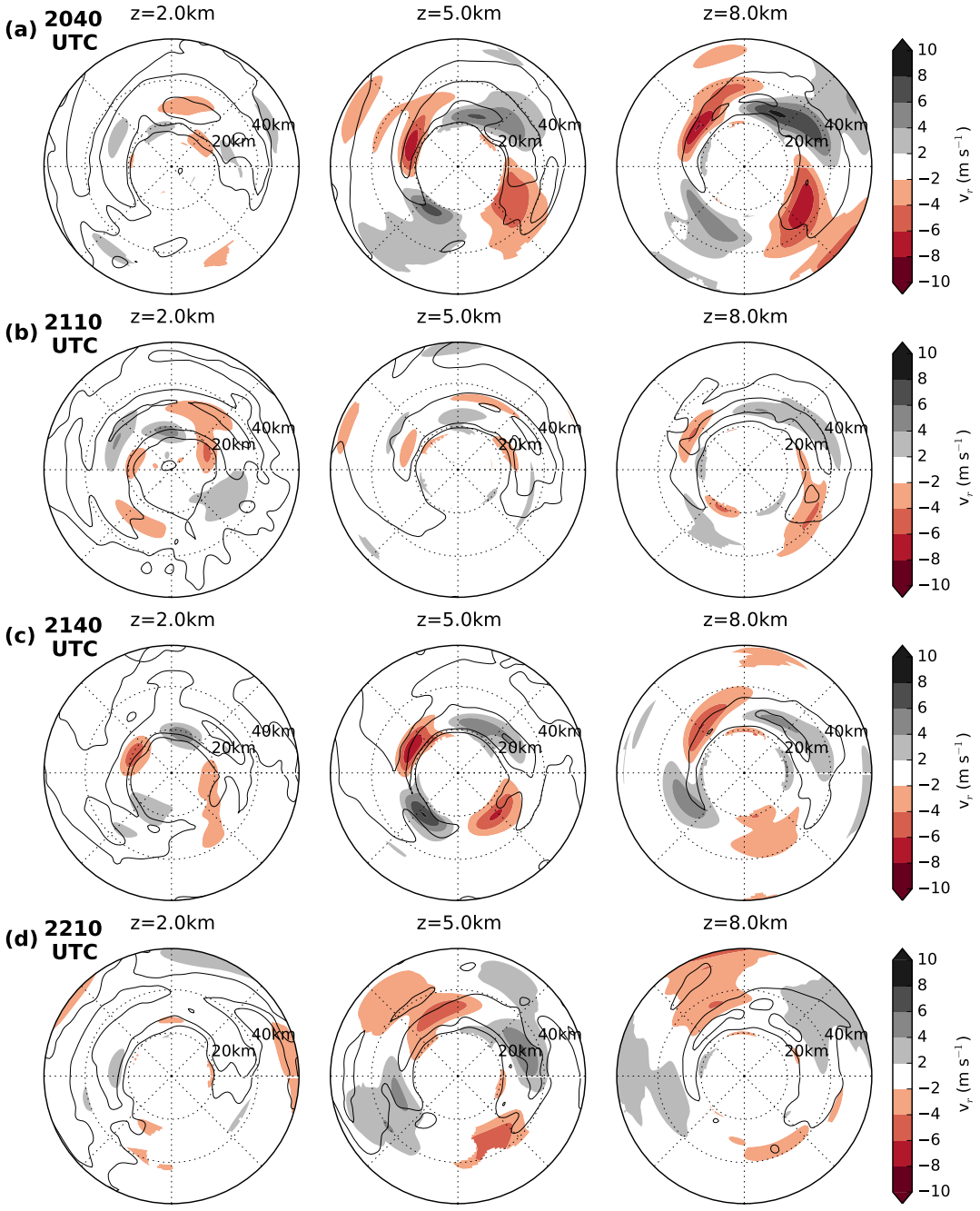

Figure 46: *Horizontal cross sections of the wavenumber-2 and -3 components of radial velocity (shaded, m s^{-1}) for 2 km (left), 5 km (center), and 8 km altitude (right) for 2040 UTC, 2110 UTC, 2140 UTC, and 2210 UTC. Radar reflectivity (black contours at 20, 30, 40, and 50 dBZ) is added for orientation.*

wavenumber-2. Positive anomalies are mostly located to the north and south, whereas the negative anomalies are located to the east and west. The anomalies are strongest at the inner edge of the eyewall. The behavior at outer radii varies from period to period, with anomalies near zero at 2040 UTC, a more complex pattern with negative anomalies outside of positive anomalies and vice versa at 2110 UTC, and an outward spiraling pattern at 2140 UTC. Overlaying the horizontal wavenumber-2 and -3 flow field onto the vertical velocities and focussing on the eyewall region shows that the regions with positive tangential velocity anomalies are usually collocated with negative vertical velocity anomalies, and the regions of enhanced outflow (e.g. to the northeast of the center) are usually collocated with a transition from negative to positive vertical velocity anomalies. In summary, the perturbation pressure and the three wind vector components show a clear wavenumber-2 signature. The positive pressure perturbations are mainly collocated with decreased tangential velocities, downward vertical motion, and a transition from outward to inward radial velocities, whereas negative pressure perturbations are collocated with increased tangential velocities, upward vertical motion, and a transition from inward to outward radial velocities.

Deformation flow patterns in tropical cyclones have been mentioned in previous literature in the context of elliptical eyewalls (Yamauchi et al., 2002). Large-scale environmental flow had been suggested as one of the mechanisms to cause the eyewall ellipticity. The other suggested mechanism was a wavenumber-2 Rossby wave (Kuo et al., 1999, Lee et al., 2006). Braun (2002) found a stationary wavenumber-2 deformation flow in his simulation of Hurricane Bob (1991). He attributed it to an environmental deformation flow pattern caused by an approaching trough to the west, the subtropical high to the east, and weaker westerly flow to the southwest of Bob. He argued that this environmental flow pattern is typical for recurving storms and thus deformation might impact the storm structure of recurving storms. Another possible mechanism to create a wavenumber-2 would be the superposition of two perpendicular wavenumber-1 patterns. Storm motion and tilt direction are oriented perpendicular in the case of Rita. However, if and how the interaction of storm motion and tilt can result in a wavenumber-2 flow field is unclear.

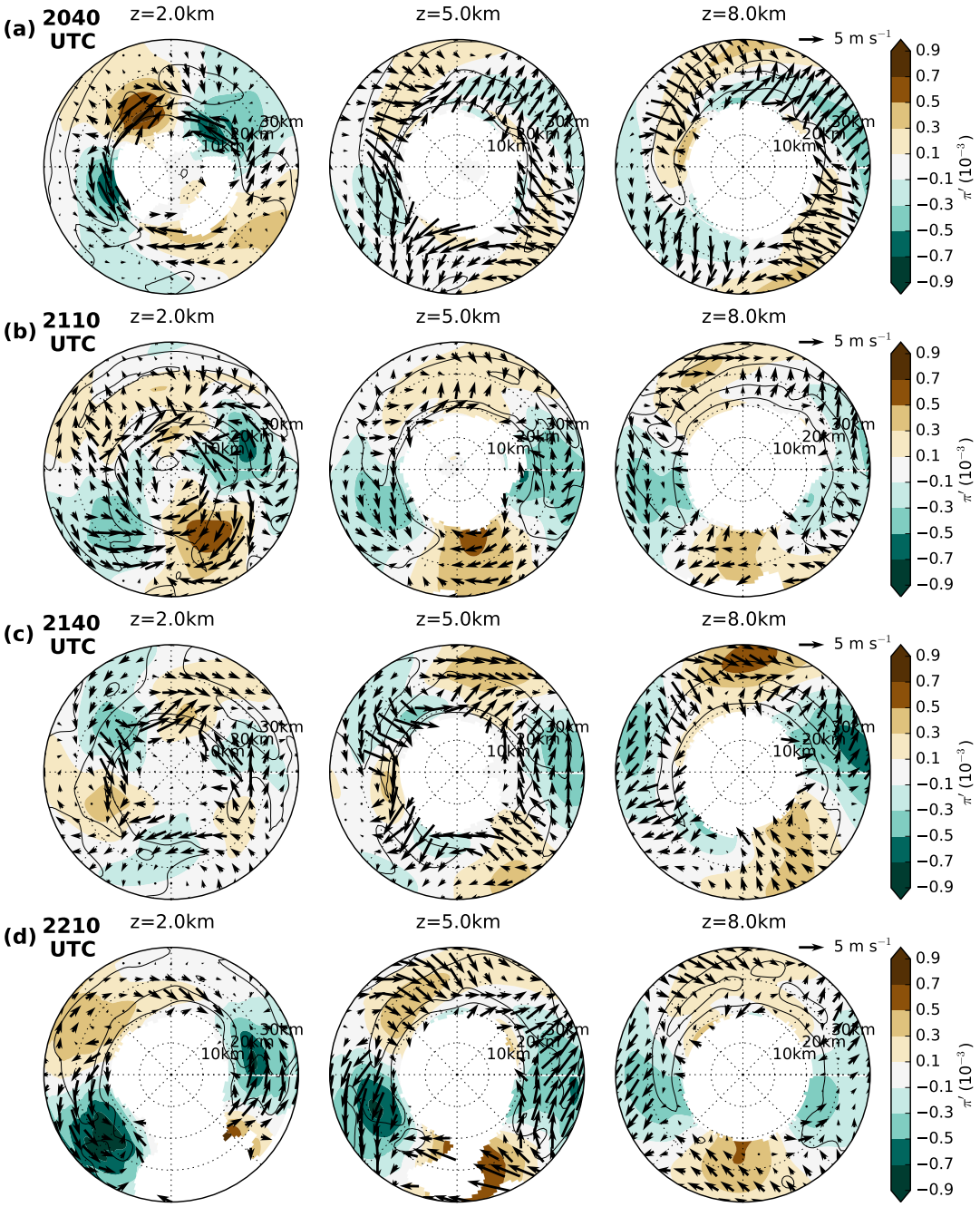

Figure 47: *Horizontal cross sections of the wavenumber-2 and -3 components of perturbation pressure (shaded, 10^{-3}) and the wavenumber-2 and -3 components of horizontal wind speed (arrows, m s^{-1}) for 2 km (left), 5 km (center), and 8 km altitude (right) for 2040 UTC, 2110 UTC, 2140 UTC, and 2210 UTC. Radar reflectivity (black contours at 20, 30, 40, and 50 dBZ) is added for orientation. The domain size is reduced to 40 km in the radial direction, compared to 60 km in Figs. 44 - 46.*

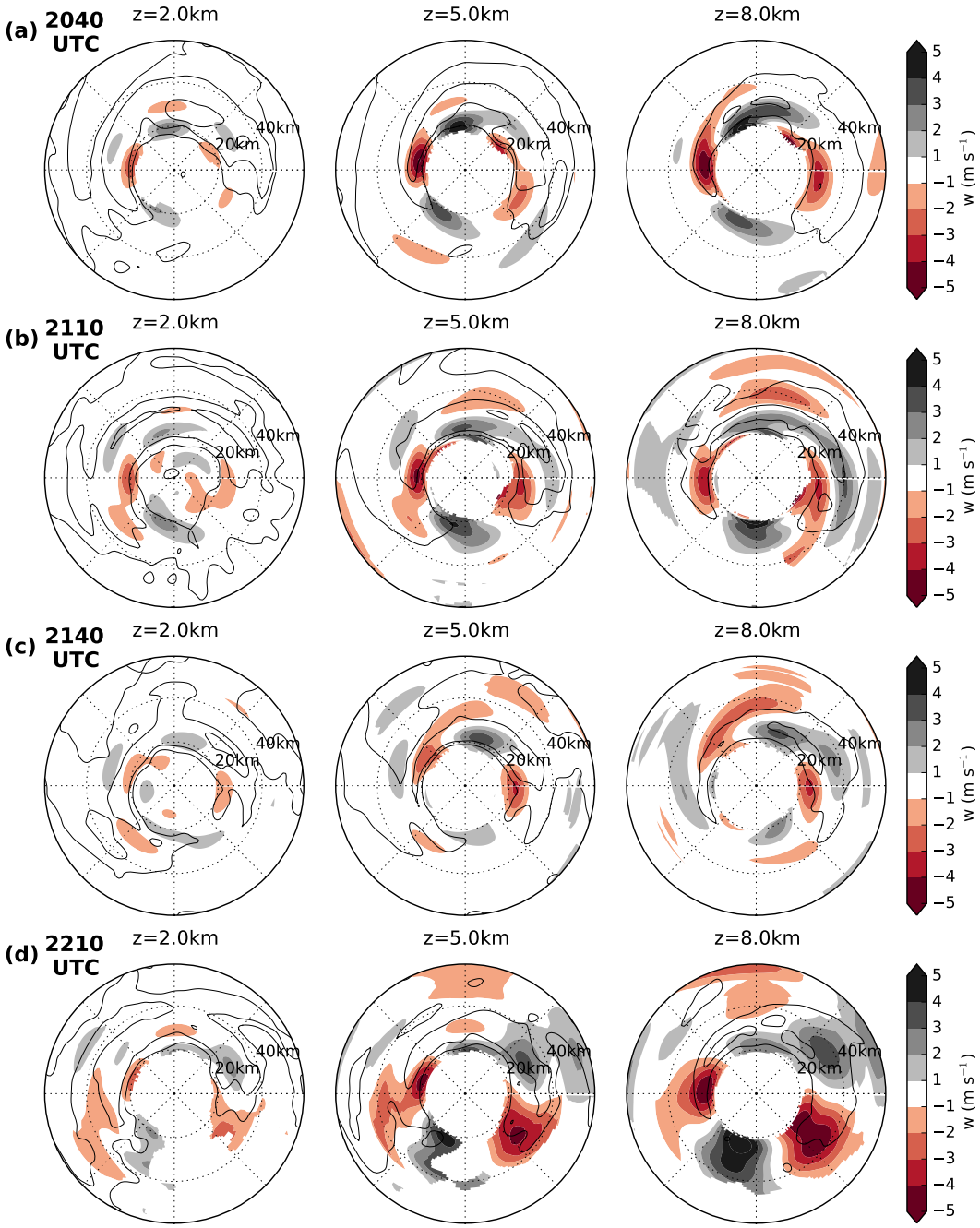

Figure 48: *Horizontal cross sections of the wavenumber-2 and -3 components of vertical velocity (shaded, m s^{-1}) for 2 km (left), 5 km (center), and 8 km altitude (right) for 2040 UTC, 2110 UTC, 2140 UTC, and 2210 UTC. Radar reflectivity (black contours at 20, 30, 40, and 50 dBZ) is added for orientation.*

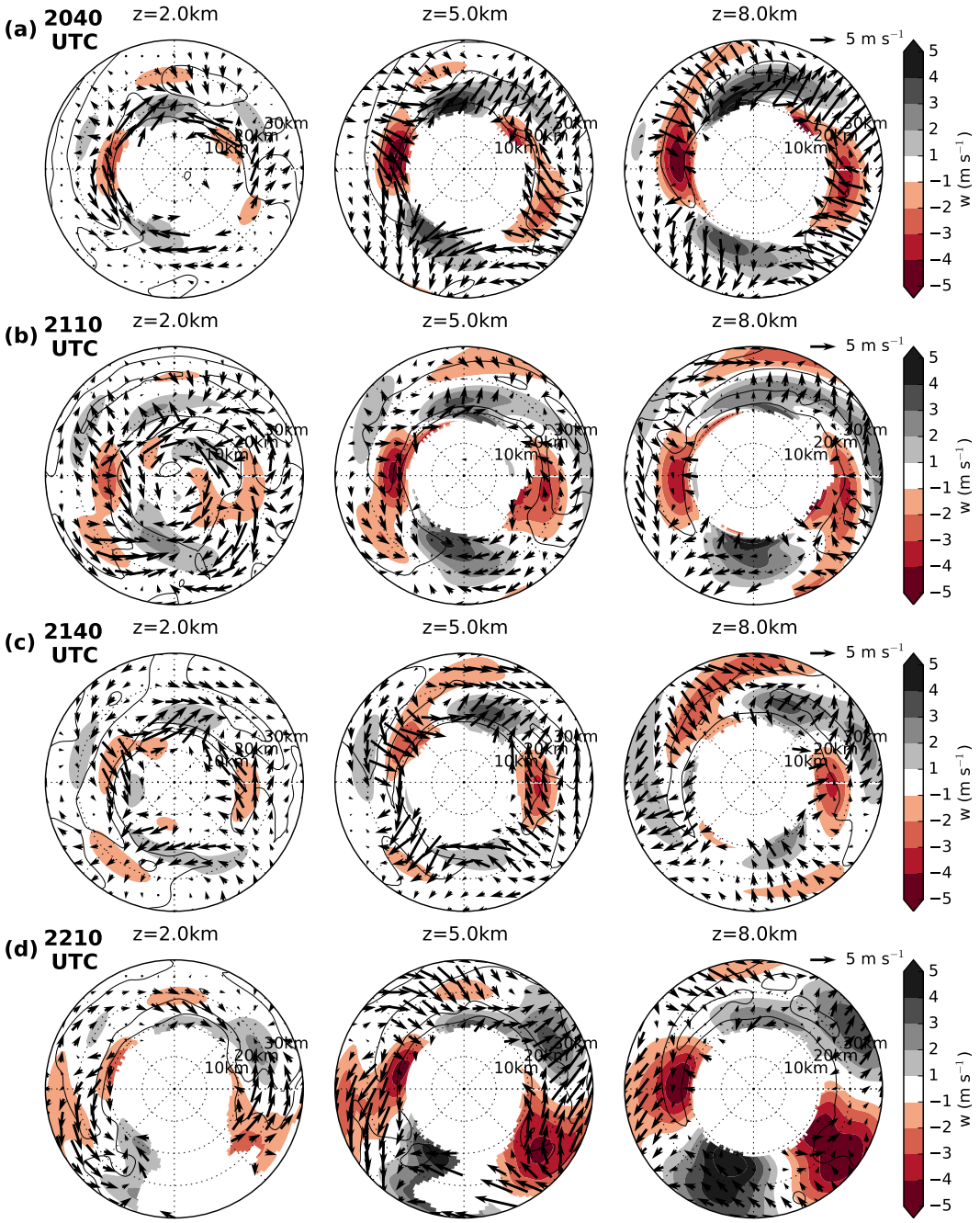

Figure 49: *Horizontal cross sections of the wavenumber-2 and -3 components of vertical velocity (shaded, m s^{-1}) and the wavenumber-2 and -3 components of horizontal wind speed (arrows, m s^{-1}) for 2 km (left), 5 km (center), and 8 km altitude (right) for 2040 UTC, 2110 UTC, 2140 UTC, and 2210 UTC. Radar reflectivity (black contours at 20, 30, 40, and 50 dBZ) is added for orientation. The domain size is reduced to 40 km in the radial direction, compared to 60 km in Figs. 44 - 46.*

4.5.5 Eyewall Convection: Higher-order Wavenumbers

Airborne radar data can provide a very detailed look at the structure of the eyewall. However, even the high-resolution airborne radar data can't resolve the evolution of individual convective cells, because the data has to be composited over a certain period of time. WSR88D reflectivity data from Houston-Galveston, TX (KGHX) and Lake Charles, LA (KLCH) illustrate the high degree of variability of the eyewall convection during a period of 22 minutes (Fig. 50), roughly corresponding to the second analysis period (2110 UTC). The distance of the radars to the center of the analysis domain is 272 km (KGHX) and 210 km (KLCH), respectively, with KLCH located toward the north-northwest of Rita (344°) and KHGX located toward the north-west of Rita (298°). The large distance between the radars and the storm results in the limitation of the WSR88D data to levels above 5 km and introduces some beam-broadening artifacts, which result in slightly different depictions of the eyewall convection by the two radars. Snapshots from both radars show the asymmetric structure of the storm, with high reflectivities in the northern semicircle and small or no radar returns in the southern portion of the eyewall. The appearance of the eyewall changes from snapshot to snapshot. For example, at 2111 UTC, the KLCH radar shows four distinct cells exceeding 35 dBZ toward the north and northeast. The same four cells can be seen with the KHGX radar, they are, however, elongated in the across-beam direction as a result of the beam-broadening. As time progresses, the highest reflectivities shift to the north (2116 UTC), and then to the northwest (2121/2122 UTC). The formation of a new cell can be seen at 2121/2122 UTC, detached from the rest of the eyewall toward the southeast of the center. This cell matures (2127 UTC) and then merges with the rest of the eyewall (2132 UTC).

The 30-min resolution of the SAMURAI analyses makes it difficult to interpret the higher wavenumbers in terms of individual convective cells. The cyclonic advection of the eyewall convection with the mean tangential wind acts to blur the results. Hence, a statistical approach is taken to examine the thermodynamic properties of updrafts in the eywall.

A histogram of the perturbation density potential temperature θ'_ρ of all updrafts in the eyewall region (15 km $\leq$ r $\leq$ 40 km, 2 km $\leq$ z $\leq$ 12 km) for the four different periods (Fig. 51a) shows that the distributions are similar for all periods and are shifted toward negative values. The average perturbation density potential temperature computed from these histograms ranges between -0.54 K and -0.76 K. This shift to negative values is largely due to the fact that most updrafts occur in the downshear quadrants, and that these downshear quadrants exhibit a shear-induced wavenumber-1 cold anomaly. The shear-induced wavenumber-1, however, is quasi-balanced. It makes sense to look at the perturbation density potential

temperature not only relative to a vortex in thermal wind balance, but additionally include the shear-induced wave- number-1 into the reference state and thus subtracting off the wavenumber-1 contribution of the perturbation density potential temperature. The distributions of this "unbalanced" perturbation density potential temperature (Fig. 51b) show a Gaussian shape centered around zero for all periods, with the majority of the gridpoints exhibiting temperature perturbations of less than 2 K (e-folding is approximately ± 2K). Hence, there are approximately the same number of positively buoyant and negatively buoyant updrafts with respect to a reference state which includes shear effects. These distributions include all gridpoints with positive vertical velocities, ranging from values just above zero to strong updrafts. Limiting the distributions to gridpoints with vertical velocities in excess of 5 m s^{-1} results in a shift of the distribution to the right (Fig. 51c). Gridpoints with

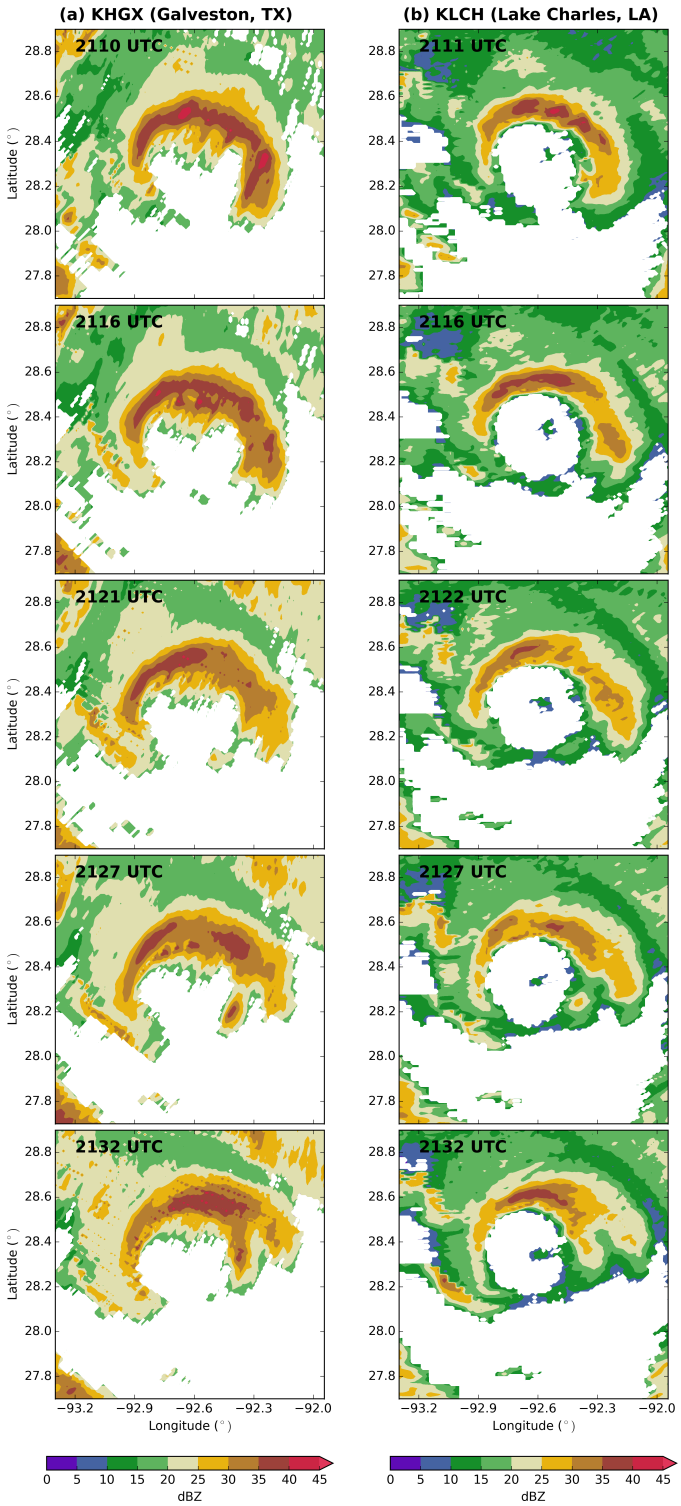

Figure 50: *Sequence of 8-km constant altitude radar reflectivity (shaded, dBZ) of Hurricane Rita as recorded by WSR88-D radars in (a) Lake Charles, LA (KLCH), and (b) Houston-Galveston, TX (KHGX) on 23 September 2005.*

strong vertical motion are more likely to have positive than negative temperature perturbations. To test the robustness of this result average temperature perturbations for gridpoints exceeding a certain vertical velocity threshold are computed. Thresholds are chosen as increments of 1 m s^{-1}, from zero to ten m s^{-1}. Only gridpoints in the downshear quadrants are included to focus on the earlier times of the convective lifecycle.

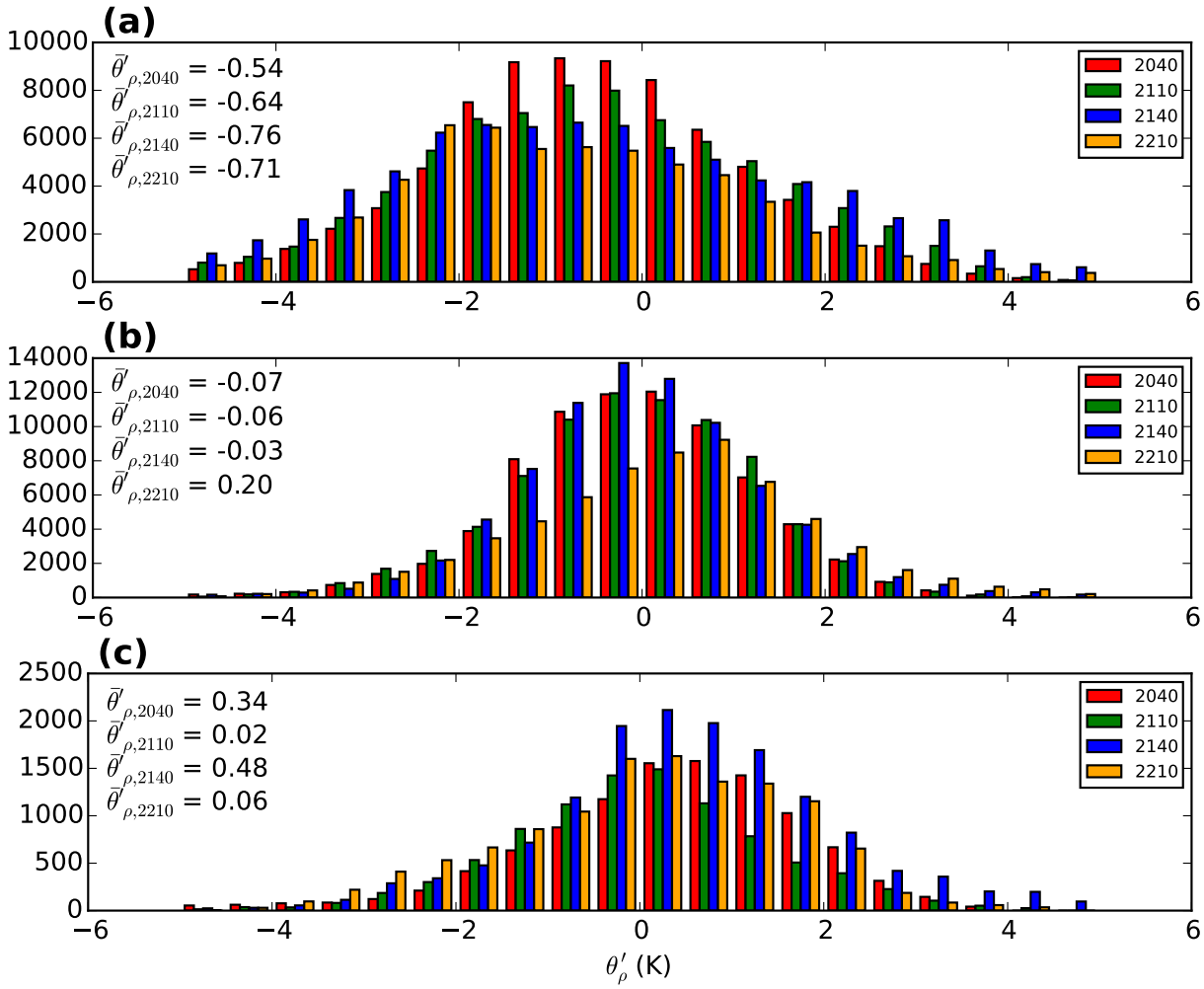

Figure 51: *Histograms of perturbation density potential temperature for gridpoints in the eyewall (15 km $\leq r \leq$ 40 km, 2 km $\leq z \leq$ 12 km) with positive vertical velocity for each period (red: 2040 UTC, green: 2110 UTC, blue: 2140 UTC, orange: 2210 UTC) for (a) the total θ'_ρ, (b) the unbalanced θ'_ρ, i.e. θ'_ρ minus its wavenumber-1 component, and (c) the unbalanced θ'_ρ for all gridpoints with a vertical velocity exceeding 5 m s^{-1}. The average θ'_ρ for each scenario and period is inserted in the respective plot.*

All periods show monotonically increasing average temperature perturbations with increasing vertical velocity (Fig. 52a). The last values for 2140 UTC and 2210 UTC are an exception and are most likely due to the limited number of gridpoints exceeding the respective threshold. The increase is strongest for 2040 UTC, but all periods show a dependence of the average temperature perturbation on the velocity threshold, with higher temperature perturbations for stronger updrafts. In contrast, no dependence of the average vertical velocity can be found with increasing temperature perturbation thresholds (Fig. 52b). Similiar to thresholding on the vertical velocity, as in Fig. 52a, we now threshold on the unbalanced density potential temperature perturbations in increments of 0.33 K, from zero to 3 K, and then average the vertical velocity of all these gridpoints. All periods show a positive, constant average vertical velocity up to a threshold of 2 K. Above that, the average vertical velocity decreases for all periods, except 2140 UTC. Hence, on average, gridpoints with strong updrafts have higher, positive temperature per-

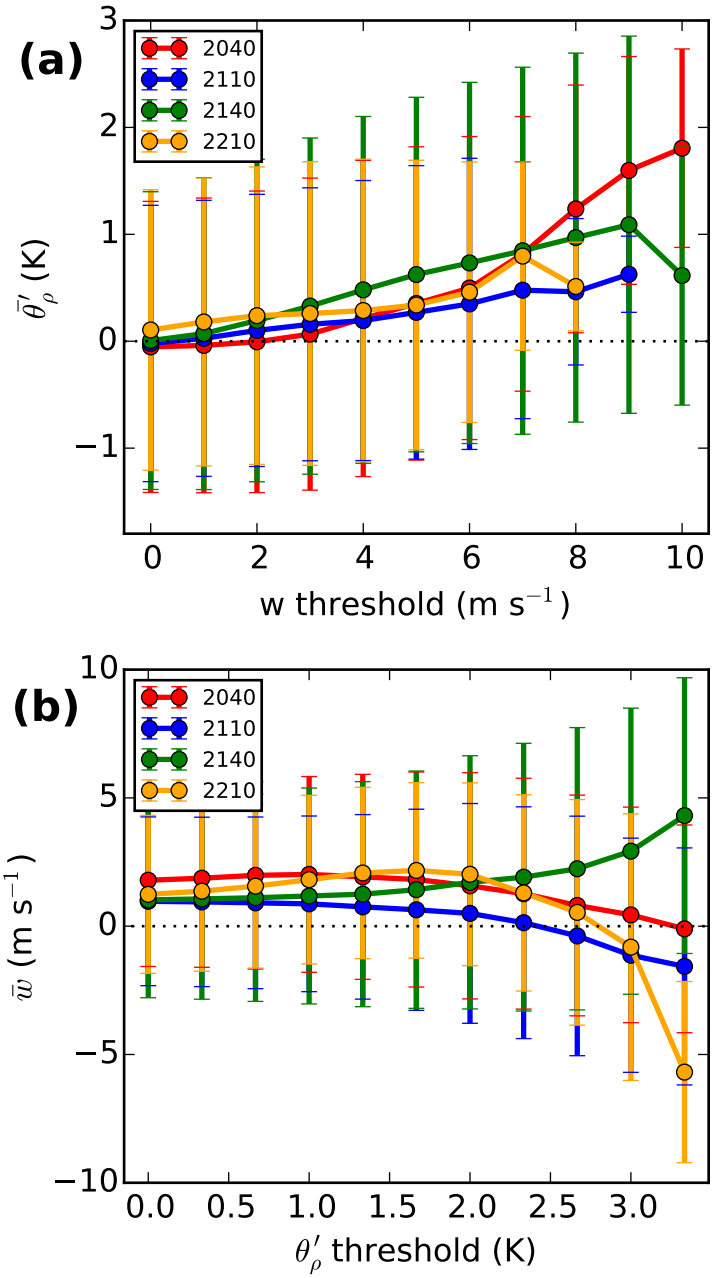

Figure 52: *(a)Unbalanced θ'_ρ averaged over all gridpoints in the downshear quadrants that exceed a certain vertical velocity threshold for 2040 UTC (red), 2110 UTC (blue), 2140 UTC (green), and 2210 UTC (orange). (b) Vertical velocity averaged over all gridpoints in the downshear quadrants that exceed a certain unbalanced θ'_ρ threshold. Vertical errorbars indicate the standard deviations.*

turbations, but gridpoints with higher temperature perturbations do not necessarily have stronger updrafts. There is no direct correlation between temperature perturbations and vertical velocity. Higher vertical velocities are accompanied by stronger positive temperature anomalies, but the magnitude of the temperature anomalies does not indicate the strength of the vertical velocity.

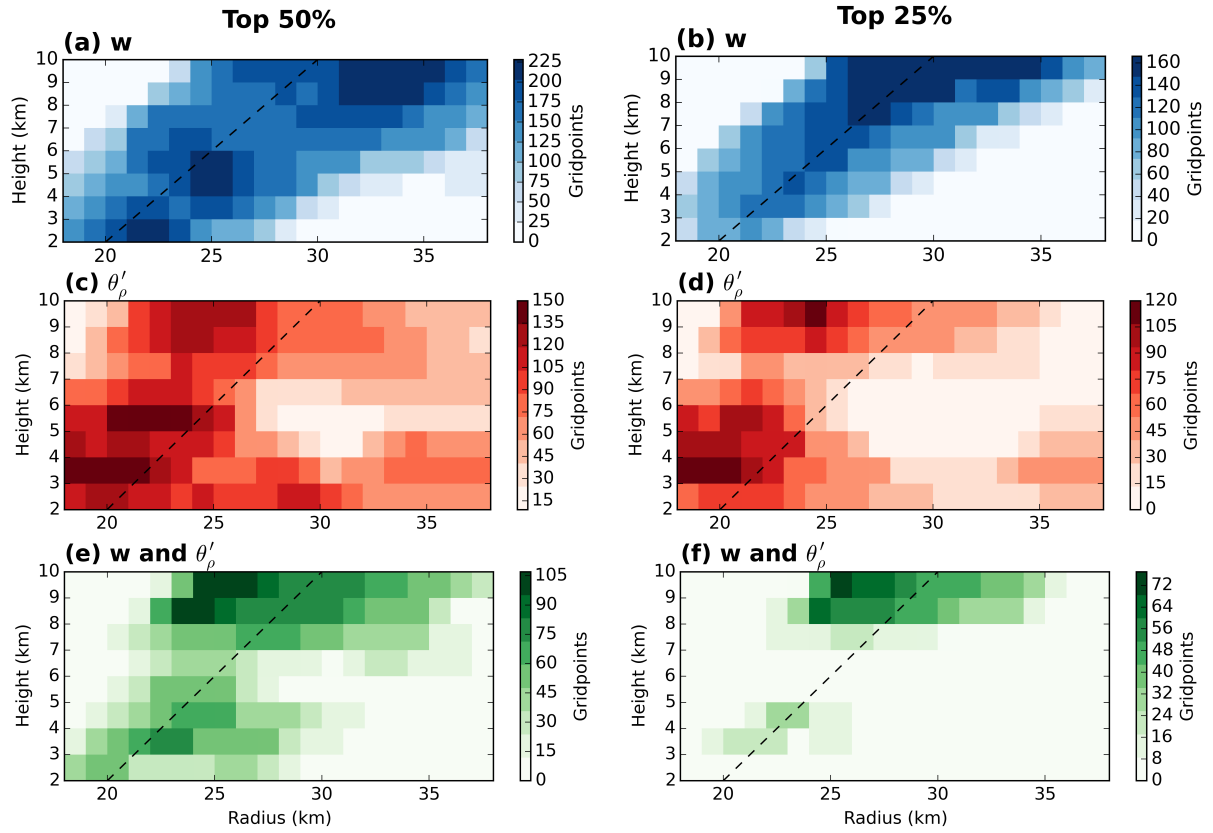

Figure 53: *Two-dimensional radius-height histograms of gridpoints in the downshear quadrants at 2040 UTC exceeding a certain (a, b) vertical velocity, (c, d) unbalanced θ'_ρ, and (e, f) combination of vertical velocity and unbalanced θ'_ρ. The left column (a, c, e) show histograms for gridpoints with vertical velocities exceeding 2.43 m s^{-1} and/or unbalanced θ'_ρs exceeding 0.83 K, which corresponds to the top 50% of positive vertical velocities and positive temperature perturbations. The right column (b, d, f) shows histograms for gridpoints with vertical velocities exceeding 4.08 m s^{-1} and/or unbalanced θ'_ρs exceeding 1.50 K, which corresponds to the top 25% of positive vertical velocities and positive temperature perturbations. The dashed line shows the mean radial location of the top 25% vertical velocities with height for orientation.*

The location of these gridpoints with high vertical velocities and high temperature perturbations is investigated using 2D-histograms (Fig. 53) for 2040 UTC. The locations of all gridpoints with a vertical velocity in the top 50% of all updrafts in the downshear quadrants

are displayed in Fig. 53a, and the locations of all gridpoints in the top 25% are displayed in Fig. 53b. The respective vertical velocity thresholds are 2.43 m s^{-1} and 4.08 m s^{-1}. The 2D-histograms both show a diagonal pattern, which is consistent with an eyewall sloping outward with height. The top 25% shows a narrower distribution than the top 50%, and its frequency of occurrence of high vertical velocities increases with height. Moreover, the higher vertical velocities (top 25%) are located slightly farther inward than the medium vertical velocities (top 50%), as the dashed diagonal line indicates. This line was placed such that it reflects the mean radial location of the strong vertical updrafts (Fig. 53b), and was added to all other sub-plots for reference. The locations of gridpoints with high temperature perturbations are shown in Figures 53c and 53d, with Fig. 53c representing the locations of all gridpoints exceeding an unbalanced θ'_ρ value of 0.83 K, and Fig. 53d representing the locations of all gridpoints exceeding 1.50 K. Both histograms show a similar pattern, with most higher temperature anomalies located at inner radii inside the strongest updrafts, and outside some higher values at lower and upper levels, with a relative minimum at midlevels around 4 to 6 km height and 30 km radius. Combining thresholding on vertical velocity and temperature anomaly highlights the locations that are both positively buoyant and have a strong upward motion (Fig. 53e, 53f). These plots show that this combination doesn't occur frequently, it is mostly limited to upper levels and to some degree to the slanted path of the eyewall. In summary, the histograms show that the highest vertical velocities occur within the slanted eyewall, the highest temperature anomalies occur more preferably at smaller radii, and gridpoints with both high vertical velocities and high temperature anomalies occur relatively infrequently.

The occurrence of positive temperature anomalies and upward vertical velocities don't have to be collocated to be linked though. Air parcels with negligible vertical velocities might encounter regions with enhanced temperature anomalies at lower levels, be accelerated upwards by them, and then show increased vertical velocities later on. Results from trajectory analysis of high-resolution simulations (e.g. Braun, 2002, Hazelton, 2016) suggest that one forcing mechanism for convective bursts in the eyewall is buoyancy through exchange of air between the eye and eyewall.

Another approach to analyze the importance of the buoyancy for eyewall convection is to investigate the correlation between vertical acceleration and its two forcing terms, buoyancy and vertical perturbation pressure gradient force (equation 15). This equation is part of the retrieval and thus has been used to obtain the temperature and pressure fields that are now being evaluated. However, the retrieval has been tested with and without including the ver-

Table 5: *R^2 values characterizing the relation between vertical acceleration and thermodynamic/dynamic forcing in the vertical momentum equation for each of the four periods. The R^2 values are computed separately for wavenumbers 0-and-1 (Wnrs 0&1), and wavenumbers-2 and higher (Wnr >=2).*

	2040 UTC	2110 UTC	2140 UTC	2210 UTC
Wnrs 0&1, Dynamic	0.03	0.00	0.01	0.01
Wnrs 0&1, Thermodynamic	0.01	0.00	0.03	0.00
Wnr >=2, Dynamic	0.15	0.20	0.03	0.26
Wnr >=2, Thermodynamic	0.39	0.59	0.25	0.47

tical momentum equation, and no notable differences in the retrieved fields have been found. Hence, it is argued that the impact of the vertical momentum equation on the retrieved fields is small and that it is valid to use the vertical momentum equation as a diagnostic tool. The correlation between the vertical acceleration (left-hand side of equation 15) and the dynamic ($-\frac{\partial \pi'}{\partial z}$) and thermodynamic ($\frac{g}{c_p \bar{\theta}_\rho^2}\theta'_\rho$) forcing, respectively, is expressed in terms of coefficients of determination, called R^2 values. The R^2 values indicate the percentage of variance explained by the dependent variables. Vertical acceleration, dynamic forcing, and thermodynamic forcing were first computed and then decomposed into wavenumbers. The R^2 values for different wavenumbers in each individual period are summarized in Table 5, and scatter plots for all four periods combined are shown in Fig. 54.

The scatter plots for wavenumber 0-and-1 show that while both forcing terms have non-zero values, the vertical acceleration is very close to zero. This is reflected in R^2 values which are very close or equal to zero, and supports the interpretation of a quasi-balanced wavenumber-1 pattern, with negligible vertical acceleration and a balance between thermodynamic and dynamic forcings. The scatter plots for wavenumber 2-and-higher show non-zero values for vertical acceleration, dynamic, and thermodynamic forcing. The spread is large, but correlations between vertical acceleration and the forcing terms can be seen. The correlation between vertical acceleration and buoyancy is positive, whereas the correlation between vertical acceleration and vertical perturbation pressure gradient force is negative. The R^2 values for the dynamic forcing term are on the order of 0.2, and are as high as 0.59 for the thermodynamic forcing term. This indicates that vertical accelerations in convection are correlated with the higher-order wavenumber thermodynamic structure. The positive correlation of vertical acceleration to the thermodynamic forcing term and higher explanation of variance suggests that the thermodynamic forcing has a more direct impact on eyewall convection than the dynamic forcing. The negative correlation of vertical acceleration to the

dynamic forcing term and lower explanation of variance suggests that thermodynamic and dynamic forcing may counteract each other.

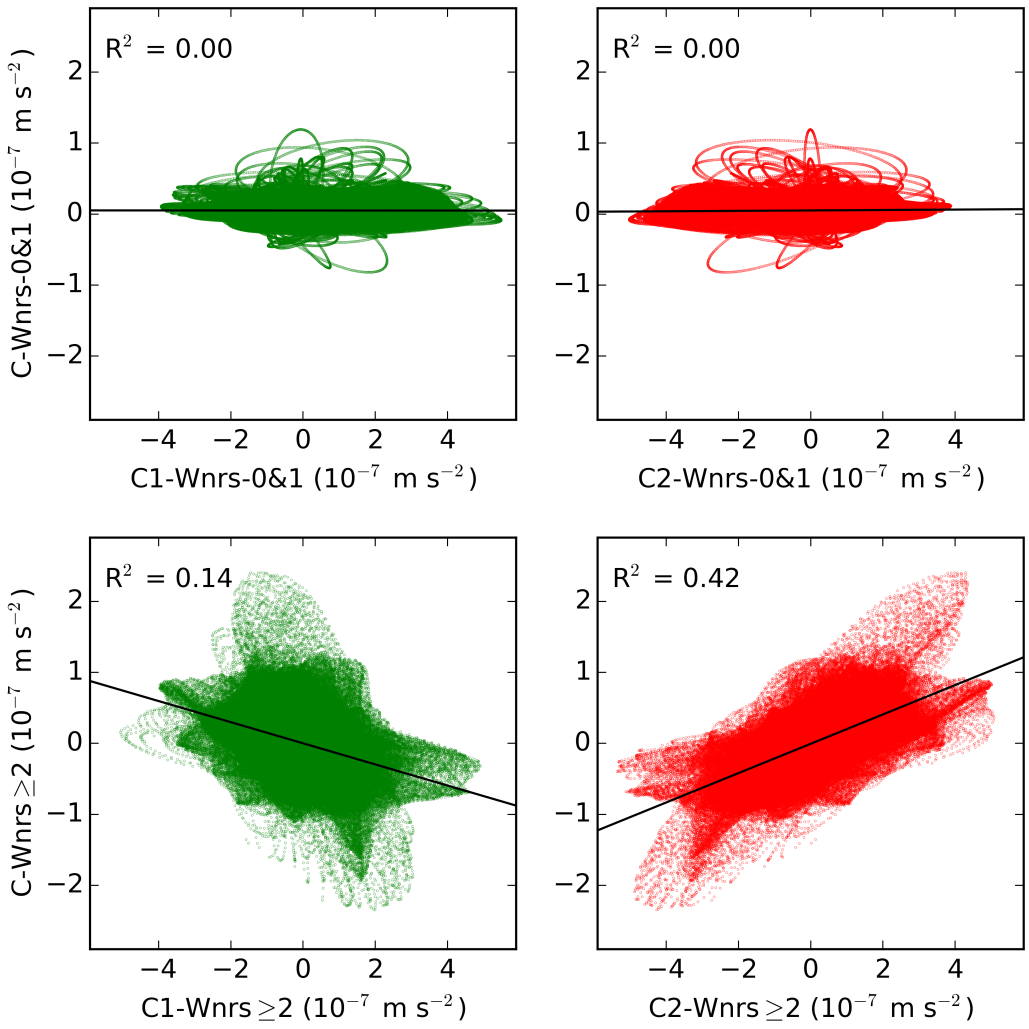

Figure 54: *Scatter plots of vertical acceleration (C), dynamic forcing (C1), and thermodynamic forcing (C2) for wavennumbers 0-and-1, and wavenumbers 2-and-higher. The scatter plots contain data of the eyewall region (15 km $\leq r \leq$ 40 km, 2 km $\leq z \leq$ 8 km) of all four periods.*

5 Summary and Conclusions

Investigating the physical mechanisms that force and shape eyewall convection is essential to better understand the impacts of the eyewall convection on the storm scale and to estimate how changes in environmental forcing will alter the eyewall convection. Kinematic and thermodynamic observations within the eyewall are critical to identify these physical mechanisms. However, high resolution observations in this region are limited. They are limited temporally to periods when reconnaissance or research aircraft sample the storm, and limited spatially to aircraft tracks, dropsonde paths and scanning geometries of remote sensing instruments. Here I present a thermodynamic retrieval tailored specifically toward rapidly rotating vortices, which provides estimates of the pressure and temperature fields within the inner core region of tropical cyclones using airborne Doppler radar data. The retrieval is applied to observations in Hurricane Rita collected on 23 September 2005 during the RAINEX field campaign. The retrieved pressure and temperature fields along with the wind and precipitation structure of Hurricane Rita emphasize the impact of vertical wind shear on the azimuthal location of convection in the eyewall. The pressure and temperature fields show the dynamic and thermodynamic processes that act to balance the vortex tilt. Analysis of the contributions of the retrieved pressure and temperature fields to different azimuthal wavenumbers suggests the interpretation of eyewall convection within a three-level framework of balanced, quasibalanced, and unbalanced motions.

The thermodynamic retrieval introduced here is a modification and combination of previous work done by Gal-Chen, Roux and Viltard, and Liou (e.g. Gal-Chen, 1978, Roux, 1985, Viltard and Roux, 1998, Roux et al., 1993, Liou, 2001, Liou et al., 2003). Gal-Chen proposed the approach of using the momentum equations to derive temperature and pressure from the wind field. Roux suggested to combine the derivatives of the horizontal and vertical momentum equations to eliminate the pressure perturbation terms and obtain equations with only temperature perturbation terms, which proved to be instrumental to retrieve the temperature anomalies in our case. Liou introduced a global approach to the problem, solving the thermodynamic retrieval by minimizing a cost function for the entire domain. Our retrieval combines these three approaches and adds an additional component to account for the hurricane environment. The reference state changes with radius and height, as was suggested by Smith et al. (2005). Moreover, the technical implementation differs from previous methods. Similar to the approach taken in SAMURAI, the retrieval minimizes a cost function using a Galerkin approach, with cubic B-spline finite elements as a basis. This allows one to specify gradients of observations directly and connects the vertical levels

effectively. The retrieval performs slightly better for pressure than for temperature, with RMSE values of 0.4 hPa and 0.7 K, respectively. The performance is higher in regions with higher velocities such as the eyewall and lower in regions with lower velocities. While the inclusion of the time tendency terms in the retrieval equations would be desirable, it is not possible to compute them from observational data. Fortunately, sensitivity tests show that omitting the tendency terms only marginally affects the quality of the retrieval performance.

In order to investigate the storm's thermodynamic structure and the dynamic and thermodynamic mechanisms shaping the eyewall convection, the thermodynamic retrieval is applied to RAINEX observations of Hurricane Rita collected on 23 September 2005. At the time of observation, Rita had weakened to a Category-3 hurricane due to its exposure to increased vertical wind shear, cooler sea surface temperatures, and structural changes that had occurred on the previous day. Four consecutive 30-min intervals of data paint a very consistent picture of the main kinematic and thermodynamic features of the eyewall. During all four periods, tilt and shear are approximately perpendicular to the storm motion and the tilt is in the downshear direction, which is in contrast to other studies where the tilt direction was found to be closer to the left-of-shear direction. Vertical motion and precipitation structure show a pronounced wavenumber-1 pattern in all cases, with highest radar reflectivities and strongest upward motion in the northern semicircle, which roughly corresponds to the downshear quadrants.

The 2-D axisymmetric tangential wind fields from the center out to 60 km radius are balanced by a pressure deficit of approximately 26 hPa and a temperature increase of approximately 4 K. The pressure deficit is maximized at low levels, while the temperature increase is maximized at vertical levels of 6 to 9 km. This axisymmetric mean temperature and pressure field represents the balanced reference state.

The pressure and temperature fields obtained by the thermodynamic retrieval show pronounced wavenumber-1 patterns. The patterns are very consistent over all four periods, bolstering the confidence in the retrieval and suggesting a connection between the thermodynamic structure of the vortex and the environmental wind shear. The thermal anomalies show an anticyclonic rotation with height, with negative values in the northern part of the eyewall at low levels and negative values in the eastern part of the eyewall at upper levels. Hence, the cold anomalies are located in the downshear/downtilt direction and are collocated with regions of strong convection. Jones (1995) identified this thermal couplet with cool anomalies downtilt and warm anomalies uptilt as the adiabatic response of the vortex to shear. The shear introduces a tilt of the vortex and the tilt introduces adiabatic ascent right-

of-tilt and adiabatic descent left-of-tilt, resulting in raised isentropes and thus cold anomalies downtilt and lowered isentropes and thus warm anomalies uptilt. This wavenumber-1 in vertical motion and temperature acts to balance the tilt and thus keep the vortex close to alignment and in a quasi-steady state. Hence, the combination of balanced state and wavenumber-1 will be called the quasi-balanced reference state in our three-level framework. The anticyclonic rotation of the thermal anomalies with height is similar to results of Jones (2000). She also found an anticyclonic rotation with height in her simulations of baroclinic vortices and attributed it to the anticyclonic rotation of the tilt with height, emphasizing the close connection between the orientation of the thermal couplet and the tilt direction. While the first of our four periods also shows an anticyclonic rotation of the tilt with height, the relationship is less clear for the other three periods. The wavenumber-1 pressure anomalies show a cyclonic rotation with height, with high pressure anomalies to the north of the center at low levels and high pressure anomalies to the west of the center at upper levels. Hence, the high pressure anomalies are located predominantly left-of-shear/left-of-tilt, with low-level storm-relative inflow and upper-level storm-relative outflow to the east of the center, and a reverse flow pattern to the west of the center. The pressure perturbation distribution results in an upward-directed pressure gradient force at upper levels in the upshear-right quadrant, at all vertical levels in the downshear-right quadrant, and at low levels in the downshear-left quadrant. In contrast, it results in a downward-directed pressure gradient force at upper levels in the downshear-left quadrant, at all vertical levels in the upshear-left quadrant, and at low levels in the upshear-right quadrant.

The power spectrum of the pressure perturbation field shows that the wavenumber-1 component contains the most power, and moreover that there is also a non-negligible amount of power in wavenumber-2. The wavenumber-2 pressure anomalies show a consistent pattern for all periods and vertical levels, with positive perturbations to the north and south of the center, and negative perturbations to the east and west of the center. In many cases this pressure perturbation pattern is accompanied by a wavenumber-2 flow field in the horizontal and vertical, with enhanced vertical motion toward the inner edge of the eyewall in the eastern and western part of the eyewall, and a deformation field in the horizontal, with inflow toward the southeast and northwest and outflow toward the northeast and southwest. Wavenumber-2 pressure anomalies have previously been linked to vortex Rossby waves. If the pressure pattern of Rita was caused by a wavenumber-2 vortex Rossby wave, the anomalies should move at half the advective speed, and thus rotate about 90° between periods. The stationary nature of the pressure and the flow field suggest that vortex Rossby waves are not the cause for the wavenumber-2 pattern in the present study. Deformation flow

patterns in tropical cyclones have been mentioned in previous literature in the context of elliptical eyewalls (Yamauchi et al., 2002), and in the context of environmental deformation flow patterns (Braun, 2002). Another possible mechanism to create a wavenumber-2 would be the superposition of two perpendicular wavenumber-1 patterns. Storm motion and tilt direction are oriented perpendicular in the case of Rita. If and how the interaction of storm motion and tilt can result in a wavenumber-2 flow field is unclear, however, and would be an interesting topic for future research. Further investigation is needed to determine which of the mechanisms is responsible for the wavenumber-2 pattern.

Individual convective cells embedded in the eyewall have been regarded to play an integral role in eyewall dynamics ("hot towers", Malkus and Riehl (1960), Hendricks et al. (2004)) and their location has been linked to intensity change efficiency (Pendergrass and Willoughby, 2009, Vigh and Schubert, 2009). Individual convective cells project onto higher-order wavenumbers. The temporal resolution of 30 minutes between our radar analyses precludes a detailed analysis of the thermodynamic structure of individual updrafts and might result in dealiasing into lower wavenumbers. Nevertheless, statistical analysis of the higher-wavenumber structure of convective updrafts suggests that while "stronger updrafts are more likely to be buoyant" the opposite conclusion that "more buoyant parcels have higher vertical velocities" is not supported by our analysis. This highlights the difference between vertical motion and vertical acceleration, and the necessity to analyze the effects of buoyancy on an air parcel along a parcel trajectory rather than instantaneously.

Correlations between vertical acceleration and dynamic and thermodynamic forcing, respectively, suggest that vertical accelerations are due to higher-order wavenumbers and that the thermodynamic forcing dominates the dynamic forcing. Wavenumbers-0 and -1 of the vertical acceleration show very small acceleration values and no correlation to the forcing terms, indicating that these lower wavenumbers are near hydrostatic balance or "quasi-balanced", suggesting that the the forcing of the individual convective elements should be studied with respect to a quasi-balanced reference state. Higher wavenumbers of vertical acceleration show non-zero values and a correlation to both forcing terms, where the correlation to the thermodynamic forcing is stronger and positive and the correlation to the dynamic forcing term is weaker and negative. This indicates that the vertical acceleration of individual convective air parcels in the eyewall is linked to thermal forcing, and that thermodynamic and dynamics effects tend to counteract each other.

In summary, the radar-derived kinematic and thermodynamic structure of Hurricane Rita on 23 September 2005 enabled a very detailed analysis of the thermodynamic and dynamic

forcing of eyewall convection. The structure can be best described in terms of a three-level framework of balanced, quasi-balanced and unbalanced motions. The axisymmetric (wavenumber-0) structure is determined by a primary force *balance* between the gravitational force and the vertical pressure gradient force in the vertical, and the horizontal pressure gradient force, Coriolis force, and centrifugal force in the horizontal, resulting in a pressure drop and temperature increase toward the center. The wavenumber-1 structure, and maybe in part the wavenumber-2 structure, is determined by the interaction of the storm with environmental vertical wind shear, resulting in a *quasi-balance* between shear and shear-induced kinematic and thermodynamic anomalies. The higher-order wavenumbers are connected to *unbalanced* motions and convective cells within the eyewall.

One limitation of this study is that the retrieval solves for density potential temperature, and not separately for temperature, humidity and water loading. Using density potential temperature is an advantage for the retrieval itself, because it reduces the number of retrieval equations and it avoids the necessity to make assumptions on the microphysical state of the eyewall convection prior to performing the retrieval. However, it complicates the interpretation of the results in terms of separating adiabatic and diabatic contributions, because the density potential temperature is a combination of temperature, humidity, and water loading. The radar reflectivity distribution could be used to get a rough estimate on the amount of water loading, but disentangling the respective contributions of temperature, humidity and water loading to the density potential temperature will nevertheless be challenging, especially since the importance of water loading is expected to change throughout the lifecycle of an individual convective cell. Polarimetric radar data could aid to improve the estimate of water loading by providing additional information about the type and mass of the hydrometeors.

Future work, such as applying the retrieval to other datasets and analyzing the thermodynamic structure of tropical cyclones at different stages of their lifecycle or while being impacted by different environmental conditions will help to improve the understanding of the physical mechanisms that determine the activity and organization of eyewall convection. Analysis of the respective importance of the thermodynamic and dynamic forcing terms during those different scenarios should lead to a better understanding of how eyewall convection contributes to tropical cyclone intensity change.

Appendix A Automated Radar Data Quality Control

The following commands are executed in the SOLO Editor to remove non-weather echoes from tail Doppler radar data. The script expects Dorade sweepfiles containing radar reflectivity (ZZ), aircraft-motion-removed radial velocity (VV), and spectrum width (SPEC_WDT). The quality-controlled fields are saved as DBZ (radar reflectivity) and VG (radial velocity):

a-speckle is 5 gates
optimal-beamwidth is 3. degrees
freckle-threshold is 20.
freckle-average is 5 gates
BB-max-neg-folds is 4
BB-max-pos-folds is 4
BB-use-ac-wind
BB-gates-averaged is 15 gates
! for-each-ray
copy ZZ to DBZ
copy VV to VG
remove-ring in VG from 0. to 0.5 km.
remove-ring in VG from 70. to 75. km.
remove-only-surface in VG
clear-bad-flags
set-bad-flags when SPEC_WDT above 4.
and-bad-flags when DBZ below 0.
assert-bad-flags in VG
despeckle VG
copy VG to V1
clear-bad-flags
BB-unfolding of VG
flag-freckles in VG
assert-bad-flags in VG
despeckle VG
clear-bad-flags
copy-bad-flags from VG
assert-bad-flags in DBZ

Appendix B SAMURAI Configuration

The SAMURAI configuration is specified using an xml-file. The settings used for the SAMURAI analyses of Hurricane Rita (2005) are:

```
<?xml version="1.0" encoding="UTF-8"?>
<samurai xmlns = 'http://www.hawaii.edu/ns/samurai'>
<grid>
<i_min>-75.</i_min>
<i_max>75.</i_max>
<i_incr>1.0</i_incr>
<j_min>-75.</j_min>
<j_max>75.</j_max>
<j_incr>1.0</j_incr>
<k_min>0.</k_min>
<k_max>15.0</k_max>
<k_incr>0.5</k_incr>
</grid>
<operation>
<mode>XYZ</mode>
<data_directory>vardata</data_directory>
<output_directory>output_shifted</output_directory>
<load_background>false</load_background>
<adjust_background>false</adjust_background>
<preprocess_obs>true</preprocess_obs>
<num_iterations>2</num_iterations>
<output_mish>false</output_mish>
<output_txt>true</output_txt>
<output_qc>true</output_qc>
<output_netcdf>true</output_netcdf>
<output_asi>false</output_asi>
</operation>
<background>
```

<ref_state>dunion_mt.snd</ref_state>
<ref_time>21:10:00</ref_time>
<i_background_roi>25.</i_background_roi>
<j_background_roi>25.</j_background_roi>
</background>
<radar>
<radar_skip>1</radar_skip>
<radar_stride>2</radar_stride>
<dynamic_stride>0</dynamic_stride>
<qr_variable>dbz</qr_variable>
<i_reflectivity_roi>1.0</i_reflectivity_roi>
<j_reflectivity_roi>1.0</j_reflectivity_roi>
<k_reflectivity_roi>1.0</k_reflectivity_roi>
<dbz_pseudow_weight>1.0</dbz_pseudow_weight>
<radar_dbz>DBZ</radar_dbz>
<radar_vel>VG</radar_vel>
<radar_sw>SW</radar_sw>
<mask_reflectivity>-10</mask_reflectivity>
<melting_zone_width>1.0</melting_zone_width>
<mixed_phase_dbz>20.0</mixed_phase_dbz>
<rain_dbz>30.0</rain_dbz>
</radar>
<parameters iter="1">
<bg_rhou_error>20.0</bg_rhou_error>
<bg_rhov_error>20.0</bg_rhov_error>
<bg_rhow_error>20.0</bg_rhow_error>
<bg_tempk_error>5.0</bg_tempk_error>
<bg_qv_error>5.0</bg_qv_error>
<bg_rhoa_error>5.0</bg_rhoa_error>
<bg_qr_error>3.0</bg_qr_error>
<mc_weight>1.0</mc_weight>
<i_filter_length>4.0</i_filter_length>
<j_filter_length>4.0</j_filter_length>
<k_filter_length>4.0</k_filter_length>
<i_spline_cutoff>10.0</i_spline_cutoff>

<j_spline_cutoff>10.0</j_spline_cutoff>
<k_spline_cutoff>10.0</k_spline_cutoff>
<i_max_wavenumber>-1.0</i_max_wavenumber>
<j_max_wavenumber>-1.0</j_max_wavenumber>
<k_max_wavenumber>-1.0</k_max_wavenumber>
</parameters>
<parameters iter="2">
<bg_rhou_error>1.0</bg_rhou_error>
<bg_rhov_error>1.0</bg_rhov_error>
<bg_rhow_error>1.0</bg_rhow_error>
<bg_tempk_error>1.0</bg_tempk_error>
<bg_qv_error>1.0</bg_qv_error>
<bg_rhoa_error>1.0</bg_rhoa_error>
<bg_qr_error>1.0</bg_qr_error>
<mc_weight>1.</mc_weight>
<i_filter_length>2.0</i_filter_length>
<j_filter_length>2.0</j_filter_length>
<k_filter_length>2.0</k_filter_length>
<i_spline_cutoff>5.0</i_spline_cutoff>
<j_spline_cutoff>5.0</j_spline_cutoff>
<k_spline_cutoff>5.0</k_spline_cutoff>
<i_max_wavenumber>-1.0</i_max_wavenumber>
<j_max_wavenumber>-1.0</j_max_wavenumber>
<k_max_wavenumber>-1.0</k_max_wavenumber>
</parameters>
<boundary_conditions>
<i_rhou_bcL>R1T2</i_rhou_bcL>
<i_rhou_bcR>R1T2</i_rhou_bcR>
<i_rhov_bcL>R1T2</i_rhov_bcL>
<i_rhov_bcR>R1T2</i_rhov_bcR>
<i_rhow_bcL>R1T2</i_rhow_bcL>
<i_rhow_bcR>R1T2</i_rhow_bcR>
<i_tempk_bcL>R1T2</i_tempk_bcL>
<i_tempk_bcR>R1T2</i_tempk_bcR>
<i_qv_bcL>R1T2</i_qv_bcL>

<i_qv_bcR>R1T2</i_qv_bcR>
<i_rhoa_bcL>R1T2</i_rhoa_bcL>
<i_rhoa_bcR>R1T2</i_rhoa_bcR>
<i_qr_bcL>R1T2</i_qr_bcL>
<i_qr_bcR>R1T2</i_qr_bcR>
<j_rhou_bcL>R1T2</j_rhou_bcL>
<j_rhou_bcR>R1T2</j_rhou_bcR>
<j_rhov_bcL>R1T2</j_rhov_bcL>
<j_rhov_bcR>R1T2</j_rhov_bcR>
<j_rhow_bcL>R1T2</j_rhow_bcL>
<j_rhow_bcR>R1T2</j_rhow_bcR>
<j_tempk_bcL>R1T2</j_tempk_bcL>
<j_tempk_bcR>R1T2</j_tempk_bcR>
<j_qv_bcL>R1T2</j_qv_bcL>
<j_qv_bcR>R1T2</j_qv_bcR>
<j_rhoa_bcL>R1T2</j_rhoa_bcL>
<j_rhoa_bcR>R1T2</j_rhoa_bcR>
<j_qr_bcL>R1T2</j_qr_bcL>
<j_qr_bcR>R1T2</j_qr_bcR>
<k_rhou_bcL>R1T2</k_rhou_bcL>
<k_rhou_bcR>R1T2</k_rhou_bcR>
<k_rhov_bcL>R1T2</k_rhov_bcL>
<k_rhov_bcR>R1T2</k_rhov_bcR>
<k_rhow_bcL>R1T0</k_rhow_bcL>
<k_rhow_bcR>R1T0</k_rhow_bcR>
<k_tempk_bcL>R1T2</k_tempk_bcL>
<k_tempk_bcR>R1T2</k_tempk_bcR>
<k_qv_bcL>R1T2</k_qv_bcL>
<k_qv_bcR>R1T2</k_qv_bcR>
<k_rhoa_bcL>R1T2</k_rhoa_bcL>
<k_rhoa_bcR>R1T2</k_rhoa_bcR>
<k_qr_bcL>R1T2</k_qr_bcL>
<k_qr_bcR>R1T2</k_qr_bcR>
</boundary_conditions>
<observation_errors>

<dropsonde_rhou_error>2.0</dropsonde_rhou_error>
<dropsonde_rhov_error>2.0</dropsonde_rhov_error>
<dropsonde_rhow_error>50.0</dropsonde_rhow_error>
<dropsonde_tempk_error>1.0</dropsonde_tempk_error>
<dropsonde_qv_error>0.5</dropsonde_qv_error>
<dropsonde_rhoa_error>1.0</dropsonde_rhoa_error>
<flightlevel_rhou_error>2.0</flightlevel_rhou_error>
<flightlevel_rhov_error>2.0</flightlevel_rhov_error>
<flightlevel_rhow_error>5.0</flightlevel_rhow_error>
<flightlevel_tempk_error>1.0</flightlevel_tempk_error>
<flightlevel_qv_error>0.5</flightlevel_qv_error>
<flightlevel_rhoa_error>1.0</flightlevel_rhoa_error>
<insitu_rhou_error>1.0</insitu_rhou_error>
<insitu_rhov_error>1.0</insitu_rhov_error>
<insitu_rhow_error>2.0</insitu_rhow_error>
<insitu_tempk_error>1.0</insitu_tempk_error>
<insitu_qv_error>0.5</insitu_qv_error>
<insitu_rhoa_error>1.0</insitu_rhoa_error>
<sfmr_windspeed_error>10.0</sfmr_windspeed_error>
<qscat_rhou_error>2.5</qscat_rhou_error>
<qscat_rhov_error>2.5</qscat_rhov_error>
<ascat_rhou_error>2.5</ascat_rhou_error>
<ascat_rhov_error>2.5</ascat_rhov_error>
<amv_rhou_error>10.0</amv_rhou_error>
<amv_rhov_error>10.0</amv_rhov_error>
<lidar_sw_error>1.0</lidar_sw_error>
<lidar_power_error>50.0</lidar_power_error>
<lidar_min_error>1.0</lidar_min_error>
<radar_sw_error>1.0</radar_sw_error>
<radar_fallspeed_error>2.0</radar_fallspeed_error>
<radar_min_error>1.0</radar_min_error>
</observation_errors>
<options>
<max_radar_elevation>45.0</max_radar_elevation>
<horizontal_radar_appx>true</horizontal_radar_appx>

<allow_background_missing_values>true</allow_background_missing_values>
</options>
</samurai>

Appendix C Thermodynamic Retrieval Configuration

Similar to the SAMURAI configuration, the thermodynamic retrieval configuration is specified using an xml-file:

<?xml version="1.0" encoding="UTF-8"?>
<samurai xmlns = 'http://www.hawaii.edu/ns/samurai'>
<grid>
<i_min>-60.</i_min>
<i_max>60.</i_max>
<i_incr>1.0</i_incr>
<j_min>-60.</j_min>
<j_max>60.</j_max>
<j_incr>1.0</j_incr>
<k_min>0.0</k_min>
<k_max>15.0</k_max>
<k_incr>0.5</k_incr>
</grid>
<operation>
<mode>XYZ</mode>
<data_directory>vardata</data_directory>
<output_directory>output_shifted</output_directory>
<load_background>false</load_background>
<adjust_background>false</adjust_background>
<preprocess_obs>true</preprocess_obs>
<num_iterations>1</num_iterations>
<output_mish>false</output_mish>
<output_txt>false</output_txt>
<output_qc>true</output_qc>
<output_netcdf>true</output_netcdf>

<output_asi>false</output_asi>
</operation>
<background>
<ref_state>dunion_mt.snd</ref_state>
<ref_time>21:10:00</ref_time>
<i_background_roi>2.</i_background_roi>
<j_background_roi>2.</j_background_roi>
</background>
<radar>
<qr_variable>dbz</qr_variable>
<dbz_pseudow_weight>0.0</dbz_pseudow_weight>
<mask_reflectivity>None</mask_reflectivity>
</radar>
<parameters iter="1">
<i_filter_length>4.0</i_filter_length>
<j_filter_length>4.0</j_filter_length>
<k_filter_length>2.0</k_filter_length>
<i_spline_cutoff>10.0</i_spline_cutoff>
<j_spline_cutoff>10.0</j_spline_cutoff>
<k_spline_cutoff>2.0</k_spline_cutoff>
<i_max_wavenumber_rhou>-1.0</i_max_wavenumber_rhou>
<j_max_wavenumber_rhou>-1.0</j_max_wavenumber_rhou>
<i_max_wavenumber_rhov>-1.0</i_max_wavenumber_rhov>
<j_max_wavenumber_rhov>-1.0</j_max_wavenumber_rhov>
<i_max_wavenumber_rhow>0.0</i_max_wavenumber_rhow>
<j_max_wavenumber_rhow>0.0</j_max_wavenumber_rhow>
<i_max_wavenumber>-1.0</i_max_wavenumber>
<j_max_wavenumber>-1.0</j_max_wavenumber>
<k_max_wavenumber>-1.0</k_max_wavenumber>
<mc_weight>0.0</mc_weight>
</parameters>
<options>
<spline_approximation>2</spline_approximation>
</options>
<thermo>

<infile>20050923_leg6_shifted_2110.nc</infile>
<infile_idim>121</infile_idim>
<infile_jdim>121</infile_jdim>
<infile_kdim>31</infile_kdim>
<thermo_A_error>0.01</thermo_A_error>
<thermo_B_error>0.01</thermo_B_error>
<thermo_C_error>0.01</thermo_C_error>
<thermo_D_error>0.01</thermo_D_error>
<thermo_E_error>0.01</thermo_E_error>
<bg_pip_error>10.0</bg_pip_error>
<bg_thetarhop_error>10.0</bg_thetarhop_error>
<bg_ftheta_error>10.0</bg_ftheta_error>
<i_pip_bcL>R0</i_pip_bcL>
<i_pip_bcR>R0</i_pip_bcR>
<i_thetarhop_bcL>R0</i_thetarhop_bcL>
<i_thetarhop_bcR>R0</i_thetarhop_bcR>
<i_ftheta_bcL>R0</i_ftheta_bcL>
<i_ftheta_bcR>R0</i_ftheta_bcR>
<j_pip_bcL>R0</j_pip_bcL>
<j_pip_bcR>R0</j_pip_bcR>
<j_thetarhop_bcL>R0</j_thetarhop_bcL>
<j_thetarhop_bcR>R0</j_thetarhop_bcR>
<j_ftheta_bcL>R0</j_ftheta_bcL>
<j_ftheta_bcR>R0</j_ftheta_bcR>
<k_pip_bcL>R0</k_pip_bcL>
<k_pip_bcR>R0</k_pip_bcR>
<k_thetarhop_bcL>R0</k_thetarhop_bcL>
<k_thetarhop_bcR>R0</k_thetarhop_bcR>
<k_ftheta_bcL>R0</k_ftheta_bcL>
<k_ftheta_bcR>R0</k_ftheta_bcR>
</thermo>
</samurai>

References

Bargen, D. W. and R. C. Brown, 1980: Interactive radar velocity unfolding. *Preprints, 19th Radar Meteor. Conf., 9-13 Sept. 1997*, Amer. Meteor. Soc.

Bell, M. M., W.-C. Lee, C. A. Wolff, and H. Cai, 2013: A Solo-Based Automated Quality Control Algorithm for Airborne Tail Doppler Radar Data. *J. Appl. Meteor. Climatol.*, **52**, 2509–2528.

Bell, M. M., M. T. Montgomery, and K. A. Emanuel, 2012a: Air-Sea Enthalpy and Momentum Exchange at Major Hurricane Wind Speeds Observed during CBLAST. *J. Atmos. Sci.*, **69**, 3197–3222.

Bell, M. M., M. T. Montgomery, and W. C. Lee, 2012b: An Axisymmetric View of Concentric Eyewall Evolution in Hurricane Rita (2005). *J. Atmos. Sci.*, **69**, 2414–2432.

Black, M. L., J. F. Gamache, F. D. Marks, C. E. Samsury, and H. E. Willoughby, 2002: Eastern Pacific Hurricanes Jimena of 1991 and Olivia of 1994: The Effect of Vertical Shear on Structure and Intensity. *Mon. Wea. Rev.*, **130**, 2291–2312.

Bosart, B. L., W.-C. Lee, and R. M. Wakimoto, 2002: Procedures to Improve the Accuracy of Airborne Doppler Radar Data. *J. Atmos. Oceanic Technol.*, **19**, 322–339.

Braun, S. A., 2002: A cloud-resolving simulation of Hurricane Bob (1991): Storm Structure and Eyewall Buoyancy. *Mon. Wea. Rev.*, **130**, 1573–1592.

Braun, S. A., M. T. Montgomery, and Z. Pu, 2006: High-Resolution Simulation of Hurricane Bonnie (1998). Part I: The Organization of Eyewall Vertical Motion. *J. Atmos. Sci.*, **63**, 19–42.

Braun, S. A. and L. Wu, 2007: A Numerical Study of Hurricane Erin (2001). Part II: Shear and the Organization of Eyewall Vertical Motion. *Mon. Wea. Rev.*, **135**, 1179–1194.

Cai, H., W.-C. Lee, M. M. Bell, C. A. Wolff, X. Tang, and F. Roux, 2015: A Generalized Navigation Correction Method for Airborne Doppler Radar Data. *Preprints, 37th Conference on Radar Meteorology, 14 - 18 September 2015*, Norman, OK, Amer. Meteor. Soc.

Corbosiero, K. L. and J. Molinari, 2002: The Effects of Vertical Wind Shear on the Distribution of Convection in Tropical Cyclones. *Mon. Wea. Rev.*, **130**, 2110–2123.

Corbosiero, K. L. and J. Molinari, 2003: The Relationship between Storm Motion, Vertical Wind Shear, and Convective Asymmetries in Tropical Cyclones. *Mon. Wea. Rev.*, **60**, 366–376.

Davis, C., et al., 2008: Prediction of Landfalling Hurricanes with the Advanced Hurricane WRF Model. *Mon. Wea. Rev.*, **136**, 1990–2005.

DeHart, J., R. A. Houze, Jr., and R. F. Rogers, 2014: Quadrant Distribution of Tropical Cyclone Inner-Core Kinematics in Relation to Environmental Shear. *J. Atmos. Sci.*, **71**, 2713–2732.

DeMaria, M. and J. Kaplan, 1994: A Statistical Hurricane Intensity Prediction Scheme (SHIPS) for the Atlantic Basin. *Wea. Forecasting*, **9**, 209–220.

Didlake, A. C., Jr. and R. A. Houze, Jr., 2011: Kinematics of the Secondary Eyewall Observed in Hurricane Rita (2005). *J. Atmos. Sci.*, **68**, 1620–1636.

Didlake, A. C., Jr. and R. A. Houze, Jr., 2013a: Convective-Scale Variations in the Inner-Core Rainbands of a Tropical Cyclone. *J. Atmos. Sci.*, **70**, 504–523.

Didlake, A. C., Jr. and R. A. Houze, Jr., 2013b: Dynamics of the Stratiform Sector of a Tropical Cyclone Rainband. *J. Atmos. Sci.*, **70**, 1891–1911.

Dudhia, J., 1989: Numerical Study of Convection Observed During Winter Monsoon Experiment Using a Mesoscale Two-Dimensional Model. *J. Atmos. Sci.*, **46**, 3077–3107.

Eastin, M. D., W. M. Gray, and P. G. Black, 2005: Buoyancy of Convective Vertical Motions in the Inner Core of Intense Hurricanes. Part I: General Statistics. *Mon. Wea. Rev.*, **133**, 188–208.

Ek, M. B., K. E. Mitchell, Y. Lin, E. Rogers, P. Grunmann, V. Koren, G. Gayno, and J. D. Tarpley, 2003: Implementation of Noah land surface model advances in the National Centers for Environmental Prediction operational mesoscale Eta model. *Journal of Geophysical Research*, **108**, 2156–2202.

Emanuel, K. A., 1995: Sensitivity of tropical cyclones to surface exchange coefficients and a revised steady-state model incorporating eye dynamics. *J. Atmos. Sci.*, **52**, 3969–3976.

Foerster, A. M., M. M. Bell, P. A. Harr, and S. C. Jones, 2014: Observations of the Eyewall Structure of Typhoon Sinlaku (2008) during the Transformation Stage of Extratropical Transition. *Mon. Wea. Rev.*, **142**, 3372–3392.

Frank, W. M. and E. A. Ritchie, 1999: Effects of environmental flow upon tropical cyclone structure. *Mon. Wea. Rev.*, **127**, 2044–2061.

Gal-Chen, T., 1978: A Method for the Initialization of the Anelastic Equations: Implications for Matching Models with Observations. *Mon. Wea. Rev.*, **106**, 587–606.

Gao, J., M. Xue, K. Brewster, and K. K. Droegemeier, 2004: A Three-Dimensional Variational Data Analysis Method with Recursive Filter for Doppler Radars. *J. Atmos. Oceanic Technol.*, **21**, 457–469.

Georgis, J. F., F. Roux, and P. H. Hildebrand, 2000: Observation of Precipitating Systems over Complex Orography with Meteorological Doppler Radars: A Feasibility Study. *Meteorol. Atmos. Phys.*, **72**, 185–202.

Guimond, S. R., M. A. Bourassa, and P. D. Reasor, 2011: A Latent Heat Retrieval and Its Effects on the Intensity and Structure Change of Hurricane Guillermo (1997). Part I: The Algorithm and Observations. *J. Atmos. Sci.*, **68**, 1549–1567.

Hazelton, J. F., 2016: Development and Evolution of Convective Bursts in WRF Simulations of TCs Dean (2007) and Bill (2009). *Preprints, 32nd Conference on Hurricanes and Tropical Meteorology, 17 - 22 April 2016*, San Juan, PR, Amer. Meteor. Soc.

Hence, D. A. and R. A. Houze, Jr., 2011: Vertical structure of hurricane eyewalls as seen by TRMM precipitation radar. *J. Atmos. Sci.*, **68**, 1637–1652.

Hendricks, E. A., M. T. Montgomery, and C. A. Davis, 2004: The Role of "Vortical" Hot Towers in the Formation of Tropical Cyclone Diana (1984). *J. Atmos. Sci.*, **61**, 1209–1232.

Hildebrand, P. H., et al., 1996: The ELDORA/ASTRAIA Airborne Doppler Weather Radar: High-Resolution Observations from TOGA COARE. *Bull. Amer. Meteor. Soc.*, **77**, 213–232.

Hong, S.-Y., Y. Noh, and J. Dudhia, 2006: A New Vertical Diffusion Package With an Explicit Treatment of Entrainment Processes. *Mon. Wea. Rev.*, **134**, 2318–2341.

Houze, R. A., Jr., et al., 2006: The Hurricane Rainband and Intensity Change Experiment: Observations and Modeling of Hurricanes Katrina, Ophelia, and Rita. *Bull. Amer. Meteor. Soc.*, **87**, 1503–1521.

Jones, S. C., 1995: The evolution of vortices in vertical shear. I: Initially barotropic vortices. *Q. J. R. Meteorol. Soc.*, **121**, 821–851.

Jones, S. C., 2000: The evolution of vortices in vertical shear. III: Baroclinic vortices. *Q. J. R. Meteorol. Soc.*, **126**, 3161–3186.

Kain, J. S. and J. M. Fritsch, 1990: A One-Dimensional Entraining Detraining Plume Model and Its Application in Convective Parameterization. *J. Atmos. Sci.*, **47**, 2784–2802.

Knabb, R. D., D. P. Brown, and J. R. Rhome, 2011: Tropical Cyclone Report, Hurricane Rita, 18-26 September 2005. *National Hurricane Center*.

Kuo, H.-C., R. T. Williams, and J.-H. Chen, 1999: A Possible Mechanism for the Eye Rotation of Typhoon Herb. *J. Atmos. Sci.*, **56**, 1659–1673.

Lee, W.-C., P. R. Harasti, M. Bell, B. J. Jou, and M.-H. Chang, 2006: Doppler Velocity Signatures of Idealized Elliptical Vortices. *Terr. Atmos. Ocean. Sci.*, **17**, 429–446.

Liou, Y.-C., 2001: The Derivation of Absolute Potential Temperature Perturbations and Pressure Gradients from Wind Measurements in Three-Dimensional Space. *J. Atmos. Oceanic Technol.*, **18**, 577–590.

Liou, Y.-C., T.-C. C. Wang, and K.-S. Chung, 2003: Three-Dimensional Variational Approach for Deriving the Thermodynamic Structure Using Doppler Wind Observations - An Application to a Subtropical Squall Line. *J. Appl. Meteor.*, **42**, 1443–1454.

Malkus, J. and H. Riehl, 1960: On the dynamics and energy transformations in steady-state hurricanes. *Tellus*, **12**, 1–20.

Marks, F. D., Jr., R. A. Houze, Jr., and J. F. Gamache, 1992: Dual-Aircraft Investigation of the Inner Core of Hurricane Norbert. Part I: Kinematic Structure. *J. Atmos. Sci.*, **49**, 919–942.

Mlawer, E. J., S. J. Taubman, P. D. Brown, M. J. Iacono, and S. A. Clough, 1997: Radiative Transfer for Inhomogeneous Atmospheres: RRTM, a Validated Correlated-k Model for the Longwave. *Journal of Geophysical Research*, **102**, 16 663–16 682.

Montgomery, M. T. and R. J. Kallenbach, 1997: A theory for vortex Rossby-waves and its application to spiral bands and intensity changes in hurricanes. *Q. J. R. Meteorol. Soc.*, **123**, 435–465.

Ooyama, K. V., 2002: The Cubic-Spline Transform Method: Basic Definitions and Tests in a 1D Single Domain. *Mon. Wea. Rev.*, **130**, 2392–2415.

Pendergrass, A. G. and H. E. Willoughby, 2009: Diabatically Induced Secondary Flows in Tropical Cyclones. Part I: Quasi-Steady Forcing. *Mon. Wea. Rev.*, **137**, 805–821, doi: {http://dx.doi.org/10.1175/2008MWR2657.1}.

Purser, R. J., W.-S. Wu, D. F. Parrish, and N. M. Roberts, 2003: Numerical Aspects of the Application of Recursive Filters to Variational Statistical Analysis. Part I: Spatially Homogeneous and Isotropic Gaussian Covariances. *Mon. Wea. Rev.*, **131**, 1524–1535.

Reasor, P. D. and M. D. Eastin, 2012: Rapidly Intensifying Hurricane Guillermo (1997). Part II: Resilience in Shear. *Mon. Wea. Rev.*, **140**, 425–444.

Reasor, P. D., M. T. Montgomery, and L. D. Grasso, 2004: A New Look at the Problem of Tropical Cyclones in Vertical Shear Flow: Vortex Resiliency. *J. Atmos. Sci.*, **61**, 3–22.

Reasor, P. D., R. Rogers, and S. Lorsolo, 2013: Environmental Flow Impacts on Tropical Cyclone Structure Diagnosed from Airborne Doppler Radar Composites. *Mon. Wea. Rev.*, **141**, 2970–2991.

Rogers, R., P. Reasor, and S. Lorsolo, 2013: Airborne Doppler Observations of the Inner-Core Structural Differences between Intensifying and Steady-State Tropical Cyclones. *Mon. Wea. Rev.*, **141**, 2970–2991.

Roux, F., 1985: Retrieval of Thermodynamic Fields from Multiple-Doppler Radar Data Using the Equations of Motion and the Thermodynamic Equation. *Mon. Wea. Rev.*, **113**, 2142–2157.

Roux, F., V. Marecal, and D. Hauser, 1993: The 12/13 January 1988 Narrow Cold-Frontal Rainband Observed during MFDP/FRONTS 87. Part I: Kinematics and Thermodynamics. *J. Atmos. Sci.*, **50**, 951–974.

Smith, R. K., 2006: Accurate determination of a balanced axisymmetric vortex in a compressible atmosphere. *Tellus A*, **58**, 98–103.

Smith, R. K., M. T. Montgomery, and H. Zhu, 2005: Buoyancy in tropical cyclones and other rapidly rotating atmospheric vortices. *Dyns. Atmos. Oceans*, **40**, 189–208.

Testud, J., P. H. Hildebrand, and W.-C. Lee, 1995: A Procedure to Correct Airborne Doppler Radar Data for Navigation Errors Using the Echo Returned from the Earth's Surface. *J. Atmos. Oceanic Technol.*, **12**, 800–820.

Thompson, G. and T. Eidhammer, 2014: A Study of Aerosol Impacts on Clouds and Precipitation Development in a Large Winter Cyclone. *J. Atmos. Sci.*, **71**, 3636–3658.

Vigh, J. L. and W. H. Schubert, 2009: Rapid Development of the Tropical Cyclone Warm Core. *J. Atmos. Sci.*, **66**, 3335–3350.

Viltard, N. and F. Roux, 1998: Structure and Evolution of Hurricane Claudette on 7 September 1991 from Airborne Doppler Radar Observations. Part II: Thermodynamics. *Mon. Wea. Rev.*, **126**, 281–302.

Wang, Y. and G. J. Holland, 1996: Tropical cyclone motion and evolution in vertical shear. *J. Atmos. Sci.*, **53**, 3313–3352.

Wang, Y. and C. C. Wu, 2004: Current understanding of tropical cyclone structure and intensity changes - a review. *Meteorol. Atmos. Phys.*, **87**, 257–278.

Willoughby, H. E., 1990: Gradient balance in tropical cyclones. *J. Atmos. Sci.*, **47**, 265–274.

Willoughby, H. E., 2009: Diabatically Induced Secondary Flows in Tropical Cyclones. Part II: Periodic Forcing. *Mon. Wea. Rev.*, **137**, 822–835.

Yamauchi, H., O. Suzuki, and K. Akaeda, 2002: Asymmetry in wind field of Typhoon analyzed by triple Doppler radar observations. *Int. Conf. on Mesoscale Convective Systems and Heavy Rainfall/Snowfall in East Asia*, Tokyo, Japan, 245–250.

Zhang, D.-L., Y. Liu, and M. K. Yau, 2000: A Multiscale Numerical Study of Hurricane Andrew (1992). Part III: Dynamically Induced Vertical Motion. *Mon. Wea. Rev.*, **128**, 3772–3788.